Synthesis and Analysis of Physical Properties of Iron Oxides Based Nanocomposites

PhD Thesis

By

Kashif Ali

(18-FBAS/PHDPHY/F12)

Supervised By:

Dr. Javed Iqbal

Department of Physics, QAU, Islamabad

Department of Physics
Faculty of Basic and Applied Sciences
International Islamic University, Islamabad
(2020)

Forwarding Sheet by Research Supervisor

This is to certify that the work contained in this thesis entitled: **"Synthesis and Analysis of Physical Properties of Iron Oxides Based Nanocomposites"** has been carried out by **Mr. Kashif Ali** (Reg.No.18-FBAS/PHDPHY/F12) in Laboratory of Nanoscience and Technology (LNT) under my supervision. I am satisfied with the quality of his research work and allow him to submit the thesis for further process. In my opinion, this is fully adequate in scope and quality for the thesis of PhD Physics.

……

Supervisor: Dr.Javed Iqbal

Associate Professor

Department of Physics

Quaid-i-Azam University Islamabad.

Dated: …….

Synthesis and Analysis of Physical Properties of Iron Oxides Based Nanocomposites

By

Kashif Ali

(18-FBAS/PHDPHY/F12)

A thesis submitted to

Department of Physics

For the award of the degree of

PhD Physics

Signature: _____

(Chairman, Department of Physics, IIUI)

Signature: _____

(Dean, FBAS, IIU, Islamabad)

International Islamic University, Islamabad
Faculty of Basic and Applied Sciences
Department of Physics

Final Approval

This is to certify that the work in this dissertation entitled "**Synthesis and Analysis of Physical Properties of Iron Oxides Based Nanocomposites**" has been carried out by **Mr. Kashif Ali**, Registration No**. (18-FBAS/PHDPHY/F12)** and completed in Laboratory of Nanoscience and Technology, Department of Physics, Faculty of Basic and Applied Sciences, International Islamic University, Islamabad is of sufficient standard in scope and quality for the award of degree of **PhD Physics**.

Viva Voce COMMITTEE

Dr.Wiqar Hussain Shah
Associate Professor,
Department of Physics, FBAS, IIUI. _____ **Chairman**

Dr.Zafar Iqbal
Professor/HOD, Department of Physics
Riphah International University, Islamabad. _____ **External Examiner 1**

Dr.Muhammad Atif
Associate Professor/Chairman, Department
Of physics Air University Islmabad. _____ **External Examiner 2**

Dr.Sardar Skander Hayat,
Associate Professor, Department of physics,
FBAS,IIUI. _____ **Internal Examiner**

Dr.Naeem Ahmad,
Assistant Professor, Department of physics,
FBAS,IIU _____ **Co-Supervisor**

Dr. Javed Iqbal Saggu
Department of Physics,
Quaid-i- Azam University,Islamabad. _____ **Supervisor**

This work is submitted as a dissertation in partial fulfillment of the requirement for the degree of

PhD** in **PHYSICS

At

Department of Physics

International Islamic University, Islamabad.

Declaration

I hereby declare and affirm that this thesis neither as a whole nor as part thereof has been copied out from any source. It is further declared that I have completed this thesis entirely on the basis of my personal effort, made under the sincere guidance of my supervisors. If any part of this report is proven to be copied or found to be a reproduction of some other, I shall stand by the consequences. No portion of the work presented in this report has been submitted in support of an application for other degree or qualification of this or any other university or institute of learning. If any part of this project is proved to be copied from any source or found to be reproduction of some other project, I (Mr. Kashif Ali) shall be legally responsible for punishment under the plagiarism rules of Higher Education Commission (HEC), Pakistan.

Kashif Ali
(18-FBAS/PHDPHY/F12)

DEDICATED TO

My Sister

ACKNOWLEDGEMENT

This thesis is the result of six years of research work. During this period, I have been go together with and supported by many people from different universities and R &D organizations. It is the pleasurable moment and chance for me to express my gratitude for all of them.

The first and foremost person I would like thank is my supervisor Dr. Javed Iqbal Saggu for his continuous support, outstanding scientific guidance, experimental skills, tremendous cooperation & motivation always encourage me during my Ph.D. research work. I owe a debt of gratitude to my Co-Supervisor Dr. Naeem Ahmad, from whom I have learned much about materials science, magnetism and magnetic nanomaterials. I would also like to thank Chairman Department of Physics and Dean Faculty of Basic and Applied Sciences, IIUI for their cooperation during my research work.

No thanks can be enough to acknowledge Dr. Tariq Jan for the encouragement and support I received from him. I wish to acknowledge his support, encouragement, patience and guidance throughout the research period. I am deeply indebted to him for his help, stimulating suggestions and the inspiring discussions during writing and completion of this thesis. I thank Dr. Ishaq Ahmad and Dr. Dongyun Wan for magnetic characterization of magnetic Nanocomposites by Vibrating Sample Magnetometer. My special thanks also go to my friends, Muhammad Imran Bashir, Shahid Iqbal and Ali Bahadur for supporting me whenever I need them.

No thanks can be enough to acknowledge for the endless encouragement, care and long- distance support, which I had from my uncle Muhammad Siddique. I would like to thank all my family members, for their encouragement and affection to complete my research work.

Kashif Ali

List of Publications

This thesis is based on the following publications

1. **Kashif Ali**, Javed Iqbal , Tariq Jan, Ishaq Ahmad , Dongyun Wan, Ali Bahadur, Shahid Iqbal Synthesis of $CuFe_2O_4$-ZnO nanocomposites with enhanced electromagnetic wave absorption properties, *Journal of Alloys and Compounds* 705 (2017) 559e565.
2. **Kashif Ali** , Javed Iqbal , Tariq Jan , Naeem Ahmad , Ishaq Ahmad , Dongyun Wan; Enhancement of microwaves absorption properties of $CuFe_2O_4$ magnetic nanoparticles embedded in MgO matrix , *Journal of Alloys and Compounds* 696 (2017) 711e717.
3. **Kashif Ali** ,Tariq Jan, Javed Iqbal , Ishaq Ahmad ,Dongyun Wan and S. Z. Ilyas Structural, magnetic and electromagnetic wave absorption properties of WO_3–$CuFe_2O_4$: a novel nanocomposite, *J Mater Sci: Mater Electron* DOI 10.1007/10854-017-6801-1.
4. **Kashif Ali**, Javed Iqbal, Tariq Jan,Dongyun Wan ,Naeem Ahmad, Ishaq Ahamd , Syed Zafar Ilyas , Structural, dielectric and magnetic properties of SnO_2-$CuFe_2O_4$ nanocomposites , Journal of Magnetism and Magnetic Materials 428 (2017) 417–423.
5. **Kashif Ali**, Javed Iqbal, Tariq Jan, Ishaq Ahmad, Dongyun Wan, Ijaz Ahmad, Influence of NiO concentration on Structural, Dielectric and Magnetic properties of Core/Shell $CuFe_2O_4$/ NiO nanocomposites. 10.1016/j.matchemphys.2017.03.013.

Abbreviations

EM: Electromagnetic

EMI: Electromagnetic Interference

RCS: Radar cross section

MOs: Metal oxides

RCS: Radar Cross section

MNPs: Magnetic nanoparticles

$CuFe_2O_4$: Copper Ferrite

ZnO*:* Zinc *Oxide*

MgO: Magnesium Oxide

WO_3: Tungsten Trioxide

SnO_2: Tin Dioxide

RTFM: Room Temperature Ferromagnetism

FMR: Ferromagnetic Resonance

IR: Infrared

FCC: Face Centered Cubic

JCPDS: Joint Committee on Powder Diffraction Standards

SEM: Scanning Electron Microscopy

TEM: Transmission Electron Microscopy

FTIR: Fourier Transform Infrared Spectroscopy

VNA: Vector Network Analyzer

M: Magnetization

M*s*: Saturation magnetization

M-H*:* Magnetic Hysteresis

GHz: Giga Hertz

K: Kilo

M: Mega

Oe: Oersted

dB: Decibel

Hz: Hertz

MW: Microwave

H*c*: Coercivity

Abstract

Nanosized magnetic composites have attained excessive consideration and importance over the last few decades. Nanocomposites materials are one of the main subjects of the present-day research and development. The physical properties of magnetic nanocomposites materials are different as compared to their monocomponent counterparts, and their properties can be tuned by increasing the contents of the host material. The aim of this research study focuses on the synthesis of Copper Ferrite (*$CuFe_2O_4$*) and selected metal oxides (*MOs*) nanocomposites in nanocrystalline form and studies their magnetic, dielectric and electromagnetic absorption (*EM*) properties.

The response of *$CuFe_2O_4$* magnetic nanoparticles (*MNPs*) with *MOs* (*ZnO, MgO, WO_3, SnO_2 and NiO*) nanostructures towards *EM* radiation absorption at Microwave (*MW*) frequency enhances the effective absorption bandwidth. These *MOs* nanostructures behave like dielectric loss fillers and alter the electrical conductivity, dielectric permittivity, and interfacial polarization. Moreover, the synergistic behavior between the dielectric and magnetic components also plays a vital role for strong *MW* absorption. In this research work, *MOs* nanostructures, *$CuFe_2O_4$ MNPs*, and their nanocomposites have been prepared by facile wet chemical route and characterized by different experimental techniques. The obtained results are interpreted and discussed in this thesis which consists of nine chapters.

The first chapter is a brief introduction of ferrites, *MOs* nanostructures, magnetic nanocomposites, and the approaches to minimize the *EM* reflection. The second chapter discusses the literature review and the theory of *EM* absorption. The third chapter introduces the synthesis method applied and working principles of characterization techniques used to obtain the results.

The detailed studies on the required physical properties of *MOs* nanostructures are briefly described in the fourth chapter. The fifth chapter describes the synthesis and *MW* absorption characteristics of $(ZnO)_x/(CuFe_2O_4)_{1-x}$ nanocomposites. The *XRD* analysis confirms the formation of the required composite with crystallite size ranges from 30-81nm. The *SEM* images depict the nanodiscs like morphology and Transmission Electron Microscopy (*TEM)* analysis confirms that $CuFe_2O_4$ *MNPs* are embedded in *ZnO* matrix. The saturation magnetizations (*Ms*) of superparamagnetic (*SPM*) nanoparticles in composite sample decreases with *ZnO* contents. The higher content of $ZnO \geq 40\%$ in composite sample enhances the effective absorption in a required frequency band (2-10 *GHz*).

The sixth chapter deals with the improvement in *MW* absorption characteristics of $CuFe_2O_4$ *MNPs* with *MgO* nanostructures. The structural analysis confirms the formation of nanocomposites in which both phases are present. The *MgO* contents transform the spherical morphology of $CuFe_2O_4$ into an irregular shape as depicted from *TEM* images. All samples show the same ferromagnetic behavior with decrease in M_s value with *MgO* weight fractions. The *RL* properties show an enhancement in effective absorption bandwidth at 40 wt. % of *MgO* content.

The seventh chapter also focuses on structural, vibrational, magnetic and *MW* absorption characteristics of novel WO_3- $CuFe_2O_4$ nanocomposites. The structural investigation confirms the formation of nanocomposites. The *TEM* micrographs demonstrate that the addition of WO_3 weight fraction leads to the growth of WO_3 grains with an irregular plate-like structure. This irregular structure offers high value of shape anisotropy which leads to an enhancement in coercivity (H_c) as depicted from *M-H* loops. The *MW* absorption study also demonstrates a shift in *RL* towards higher frequency at an elevated concentration of WO_3 in the composite.

The eighth chapter briefly explain the *MW* absorption properties of $(SnO_2)_x/(CuFe_2O_4)_{1-x}$ nanocomposites. The structural study reveals that the composite sample exhibit the single phase up to 30 wt.% of SnO_2 due to thermodynamically solubility of Sn^{4+} ion in $CuFe_2O_4$. The *TEM* images demonstrate that the SnO_2 wt. fractions in composite samples alter the shape and particle size from spherical to flatter plate like. The *M-H* loops of composite samples show the *SPM* behavior with systematic decrease in M_s values due to the substitution of magnetic ions (Cu^{2+} and Fe^{3+}) with non-magnetic ion Sn^{4+}. The *MW* absorption study display the maximum absorption for 10 and 20 wt. % of SnO_2.

Finally, the ninth chapter also describes the *MW* absorption properties of $NiO/CuFe_2O_4$ nanocomposites. The structural investigation demonstrates the formation of $NiO/CuFe_2O_4$ phase and *TEM* micrographs display the spherical morphology of particles for all composition. The *M-H* loops show a decreasing trend in M_s and H_c which is ascribed to the increase in mass fractions of nonmagnetic samples and particle size respectively. The *RL* measurement shows a shift in absorption peaks towards higher frequency regime with *NiO* contents. Moreover, the maximum absorption -47.07 *dB* at 8.2 *G Hz* frequency with 30 wt. % of *NiO* has also been observed.

Table of Contents

List of Figures

List of Tables

Chapter No. 1

Introduction

The development of electromagnetic (*EM*) theory in the 19th century enables the industrial strategies to use the *EM* waves in engineering and medical applications. The *EM* waves transmitted by its source with certain frequency are used for various purposes like data transfer in information sharing, broadcasting, medical diagnostics and aircraft detection [1-4]. Different sources of *EM* waves generate signals of diverse frequency, which cause interference of *EM* waves that result in misconception of data carried by the *EM* wave. Undesired *EM* signals can be evaded by segregating the source (or the receiver) with proper shielding. Electromagnetic Interference (*EMI*) shielding is thus applied by a suitable material coating that lessens the intensity of *EM* waves and provides a more protected/secure system [5].

During the last few decades, *EM* absorbing materials have gained a great interest in military and defense for the protection of strategic assets by reducing the Radar Cross Section (RCS) of distant objects. When reflection loss (*RL*) of *EM* absorbing coating is equal to *-10dB*, the 90% power of wave is absorbed. The resultant frequency range in which *RL* attains the value smaller than *-10dB*, is demarcated as the operative bandwidth [6]. The existing *EM* absorbing materials possess high density, deprived environmental permanence, and feeble absorption in narrow operative bandwidth. These high density materials result in enhancement of weight carried by aircraft and produce performance problems for movable system [4]. Therefore, manufacturing of *EM* absorbing materials with strong and effective absorption having light weight, low cost and environmental stability extended a strategic significance particularly, in defense applications.

Recent material scientists and engineers are trying to synthesize novel *EM* absorbing materials that deal through numerous kinds of *EM* radiation (*MHz-GHZ*) for several applications.

The ferrites are renowned to be ideal *EM* absorber materials at microwave (*MW*) frequency, because they encompass magnetic and dielectric characteristics simultaneously [7]. But the heavy weight and inferior dielectric loss restrict the application of ferrite for microwave (*MW*) absorption [8-10]. Therefore, to enhance the dielectric loss in ferrites, the different metal oxides (*MOs*) nanostructures demonstrating metallic, semiconducting and insulating behavior are always added into the ferrites [11-12].

In this research work, the magnetic nanocomposites of copper ferrite ($CuFe_2O_4$) with different weight fractions (10-50 wt.%) of *MOs* (M= *ZnO, MgO,* WO_3, SnO_2, *and NiO*) nanostructures were synthesized by *ex-situ* method. Their structural, morphological and vibrational study was carried out by *XRD, SEM, TEM and FTIR* techniques. The magnetic and *MW* absorption properties of $(MO)_x/(CuFe_2O_4)_{(1-x)}$ nanocomposites has also been performed by *VSM* and Vector Network Analyzer (*VNA*) respectively.

1.1 Ferrites

Ferrites are composed of iron oxides with one or more metal ions (AFe_2O_4) at tetrahedral or octahedral sites. Ferrites are ferrimagnetic materials that brought a technological revolution during the last few decades. This important magnetic material contains fascinating dielectric and magnetic properties including high resistivity, low dielectric constant, high value of coercivity, high corrosion resistance and high value of anisotropic energy. These fascinating properties enable this material; to be extensively used in *MW*, electrical and magnetic devices [13]. Recently ferrites properties can be tuned for many uses by tailoring their magnetic and dielectric properties through the addition of suitable dopant atoms and forming nanocomposites with polymer and *MOs* nanostructures.

The recent uses of ferrites and their composites at nanoscale are spintronic devices, drug delivery system [14, 18], data storage devices and transformers core [19-22].

Among the various ferrites, $CuFe_2O_4$ has attained a conspicuous attention due to Jahn Teller nature of Cu^{2+} ion [23]. The structure of $CuFe_2O_4$ is highly distorted due to cooperative Jahn-Teller effect [24]. As Cu^{2+} is a Jahn Teller ion, it offers extraordinary characteristics and also endures phase transition from cubic to tetragonal depending upon ionic distribution in octahedral symmetry. This transition from cubic to tetragonal influence the dielectric and magnetic properties of $CuFe_2O_4$ which is beneficial for tuning the *EM* parameters.

1.2 Crystal Structure of Ferrites

The spinel structure of ferrite can be considered as a complex structure of positively charged metal ions and negatively charged oxygen ions [25]. The chemical formula of spinel ferrite is AB_2O_4, where A^{2+} is a divalent and B^{3+} is a trivalent metal ion.

The crystal structure can be understood by subdividing the unit cell into *8* unit cells, as shown in *Fig. 1.1*. There are 8 formula units in whole unit cell. The unit cell of spinel ferrites (AB_2O_4) contains *32* oxygen ions, 8 divalent metal ions and 16 trivalent iron ions and can be written as $M_8Fe_{16}O_{32}$. The interstitial sites are denoted as tetrahedral or *A* sites and octahedral or *B* sites. Moreover, the distinctive characteristic of ferrites is governed by the cation sharing between the tetrahedral and octahedral sites in a lattice.

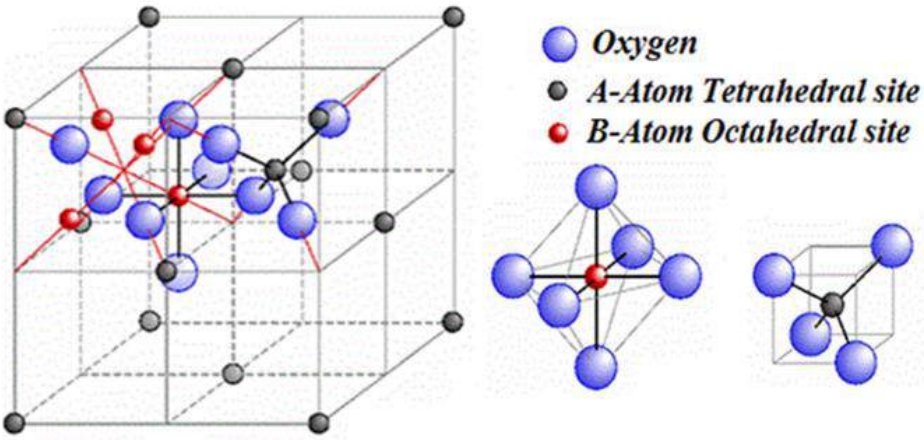

Figure 1.1: AB_2O_4 spinel structure of ferrite [26]

1.2.1 Tetrahedral Sites (A Sites)

The tetrahedral site is bounded by four oxygen O^{2-} ions (anion) located at the corners of a tetrahedron as depicted in *Fig. 1.2 (a)*. There are 16 tetrahedrons in the unit cell of spinel lattice. Therefore, there are total 64 tetrahedral sites out of which only 8 *A* sites are filled by divalent metal ions to preserve charge neutrality of the system. In a face centered (*FCC*) cubic structure, there are 8 tetrahedral (*A*) sites per unit cell.

1.2.2 Octahedral Sites (B Sites)

The octahedral site is bounded by six oxygen O^{2-} ions located at the corners of an octahedron. In an octahedral (*B*) site the interstitial atom occupies at the center of an octahedral. In this octahedron, the metal ions are surrounded by six nearest neighbors as shown in *Fig. 1.2 (b)*. In a spinel structure, to maintain the charge equilibrium, out of *32* octahedral (*B*) only *16* sites are occupied. In a FCC structure, there are *4* octahedral (*B*) sites per unit cell.

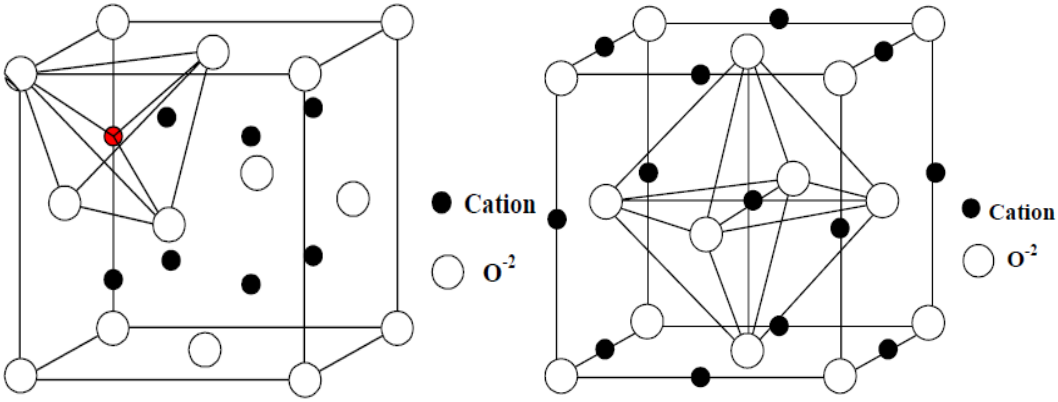

1.2: (a) Tetrahedral A sites in spinel FCC lattice (b) Octahedral B sites in spinel FCC lattice [27]

1.3 Metal Oxides (MOs) Nanostructures

Among the different types of *MOs* nanostructures, *ZnO, MgO, WO_3, SnO_2* and *NiO* are well-known for their several kinds of applications for humankind. These *MOs* plays a very critical role in science and technology. Pure metal easily forms a chemical bond with oxygen and transforms into oxide. In crystalline form, these oxide compounds form large number of geometries depending upon the arrangement of atoms in a unit cell. The electronic structure determines their electrical and magnetic properties. During last few decades, different *MOs* nanostructures are extensively used in manufacturing of supercapacitor, fuel cells, gas sensors and as dielectric loss filler for *EMI* shielding [28-31]. Moreover, at nano dimension these *MOs* nanostructures show exclusive physical and chemical properties due to quantum confinement and proliferation in the surface atoms [27].

1.3.1 Zinc Oxide (ZnO)

ZnO is most familiar and extensively studied semiconductor material in the field of material science and engineering because of its exclusive characteristics and application in different areas of science and technology [29].

Wurtzite-structured *ZnO* possesses excessive significance for its useful applications in *EM* wave absorption, optoelectronics, piezoelectricity, *LASER*, acous-optical devices and sensors etc. [30].

The *ZnO* nanostructures show great potential for *MW* absorption at *GHz* frequency range due to their high dielectric loss, semiconducting behavior and unique physicochemical properties [31]. The chapter 5, focuses on the deep analysis of structural, and *MW* absorption properties of $(ZnO)_x/(CuFe_2O_4)_{1-x}$ *(x=10-50 wt.%)* nanocomposites with the addition of nano disc like morphology of *ZnO*. This study revealed that *ZnO* is a promising candidate to enhance the *MW* absorption in wideband.

1.3.2 Magnesium Oxide (MgO)

Among the different *MOs* nonmaterial, cubic and rock salt *MgO* structures are extremely important due to its unique photonic, optical, electronic, magnetic, mechanical and chemical properties. These fascinating characteristics enable this material to be used as fire retardant, electrical cable insulation, toxic waste remediation, antibacterial paints, and in superconducting devices [34-37]. Moreover, the high dielectric constant of *MgO* makes it beneficial to use in *MW* absorption coating. The chapter 6 of this thesis discusses the *MW* absorption properties of $CuFe_2O_4$ nanocomposites in which *MgO* weight fraction varies from 10-50 wt. %.

1.3.3 Tungsten Trioxide (WO_3)

WO_3 is an *n*-type semiconductor with bandgap of 2.6 to 2.9 eV having tremendous electro-chromic characteristics. Its electron Hall mobility at room temperature has value of ~12 $cm^2V^{-1}s^{-1}$ [38]. The WO_3 has possible applications in displays windows, solar cells, smart windows, and various gas sensors [39, 40]. WO_3 is most important and extensively studied semiconductor material which reveals outstanding properties at nanolevel. Therefore, understanding of WO_3 at nanoscale can further explore the physical and chemical properties because quantum confinement effects at the nanoscale pointedly affect charge transport, electronic band structure, and electrochemical characteristics. In chapter 7**,** we first time observe the room temperature

ferromagnetism (*RTFM*) in WO_3 at nanoscale. Moreover, the influence of WO_3 weight fractions in $CuFe_2O_4$ composites shifts the *RL* towards higher frequency.

1.3.4 Tin Dioxide (SnO_2)

SnO_2 is an n-type semiconductor having band gap of 3.6 eV. The main reason for the interest in SnO_2 is its high dielectric loss and large value of conductivity. Moreover, SnO_2 shows high transparency in visible region, which makes it enable to use as a transparent conductive electrode in different devices such as solar cells and lithium ions batteries [41-43]. The defects free SnO_2 in bulk form shows insulating behavior while at nanoscale the oxygen vacancies and other defects make it conducting and magnetic [44]. Moreover, SnO_2 nanostructure contains high value of dielectric constant, which can be further tailored by increasing the weight fractions of constituents in composite [45-48]. The chapter 8 of this thesis, briefly explains magnetic and *MW* absorption properties of $(SnO_2)_x/(CuFe_2O_4)_{1-x}$ ($x=10\text{-}50$ *wt.%)* nanocomposites at room temperature.

1.3.5 Nickle oxide (NiO)

NiO is a p-type semiconductor material having a wide band gap of 3.6 to 4.0 eV with room temperature conductivity of less than 10^{-13} S cm^{-1}. This low value of conductivity is attributed to the jumping of electrons linked with Ni^{2+} vacancies at nanoscale [49,50].

In addition, *NiO*-based nanostructures have been extensively applied as electrode materials in lithium ion batteries and fuel cells [51, 52]. *NiO* shows an anodic electrochromic effect and finds its applications in smart windows, dye-sensitized photocathodes [53-55]. Controlling the structural, magnetic and dielectric properties of single crystalline *NiO* nanostructures enables it to use in the required application. In chapter 9**,** an effort has been made to study the morphological,

magnetic and *MW* absorption characteristics of $(NiO)_x/(CuFe_2O_4)_{1-x}$ ($x=10-50wt.\%$) composites synthesized by chemical co- precipitation method.

1.4 Magnetic Nanocomposites

A "nanocomposite" is defined as a composite in which the individual component(s) is/are dispersed in continuous matrix forming a compositional heterogeneity of the final solid structure. The simplest alteration of a composite property, P_c, is monotonic increase or decrease with the increase of volume fraction, "V_i" of the supplementary components; which is demonstrated by the following equation:

$$P_c = \sum_{i=1}^{N} (P_i)^{n} V_i \quad (1.1)$$

Where P_i is added material property and n is an experimental parameter ($-1 \leq n \leq 1$). Nanocomposites differ from their bulk counterpart due to strong interactions between grains and grain boundaries. Nanocomposites exhibit distinct behavior due to these effects ***(a)*** the large surface to volume ratio of atoms ***(b)*** the large grain boundary effect, and ***(c)*** the surface effect. The nanocomposites also contain numerous applications in various areas, such as in *MW* absorber and *EMI* shielding materials, biocompatible *MNPs*, conducting polymer nanocomposites and manufacturing of electronic and photonic devices [56, 57].

Among different types of nanocomposites, the magnetic nanocomposites have achieved abundant application in giant magneto resistance (*GMR*), magnetic recording, magnetic refrigeration and *EM* shielding [58, 59].

One recently studied nanocomposite material is the ferrite composite with *MOs* and polymers [60,61]. The importance of magnetic nanocomposite is that after a little modification, the electric and magnetic properties can tailored for required application [62]. In this thesis, the $CuFe_2O_4$ based magnetic nanocomposites were prepared by wet chemical co-precipitation route for *EM* shielding

in the *GHz* frequency range. The different weight fractions (*10-50 %)* of *MOs* nanostructures were added in the $CuFe_2O_4$ composite to enhance the dielectric loss and hence reduce the *RL* of *EM* waves.

These nanocomposites demonstrate an excellent *EM* absorption characteristics owing to the space charge or interfacial polarization, effective impedance matching to free space and synergic effect of dielectric and magnetic properties [63-65].

1.5 Reflection/Absorption of EMW and their relationship with permittivity and permeability

Figure 1.3 shows the mechanism for interactions of *EM* waves with matter. Some portion of incident power P_I is reflected as P_R and the remaining non-reflected power P_I - P_R is transmitted into the material. As the *EM* wave passes through the material, it can be absorbed and dissipated in the form of heat.

Through this basic reflection and transmission mechanism, it is promising to define the total shielding efficiency (SE_T) as:

$$SE_T = 10\log\frac{P_I}{P_T} = 20\log\frac{E_I}{E_T} = 20\log\frac{H_I}{H_T} \quad (1.2)$$

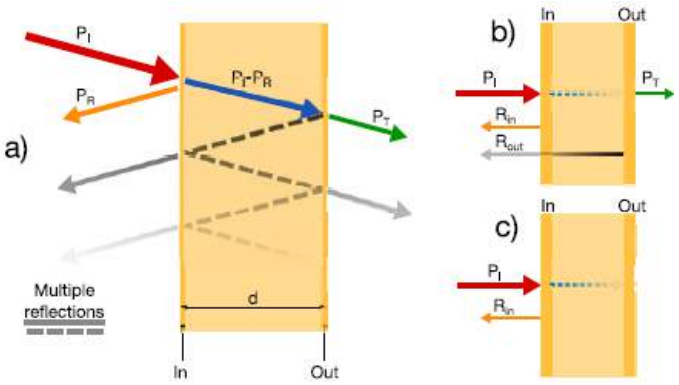

Figure 1.3: Mechanisms of attenuation of the incident and reflected EM power, when it strikes a finite slab of material [66-68].

Considering the total power after striking the material will either reflect or absorb the total *SE* (*SE*$_T$) can be rewritten as:

$$SE_T = 10 \log \frac{P_I}{P_T} = SE_R + SE_A \quad (1.3)$$

$$SE_R = 10 \log \frac{P_I}{P_{I-}P_R} \quad (1.4)$$

$$SE_A = 10 \log \frac{P_{I-}P_R}{P_T} \quad (1.5)$$

Where *SE*$_A$ and *SE*$_R$ refers to shielding due to absorption and reflection respectively. The *SE*$_R$ can also be expressed in terms of the impedance ratio between free space (*Z*$_o$) and the material's surface (*Z*$_{in}$); and *SE*$_A$ as a function of shield thickness (d) and its skin depth (δ) is given as :

$$SE_R + SE_A = 20 \log \frac{Z_0}{Z_{in}} + 20\, log e^{\frac{d}{\delta}} = SE_T \quad (1.6)$$

Where Z_o = 377 Ω is free space impedance and Z_{in} is impedance of the material and the reflection occurs due to the mismatch of impedance at the surface of material. It can also be observed that the extent of absorption depends upon the depth of penetration (***δ***) of the wave and the capability of the sample to dissipate the field within the thickness (**d**). The skin depth increases with decrease in frequency (**f**), permeability (***μ***) and conductivity (***σ***) as shown in following equation:

$$\delta = (\pi f \sigma \mu)^{-1/2} \quad (1.7)$$

For conductive monolithic shields *SE*$_R$ and *SE*$_A$ can be rewritten in terms of σ and δ as [65]

$$SE_R = 20 \log \frac{Z_0}{4Z_{in}} = 39.5 + 10 \log \frac{\sigma}{2\pi f \mu} \quad (1.8)$$

$$SE_A = 20 \log_e \frac{d}{\sigma} = 8.7 \frac{d}{\delta} = 8.7 d \sqrt{\pi f \mu \sigma} \quad (1.9)$$

Eqs. (1.8 and 1.9) show that the reflection *SE*$_R$ depends only on σ/μ while the absorption is a function of ***μ.σ*** and the material thickness. Hence it explains that why non-magnetic metals are

susceptible to shield mainly by reflection, while in magnetically permeable shields, even if they are conductive, SE_A is generally related to attenuation as compared to reflection.

But in composite materials, the situation is quite different because composites contain highly heterogeneous microstructure that is accountable for enormous variations in the local fields [66]. The $\boldsymbol{\varepsilon}$ and $\boldsymbol{\mu}$ define how the electric and magnetic fields interact with composite material and the real part of $\boldsymbol{\varepsilon}$ and $\boldsymbol{\mu}$ gives information about the energy stored in material while their imaginary part gives the amount of energy dissipated as heat [67].

Ferromagnetic metals (*Fe, Ni, and Co*) and alloys have high saturation magnetization (M_s) and large permeability value. Though, their exceedingly conductive nature and eddy current losses aggravate permeability to go down at lower frequencies than anticipated (*50 kHz-10 MHz*) [68]. Ferrites on the contrary, are semiconductor in nature and their electrical resistance is high than that of ferromagnetic metals and alloys. Furthermore, when the grain size of materials become small to some critical size, the eddy current losses turn into negligible but the anisotropic energy and surface effects play a dominant role ascribed to large surface area [69, 75]. A modification in the anisotropy energy leads to the adjustment of the spin relaxation frequency with the change in particle size. In this perspective, the dispersion of permeability in composites sample embedded with magnetic nanoparticles is govern by relaxation mechanism rather than by the intrinsic resonance observed in bulk magnets. According to the relaxation theory of magnetic moments, permeability can thus be maintained at a constant value until relaxation [76-85].

1.6 Statement of Problem

The development of ferrite based nanocomposites for *EMI* shielding and *EM* absorption at *GHz* frequency has become one of the most important issues in the fields of material science and engineering. Therefore, scientists are trying to produce novel types of nanocomposites for *EM* absorption in wide band. It is noticed from reported literature, that there is no lightweight material that fulfills the objective to minimize the *RCS*. To enhance the effective absorption characteristics, it is essential to synthesize a special light weight microstructure to obtain the desired results. In the *MW* absorber, ferrites at nanoscale are favorable, because their large M_s value leads to higher *MW* permeability and the nanosized dimensions produce high surface anisotropy. Ferrites contain multiple dielectric and magnetic resonance and demonstrate as a promising candidate for excellent *MW* absorption performance. But ferrite based absorber contains high density and low dielectric loss, which prevent them to produce light weight *EM* absorbing coating in wide band. In order to reduce the weight and enhance the *EM* absorption performance of *MNPs***,** many studies have focused on light weight nanocomposites. In ferrite based nanocomposite, the dielectric loss filler like *MOs* nanostructures with different weight fractions has been added that tailor their dielectric and magnetic properties to the desired extent.

However, the *EM* absorption properties of materials depend on many factors like: particle size, morphological shape, coating thickness, and loading percentage. Therefore, to control these parameters for required physical characteristic at low-cost mass production, it is extremely challenging to build up new methodologies for the synthesis of nanocomposites with expected properties.

1.7 Aims and Objectives

- Synthesis of *CF* and various *MOs* (*MgO, NiO, SnO_2, WO_3 and ZnO*) nanostructures with controlled size and morphology through the easily available, reproducible wet chemical co-precipitation method by optimizing reaction parameters.
- Synthesis of $(MOs)_x/(CuFe_2O_4)_{(1-x)}$ (where *x=10-50 wt.%)* nanocomposites through *ex-situ* method.
- Development of low-density *MW* absorbing coating by incorporation of light weight *MOs* nanostructures in $CuFe_2O_4$/*MNPs*.
- Enhancement in effective absorption bandwidth in required frequency range by tailoring the electric and magnetic properties, which is controlled by loading percentage of *MOs* nanostructures.
- Tuning in absorption peak to high frequency regime by incorporation of *MOs* nanostructure for selective *EM* shielding in required frequency.
- Selection of *MOs* nanostructure with $CuFe_2O_4$ having strong and effective absorption in the required frequency bandwidth that minimizes the *RCS*.

Chapter No.2

Literature Review and Theory of Electromagnetic Absorption

EM absorbing materials have appealed abundant consideration for the protection of civil and military assets. A large number of *EM* absorbing materials have been used, such as carbon nanotubes (*CNTs*), graphene, polymers composites, spinel and hexagonal ferrites etc. [86-119]. The spinel ferrites are mostly used as conventional *MW* absorbers due to their high M_s value, moderate H_c and environmental stability. But the only magnetic loss mechanism in ferrite leads to weak *MW* absorption in small frequency bandwidth. However, high density and low dielectric loss of ferrite prevent their use as *MW* absorbers [87,88].Therefore ferrite nanocomposite with dielectric loss material such as *CNTs*, graphene, nonconductiong polymers and *MOs* can be added with different weight fractions, that reveal a higher absorption at low field strengths and widen the absorption band width in *MW* region [89]. Moreover, the performance of *EM* absorbing properties of spinel and hexagonal ferrites can be enhanced by synthesizing their nanocomposites using different synthesis techniques. During last few years scientists focused on ferrite nanocomposite for *EM* shielding application e.g. Ying Lin et. al, synthesize the $CoFe_2O_4/Y_3Fe_5O_{12}$ nanocomposites with polyaniline by polymerization method and achieve maximum *RL* of *-23.4 dB* at *7.7 GHz* [90], Muhammad Faisal et. al, synthesized conducting polyaniline-stannous oxide nanocomposite. There nanocomposite revealed excellent absorption in X and K_u band [91]. Guizhen Wang et. al, prepared flower-like *ZnO* coated by *Ni* nanoparticles and maximum *RL* -48.0 *dB* was obtained at 10.4 *GHz* which is remarkably improved than pristine *ZnO* [92]. W. Widanarto et. al, synthesized *ZnO* doped strontium nano ferrites of composition $(80 - x)\ Fe_2O_3: xZnO:20\ SrCO_3$, where x = (0 - 20 mol%) and sintered through the solid state reaction scheme.

Strontium ferrite containing 20 mol % of *ZnO* exhibits greater microwave absorption with *RL* between - *45dB* to - *55dB* in the frequency range of 7–13 *G Hz* [93].

C. Della Pina et. al, prepared Fe_3O_4 nanoparticles (*NPs*) by chemical method which covers the whole K-band (*18-26 GHz*). The parameters at *K*-band were retrieved by using different mathematical equations, which allowed estimating the electric and magnetic parameters with good accuracy over whole *K*-band [94]. A. Poorbafrani et. al, synthesized strontium ferrite *NPs* with different concentrations of *ZnO* for *MW* absorption. The *RL* measured in *X* and K_u-bands and increase in contents of *ZnO* up to 15%, shows increase in *RL* in the K_u frequency band by *5 dB* [95] . K.C. Tripathi et. al, has successfully prepared sample of particulate composite with 30 % (by wt.) *Ni-Zn* nano-ferrite loaded in polyurethane (*PU*) matrix. Sample has described increasing *RL* from *-7.95 dB* to *-12.93 dB* [96]. Haibo Yang et. al, successfully prepared polyaniline/$(1-x)BaFe_{12}O_{19}/CaFe_2O_4/xCoFe_2O_4$ nanocomposite by polymerization method. The results showed that, this magnetic nanocomposites revealed enhanced *MW* absorption performance (*RL* is *-39.5 dB* was achieved at frequency of 7.9 *GHz*) in comparison to single polyaniline/$(1-x)BaFe_{12}O_{19}/xCoFe_2O_4$ and $PANI/CoFe_2O_4$ nanocomposites [97]. Bingzhen Li et. al, synthesized $Fe_3O_4/PPy/PANI$ nanocomposites by modified co-precipitation method. This nanocomposite demonstrates excellent *MW* absorbing property with *10.7 G Hz* bandwidth and also shows maximum *RL* (*-40.2 dB*) at *10.1 GHz* [98]. Jingbo Guo et. al, was firstly prepared carbonyl-iron/$Fe_{91}Si_9$ composites by a simple blending technique. This material revealed *RL -20dB* in the frequency band of 4 G Hz [99] . Xianming Qin et. al, was prepared $Ba(MnZn)_xCo_{2(1-x)}Fe_{16}O_{27}$ *(x=0.1- 0.5)* by sol-gel process and *MW* absorbing properties was studied at a coating thickness of 2.8 mm .The minimum *RL* peak was observed at - 40.7 *dB* with band width of *6.6 GHz* at a frequency of 7.3 *GHz* [100].

In this research work, to widen the band width below -10 dB (90% absorption), the $CuFe_2O_4$ based nanocomposite was prepared by *ex-situ* method with different weight fractions (10-50 wt. %) of *MOs* nanostructures. The *RL* behavior show strong absorption in tunable frequency at different composition of $CuFe_2O_4$/*MOs* nanocomposite. Moreover, an enhancement in *MW* absorption over whole frequency band (*2-10 GHz*) has also been observed. To understand the mechanism involved for absorption of *MW* radiation, it is necessary to first study the Maxwell's Equations. These are the fundamental equations that describe any *EM* system.

2.1 Maxwell's Equations

EM wave comprises of an oscillating electric *E* and magnetic field *B* that are perpendicular to each other and also to the direction of propagation. Therefore, to understand the absorption mechanism it is necessary to study the understanding of their interaction with a material.

Suppose a pulse of microwaves with definite frequency is emitted by *radar* antenna, which propagates through free space. Maxwell's equations for this *EM* waves can be written as:

$$\nabla . E = 0 \tag{2.1}$$

$$\nabla . B = 0 \tag{2.2}$$

$$\nabla \times E = -\frac{\partial B}{\partial t} \tag{2.3}$$

$$\nabla \times B = \varepsilon_0 \mu_0 \frac{\partial E}{\partial t} \tag{2.4}$$

When this *EM* wave strike the aircraft's surface, little portion of wave is reflected back and remaining portion is absorbed. Now, it is necessary to understand, what happens at an interface of aircraft in terms of Maxwell's equations in a medium [118-120].

Which are given as:

$$\nabla . D = \rho \tag{2.5}$$

$$\nabla . B = 0 \tag{2.6}$$

$$\nabla \times E = -\frac{\partial B}{\partial t} \tag{2.7}$$

$$\nabla \times H = J_f + \frac{\partial D}{\partial t} \tag{2.8}$$

Where D is an electric displacement and J_f is a free current density. The relationships between four vector fields are given by constitutive relations:

$$D = \varepsilon_r \, \varepsilon_0 E \tag{2.9}$$

$$H = \frac{1}{\mu_r \, \mu_0} B \tag{2.10}$$

$$J_{f=} \, \sigma E \tag{2.11}$$

Where ε , $\mu \; and \; \sigma$ are permittivity, permeability and conductivity of the material respectively.

2.2 Interaction of EM Wave with Material

EM waves radiated from source travel in all direction in atmospheric air and its power is attenuated as $1/r^2$, r being the distance from source. Energy possessed by the *EM* wave is transported to the ingredients of materials. The *EM* radiation interacts with material through different mechanism involved and leads to absorption of radiation [121,122]. To conserve the energy principle, the absorbed energy is dissipated as heat. When an *EM* power strike an aircraft surface, sum of reflected power P_R, transmitted power P_T and absorbed power P_A with respect to the incident power P_o should be unity.

$$\frac{\mathrm{P_R}}{\mathrm{P_0}} + \frac{\mathrm{P_T}}{\mathrm{P_0}} + \frac{\mathrm{P_A}}{\mathrm{P_0}} = 1 \tag{2.12}$$

An efficient *EM* absorber coating, absorb the maximum portion of incident energy depending upon the dielectric and magnetic characteristics. Therefore, the dielectric and magnetic characteristics of the materials can be improved by incorporation of different dopants ions or increase the contents of suitable dielectric and magnetic filler.

2.3 Electromagnetic Energy Absorption Mechanisms

As *EM* wave contains an *E* and *B* field component. The energy stored in the electric and magnetic fields of an absorbed *EM* wave can be derived by using *Eq. 2.1* to *Eq. 2.11*.

The energy densities are given as:

$$u_e = \frac{1}{2}\varepsilon_A \varepsilon_0 |E|^2 \tag{2.13}$$

$$u_m = \frac{1}{2\mu_A{}^2 \mu_0} |B|^2 \tag{2.14}$$

Where ε_A , μ_A are relative permittivity and permeability of *EM* absorbing material respectively. Both quantities are complex and depend upon frequency of an *EM* wave.

$$\varepsilon_A(f) = \varepsilon_A{}' + i\,\varepsilon_A{}'' \tag{2.15}$$

$$\mu_A(f) = \mu_A{}' + i\mu_A{}'' \tag{2.16}$$

Where the real parts $\varepsilon_A{}'$ and $\mu_A{}'$ gives the information about energy stored in a material while the imaginary parts $\varepsilon_A{}''$ and $\mu_A{}''$ are related to the dissipative nature of material. As the conductivity σ of material also plays a major role in loss mechanism, it is beneficial to relate this result in terms of $\varepsilon_A{}''$.

$$\varepsilon_A{}'' = \frac{\sigma}{\omega\varepsilon_0} \tag{2.17}$$

Where ω is radian frequency and ε_o is permittivity of free space. In polar form it can be written as,

$$\varepsilon_A(f) = |\varepsilon_A| e^{i\delta} \tag{2.18}$$

$$\mu(f) = |\mu_A| e^{i\delta_m} \tag{2.19}$$

Where δ and δ_m represent the electric and magnetic loss tangents given as

$$\tan\delta = \varepsilon''_A/\varepsilon'_A \tag{2.20}$$

$$\tan\delta = \mu''_A/\mu'_A \tag{2.21}$$

The loss tangent is defined as the energy lost per cycle to energy stored per cycle of *EM* wave. Now we will discuss why the energy is dissipated in an absorber. Energy absorption occur in a material due to polarization of permanent and induce dipoles (dielectric loss), motion of magnetic domains (magnetic loss), conduction of free charge carriers (conductance loss) and/or atomic vibrations [123,124]. Hence the performance of an *EM* absorbing material can be enhanced by tailoring its electrical and magnetic characteristics.

2.3.1 Magnetic Loss

In magnetic material, different loss mechanisms lead at different frequencies. The energy is dissipated as heat due to re-alignment of permanent dipoles and is known as magnetic hysteresis loss [125]. The area under the hysteresis loop gives the value of energy loss. The two important parameters obtained from this loss mechanism as displayed in *Fig. 2.1* are:

(a) Saturation magnetization (M_s) and

(b) Coercivity (H_c)

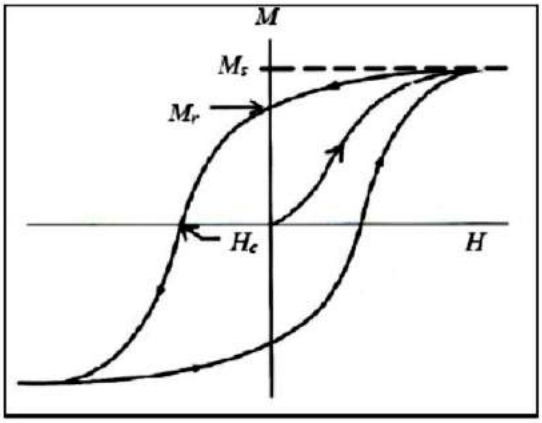

Figure 2.1: Hysteresis loop of normal ferrite [126]

Eddy current loss also contributes for energy dissipation in the form of heat in magnetic materials. In highly conductive materials like metals, this current behaves like a source of *EM* waves and re-emits the incident wave. Hence, the generation of eddy current in metals makes them a poor

absorber for *EM* waves. Generally, in a *MW* region the following loss mechanisms occur due to resonance phenomena [127].

(a) Magnetic domain wall resonance and

(b) Ferromagnetic resonance

The equation of motion for domain wall movement in an oscillating magnetic field *B (t)* can be written as [128].

$$m\ddot{x} + \beta x + kx = 2M_s\, B(t) \tag{2.22}$$

Where *x* is the domain wall displacement, *m* is inertia, β and *k* is damping and stiffness coefficient respectively. Equation *2.22* describes a damped harmonic oscillation and for small damping, a resonance effect will happen at a frequency $\omega = \sqrt{\frac{k}{m}}$.

The second resonance phenomena "Ferromagnetic Resonance" (*FMR*) is very complicated. In ferromagnetic materials, the electron's spin produces a magnetic dipole moment. As, an angular momentum is linked with this magnetic moment in static magnetic field, which exert a torque on electron and precess it along the field direction with the Larmor's angular frequency given as.

$$f_L = \frac{\gamma \mu_0}{2\pi} H = 35.2 \times 10^6 H \quad (GHz) \tag{2.23}$$

Where γ is the gyroscopic ratio $\gamma = \frac{g\mu_b}{h}$ =1.76× $10^{11}\, T^{-1} s^{-1}$, and H is the magnetic field (A/m). When a *MW* field having resonance frequency $f_{L,}$ applied in a transverse direction to an external field *H,* the torque acting on magnetic moment will enhance the angle of precession and consequently absorb the *MW* energy. When a *MW* field is removed the processional energy will be dissipated by moving the magnetization vector towards the direction of applied field as shown in *Fig. 2.2.*

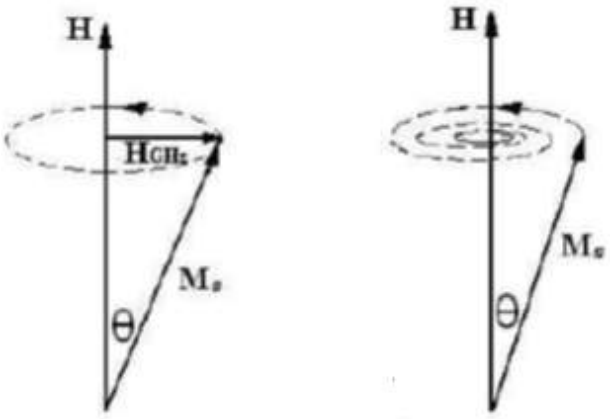

(a) (b)

Figure 2.2: (a) Absorption of *MW* energy by processional motion of magnetization vector in an external field H and (b) Dissipation of *MW* energy by moving M_s towards applied field [129].

2.3.2 Dielectric Loss

In dielectric materials induce or permanent dipoles are produced, which are susceptible to polarization by an electric field [130]. In a *MW* region, the loss is induced mainly due to dielectric relaxation of electric dipoles. The torque *T* acting on electric dipoles try to align them in the field direction, consequently producing orientation polarization as shown *in Fig. 2.3.* At low frequencies, the dipoles align with electric field, but at higher frequencies (*MW* region), the dipole alignment lags the electric field due to delay in response time. This lags in alignment of dipoles produce friction and hence energy dissipation occurs in the form of heat.

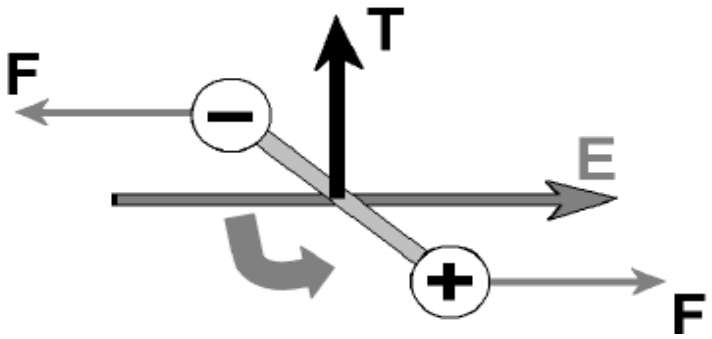

Figure 2.3: Electric dipole rotation in an electric field [125]

This rotation of dipoles lead to the tuning of both permittivities values $\varepsilon_A^{/}$, $\varepsilon_A^{//}$, at the relaxation frequency f_c, which is associated to relaxation time τ and is given as:

$$\tau = \frac{1}{2\pi fc} \tag{2.24}$$

When the frequency of dipole is below f_c, the dipoles react to the external electric field frequency and the loss $\varepsilon_A^{//}$ increases accordingly. When the external frequency increases, $\varepsilon_A^{//}$ continue to increase, but the storage ability $\varepsilon_A^{/}$, begins to go down owing to the lag of alignment among the dipole and an electric field. At frequency, higher than f_c, the dipoles do not respond to the electric field, so both parts of a permittivities $\varepsilon_A^{/}$ and $\varepsilon_A^{//}$ decrease. This dependence of permittivity with frequency for an ideal dipole is known as Debye relaxation model as displayed in *Fig. 2.4*.

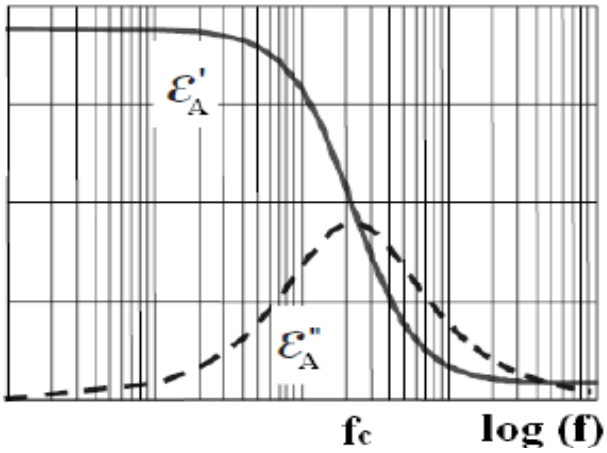

Figure 2.4: Debye relaxation spectra [126]

2.4 Dielectric Polarization versus Frequency

The different types of polarization contribute in a dielectric material when placed in an electric field as shown in *Fig.2.5*. The electronic and ionic contribution is called intrinsic while orientation and interfacial are called as extrinsic as illustrate in following equation:

$$\varepsilon = \underbrace{\varepsilon_{elec} + \varepsilon_{ion}} + \underbrace{\varepsilon_{or} + \varepsilon_{sc}} \tag{2.25}$$

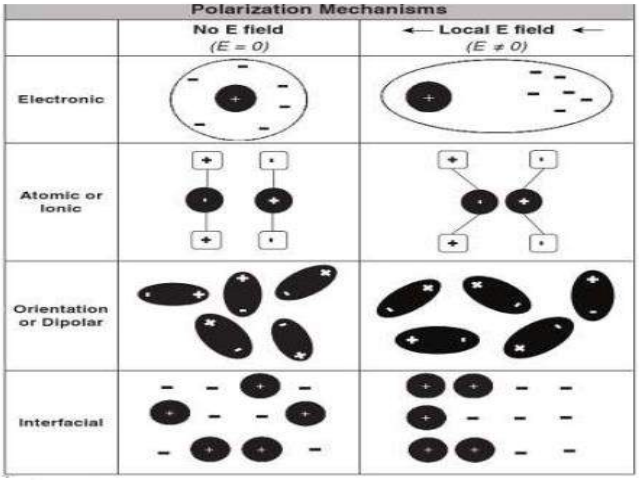

Figure 2.5: Polarization mechanisms in dielectric material [120].

The contribution of polarization depends upon frequency of external electric field and respond time of dipoles on different time scales. The dispersion of the dielectric constant (real and imaginary parts) is shown in *Fig. 2.6*, and represents the unusual dielectric contributions separately.

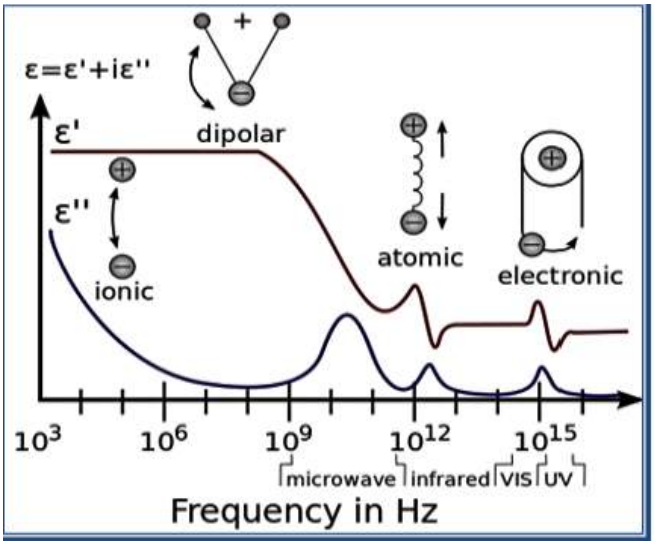

Figure 2.6: Real and imaginary part of dielectric constant as a function of frequency [132,133].

Chapter No.3

Synthesis and Experimental Techniques

Nanoscience and nanotechnology deal in synthesizing, modifying and characterizing materials that have at least one dimension in the size range of 1-100 nm. Nanotechnology encompasses all areas of science i.e. Physics, Chemistry, Electronics, Chemical Engineering, Material Science and Engineering, Medical Science and Biotechnology.

Nanosize materials contain high degree of disorder and large surface to volume ratio of atoms [134-136]. The parameter which differentiates the characteristics of nanostructure material from the bulk material is the surface effect that makes them attractive in different applications for the benefit of humankind [137].

A nanocrystalline material can be a ceramic, metal, semiconductor and their composites with different morphology that depends on crystallographic energy of lattice planes and electro-negativity of atoms. The ceramic and composite materials show distinct electrical properties and metal nanostructures become electrically more resistive at nanoscale. Furthermore, the magnetic materials, show larger value of coercivity at a specific critical particle diameter (D_c) and superparamagnetic behavior below this size [138].

The method employed for the synthesis of selected *MOs*, $CuFe_2O_4$, and their nanocomposites with controlled size and morphology are briefly discussed in this chapter.

3.1 Synthesis Methods for Nanostructures

Mainly there are two most important methodologies for the synthesis of nanomaterial i.e. top-down and bottom-up as shown in *Fig. 3.1*.

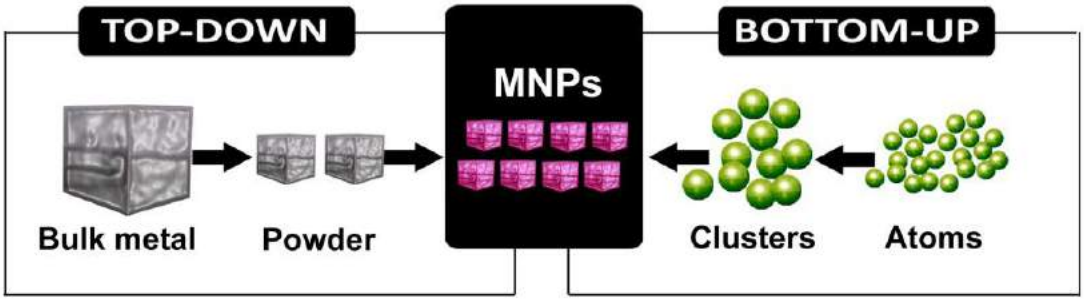

Figure 3.1: Different approaches for synthesis of nanostructure [182].

Mostly top down is difficult approach for synthesis of nanomaterials as it requires expensive equipment, time and energy to break bulk materials. This approach includes: lithography process, ball milling method, printing and skiving etc. On the other hand, the bottom up approach is an easy and economically favorable as it requires low cost raw materials. In this approach, the fabrication of nonmaterial is carried out by agglomeration of atom to atom or molecule to molecule [139].

In bottom up approach, the co-precipitation route is cheap, facile and less time consuming. In this procedure, the metal salt precursors like (chlorides, nitrates, and sulphates etc.) are dissolved in required solvent. The precipitating agent like NH_4OH *and NaOH* forms oxohydroxides. Controlled size, morphology and uniform distribution of particles are difficult to achieve by this method. However, the use of required quantity of surfactant controlled the synthesis parameters such as; *pH* value, reaction time and dropping rate. The basic medium in metal salt solution is observed to be beneficial in achieving uniform distribution with controlled size and morphology.

In this research work, the synthesis process for $CuFe_2O_4$ and *MOs* nanostructures is demonstrated separately in flow chart as shown in *Figure 3.2 (a and b)*.

This high crystallinity of $CuFe_2O_4$ nanoparticles and *MOs* nanostructures were obtained after calcinations at 600 ^oC, that reduce the structural defects and disorders in the lattice and also control the particle size.

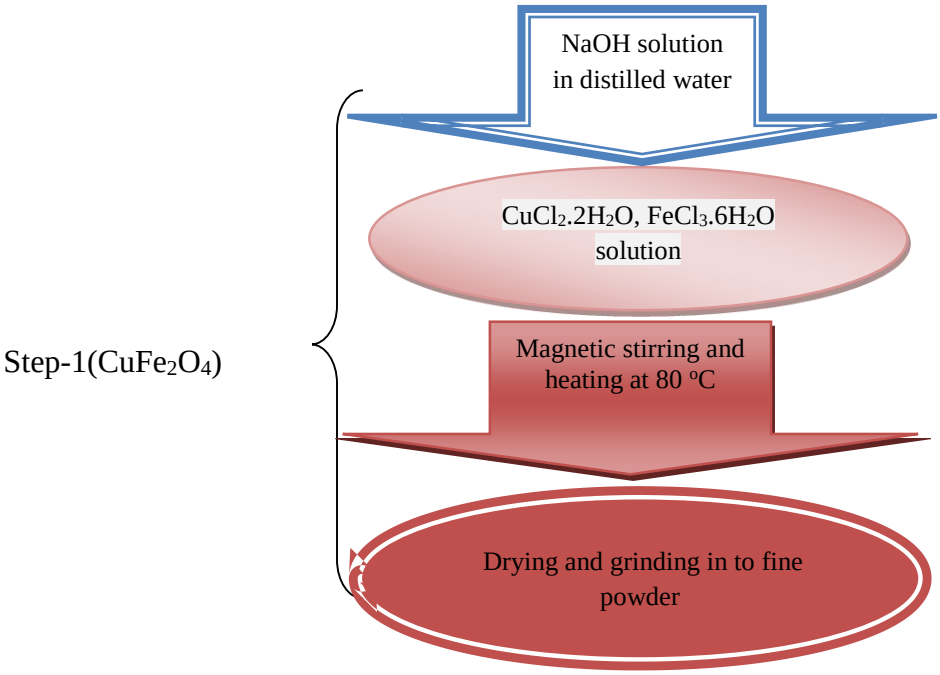

Figure 3.2 (a): Step-1: Formation of $CuFe_2O_4$ nanoparticles

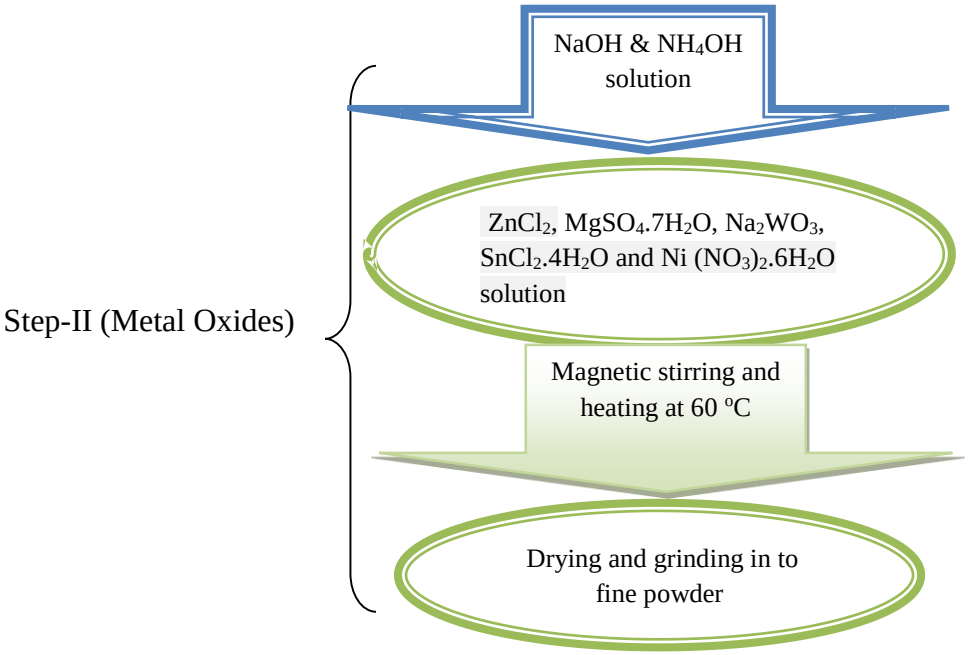

Figure 3.2 (b): Step-II: Formation of MOs nanostructures

Table - 3.1: Chemicals used for synthesis of nanocomposites

Chemicals	Formula	Molecular Weight (g/mol)	Supplier
Copper chloride	$CuCl_2.2H_2O$	170.48	Merck
Iron Chloride	$FeCl_3.6H_2O$	270.30	Merck
Zinc Chloride	$ZnCl_2$	136.30	Merck
Stannous Chloride	$SnCl_2.5H_2O$	279.62	Merck
Magnesium Sulphate	$MgSO_4.7H_2O$	246.47	Merck
Sodium Tungstate	Na_2WO_3	293.816	Merck
Nickle Nitrate	$Ni(NO_3)_2.6H_2O$	290.79	Merck
Sodium Hydroxide	NaOH	40	Sigma Aldrich
Ammonium Hydroxide	NH_4OH	35.04 (30-32%)	Sigma Aldrich
Hydrochloric Acid	HCl	36.45(35-37%)	Sigma Aldrich

3.2 Synthesis of $CuFe_2O_4$ Nanoparticles

0.2M (25ml) solution of $CuCl_2.2H_2O$ and 0.4M (25ml) solution $FeCl_3.6H_2O$ were prepared in distilled water that prevent the accumulation of contaminations in final solution.

$$CuCl_2.2H_2O + H_2O \rightarrow Cu^{2+} + nOH^- + 2Cl^- \quad (3.1)$$

$$FeCl_3.6H_2O + H_2O \rightarrow Fe^{3+} + nOH^- + 3Cl^-$$

3M aqueous solution of NaOH is used as a precipitating agent and added drop wise under constant magnetic stirring in former solution until a pH value of 12-13 was achieved.

$$NaOH + H_2O \rightarrow Na^+ + 2OH^- \quad (3.2)$$

$$Cu^{2+} + 2Fe^{3+} + 8OH^- + Cl^- + Na^+ \rightarrow Cu(OH)_2 + 2Fe(OH)_3 + NaCl\downarrow$$

The acquired light brown precipitate was heated under continuous magnetic stirring at 80 ^{o}C for one hour. The solution was centrifuged and black brown precipitates were washed to remove impurities in the final contents.

$$Cu(OH)_2 + 2Fe(OH)_3 \rightarrow CuFe_2O_4 + nH_2O \quad (3.3)$$

3.3 Synthesis of Metal Oxide (MOs) Nanostructures

3.3.1 Synthesis of ZnO Nano discs

0.2M (100 ml) solution of *$ZnCl_2$* was synthesized in deionized water and *1M (100 ml)* solution of *NaOH* as precipitating agent was added under uniform magnetic stirring until a *pH* value *8* was achieved. After adjusting *pH*, the precipitates were stirred for one hour at *300 rpm* at *60* ^{0}C and collected by centrifugation. To remove impurity contents, the precipitates were washed with ethanol. The precipitates were dried at *80* ^{0}C, grinded into fine powder and sintered at *600* ^{0}C for *5* hours.

$$ZnCl_2 + H_2O \rightarrow Zn^{2+} + nOH^- + 2Cl^- \quad (3.4)$$

$$NaOH + H_2O \rightarrow Na^+ + 2OH^-$$

$$Zn^{2+} + 2OH^- + 2Cl^- + 2Na^+ + 2OH^- \rightarrow Zn(OH)_2 + 2H_2O + 2NaCl$$

$$Zn(OH)_2 \rightarrow ZnO + H_2O$$

3.3.2 Synthesis of MgO Nanoparticles

The *MgO* nanoparticles were synthesized by wet chemical method in which *0.2M* (100 ml) solution of $MgSO_4.7H_2O$ was prepared and 1M (100 ml) solution of NaOH was added under constant magnetic stirring. The white colored precipitates were formed. After adjusting pH value to 9, the addition of NaOH was stopped. The precipitates were stirred for one hour at 300 rpm at 60 ^{0}C and were collected by centrifugation. The acquired sample was grinded and sintered at 600 ^{0}C for 5 hours to develop the nanoparticles of *MgO*.

$$MgSO_4.7H_2O + 2NaOH + H_2O \rightarrow Mg(OH)_2 + Na_2SO_4 + H_2O \quad (3.5)$$

$$Mg(OH)_2 \rightarrow MgO + nH_2O$$

3.3.3 Synthesis of WO_3 Nanoplates

The nanoplates of *WO_3* were prepared by co-precipitation method. 0.1M solution of $Na_2WO_4.2H_2O$ was synthesized with NaCl in deionized water and required *pH* was achieved by adding (3M) HCl solution under constant magnetic stirring. The yellowish green precipitates were formed. Precipitates were washed and dried to remove the water contents. Na_2WO_4 solution transformed into H_2WO_4 upon addition of HCl at adjusted *pH*. The chemical reaction for synthesis of WO_3 nanoplates is given below.

$$Na_2WO_4 + 2HCl \rightarrow H_2WO_4 + 2NaCl \quad (3.6)$$

$$H_2WO_4 \rightarrow WO_3 + H_2O$$

3.3.4 Synthesis of SnO_2 Nano Spindles

The spindle shape *SnO_2* nanostructures were synthesized by wet chemical route. 0.2 M (100 ml) solution of $SnCl_2.4H_2O$ was prepared in deionized water. The 0.5M (50 ml) solution of NH_4OH was added drop wise under constant magnetic stirring. After adjusting *pH*, the acquired precipitates were heated at 60 ^{0}C for one hour at 300 rpm. The acquired precipitates were washed and dried. The drying was carried out at 60 ^{0}C for 12 hours. The dried sample was grinded and annealed at 600 ^{0}C for 5 hours to get the SnO_2 nanospindles.

$$SnCl_2.5H_2O + H_2O \rightarrow Sn^{2+} + nOH^- + 2Cl^- \quad (3.7)$$

$$NH_4OH + H_2O \rightarrow NH^{4+} + OH^-$$

$$Sn^{2+} + nOH^- + 2Cl^- + 2NH^{4+} + OH^- \rightarrow Sn(OH)_2 + nH_2O + 2NH_4Cl$$

$$Sn(OH)_2 \rightarrow SnO_2 + nH_2O$$

3.3.5 Synthesis of NiO Nanoparticles

0.2M (25 ml) solution of Ni $(NO_3)_2.6H_2O$ was synthesized in deionized water. 3M (25ml) aqueous solution of NH_4HCO_3 was added dropwise in former solution under constant magnetic stirring to adjust *pH* from 9-11. Light green color precipitates were formed which were heated at 60 ^{0}C for 30 minutes. The acquired precipitates were dried at 100 ^{0}C to remove the water contents. The dried sample was grinded and sintered at 600 ^{o}C for 5 hours.

$$Ni\,(NO_3)_2\,.6H_2O + H_2O \rightarrow Ni^{2+} + NO^{3-} + OH^- \qquad (3.8)$$

$$NH_4HCO_3 + H_2O \rightarrow NH_4OH + H_2CO_3$$

$$Ni^{2+} + NH_4OH + NO^{3-} \rightarrow 2Ni\,(OH)_2 + H_2O + NH_4NO_3$$

$$Ni\,(OH)_2 \rightarrow NiO + H_2O$$

3.4 Synthesis of $CuFe_2O_4$/MOs Nanocomposites

The synthesized powder of *MOs* (*M=Zn, Mg, W, Sn and Ni*) nanostructures were mixed with different weight fractions (10-50 wt. %) of *$CuFe_2O_4$ MNPs*. This mixed powder was grinded till homogenization and annealed to achieve required phase of nanocomposites for further characterization. The flow chart in *Fig. 3.3* demonstrates the synthesis process for this nanocomposite.

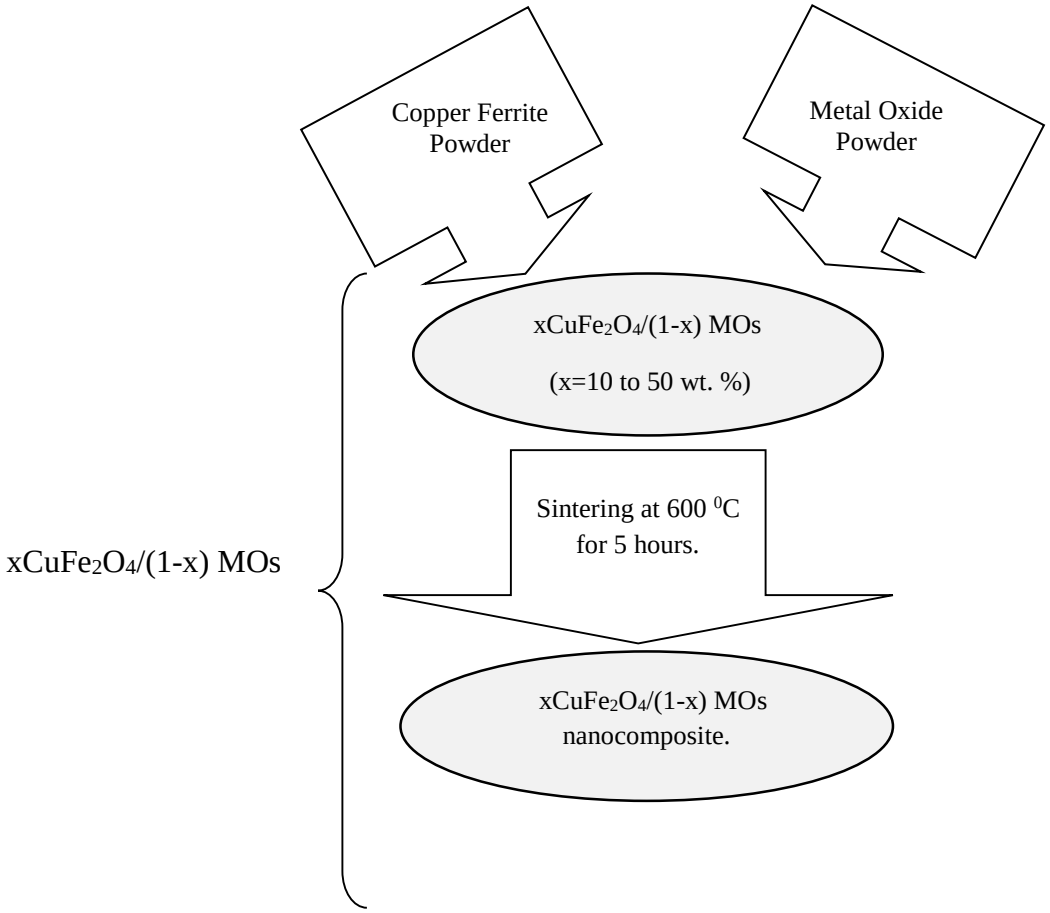

Figure 3.3: Flow chart for formation of $CuFe_2O_4$/MOs nanocomposite.

3.5 Experimental Techniques

In this section, the prepared nanocomposites were characterized through different experimental techniques to investigate their structural and physical properties.

3.5.1 X-ray Diffractometer (XRD)

XRD is a fundamental, useful and multipurpose experimental technique, being extensively applied for the analysis of *(a)* spacing between different planes of atoms *(b)* orientation of grains (*c)* crystal structures, lattice constant and volume of unit cell *(d)* shape and size of small crystalline regions *(e)* qualitative and quantitative analysis of existing phases. The *x-rays* are used in *XRD* for the material analysis, which are created when highly accelerated electrons strike a heavy metal target. The *x-ray* tube consists of a source of electrons which are accelerated by very

high voltage applied between the cathode (*W*) and the anode (metal target). The anode is cooled down by circulating cold water as shown in *Fig. 3.4.*

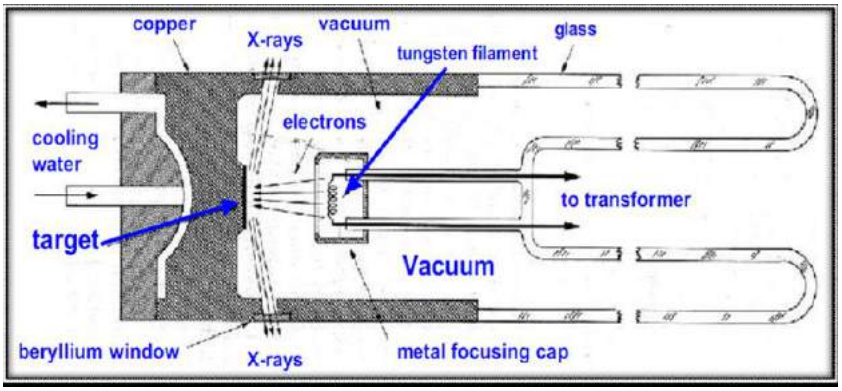

Figure 3.4: Schematic diagram of X-ray tube [140].

x-rays are *EM* waves that have wavelength equivalent to the inter-atomic distances of the materials. The atomic planes of a crystal behave like a diffraction grating for *x-rays* and interfere with one another after passing through crystal and undergo diffraction at Bragg's angle as shown in the *Fig. 3.5*. The constructively interfered x-rays enhance the amplitude, and hence, the intensity of diffracted beam and produce discrete diffraction peaks at particular position (angles) which are recorded by a detector as shown in *Fig. 3.5.* In nature, each material has its intrinsic diffraction peaks positioned at distinct angles which discriminate it from other materials. Hence, X-ray data provides the fingerprint of the material and an unidentified compound can be recognized by this diffraction technique. In this research, *X-ray* diffractometer (*model JDX-11, of JEOL Company Ltd. Japan*) operated at 40 kV and 30 mA with *Cu* K_α (1.5406 Å) was used. The *XRD* patterns of pristine $CuFe_2O_4$, *MOs* nanostructures and their nanocomposites has been obtained, from $2\theta = 20^o$ to 80^o with 0.025^o increment in the angle with 0.4 sec per step stay time.

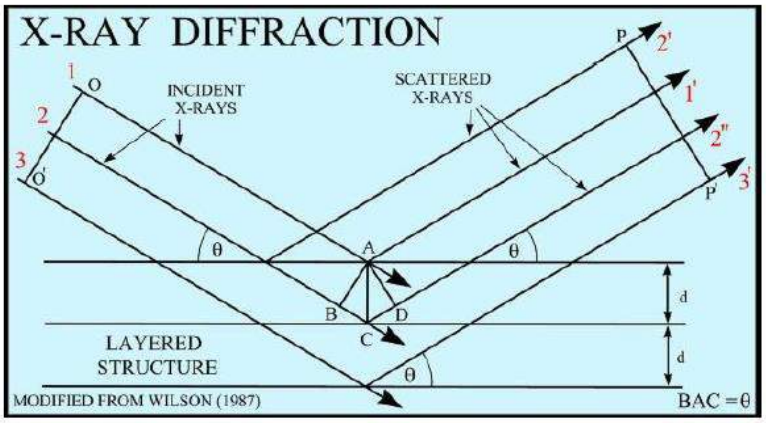

Figure 3.5: Diffraction Pattern of X-ray from material [140].

3.5.2 Fourier Transforms Infrared Spectroscopy (FTIR)

FTIR is an experimental tool based on Michelson interferometer, which is mostly used to investigate the vibrational modes of many organic materials, inorganic materials, polymers, lubricants and coatings etc. Presence of functional groups attached to biological materials and identification of different phases in a nanocomposite is also carried out using *FTIR*.

The *FTIR* spectrometer is basically comprised of a beam splitter, a fixed mirror and a moveable mirror that can move backward and forward. The beam splitter is half coated with silver, so that it transmits half of the *IR* beam incident on it and reflects the remaining half. The schematic diagram of *FTIR* is shown in *Fig. 3.6.*

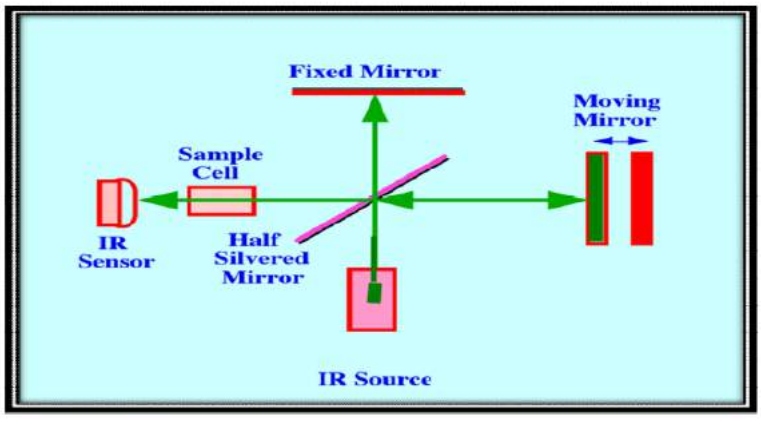

Figure 3.6: Schematic diagram of the FTIR spectrometer [141]

A beam of infrared radiation is focused by using optical techniques and is permitted to pass through the sample. Depending upon the composition of material; some part of radiation is absorbed and the remaining one is passed through it. The absorbed radiation induces vibrational excitation of polar bonds in the materials. The graph between radiations absorbed versus *IR* frequency gives *FTIR* spectra which encompasses evidence associated to the vibrational modes exist in the material. This absorption pattern is unique for almost every compound. From this absorption pattern of light, identification of the composition can be made.

In this research work, presence of *MOs* nanostructures in $CuFe_2O_4$ composite has also been confirmed by *FTIR* (*IR Tracer -100r made by Shimadzu*) analysis, which gives the M-O,M-O-M (*M = Zn, Mg, W, Sn and Ni*) vibrational modes along with characteristics tetrahedral and octahedral vibrational modes of cation present in ferrites. The measurements were performed by preparing a pellet of 12 mm diameter (using Hydraulic Presser) containing 0.02 % of powder sample and 0.98 % of KBr powder. The spectrum of prepared sample was obtained from 400 cm^{-1} to 4000 cm^{-1}. The spectrum obtained by this spectroscopy technique is subjected to analysis as shown in *Fig. 3.7.*

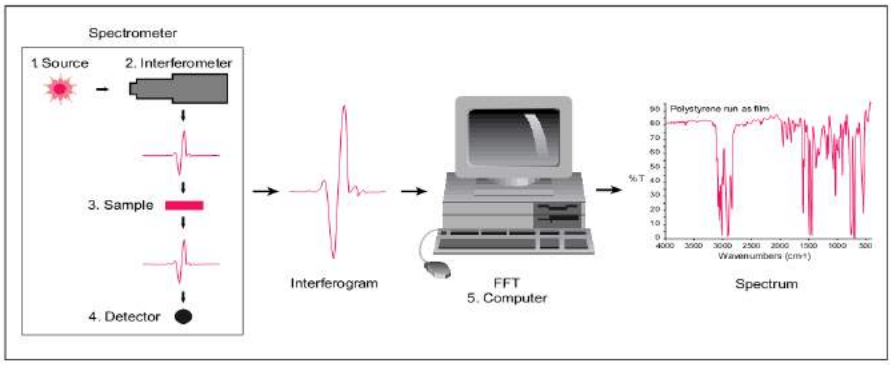

Figure 3.7: The FTIR Spectrometer [142].

3.5.3 Scanning Electron Microscopy (SEM)

The particle size and morphology of the nanostructure materials play an important role in defining their various applications in engineering and technology.

The surface morphology, particle size and their distribution can be obtained by *SEM* analysis, which uses highly energetic beam of electrons with energy range 0.2 k eV to 40 k ev emitted from an electron gun by thermionic emission and focused on a material which is placed in vacuum chamber. This beam of electrons interacts with the material and dissipates energy through different interacting mechanism. This beam of electron produces several kinds of secondary particles and radiation in the form of a signal from the material. The obtained signal is recognized by a detector attached with the system computer shown schematically in *Fig. 3.8 and* the secondary electrons provide the descriptions of the surface structure of the specimen.

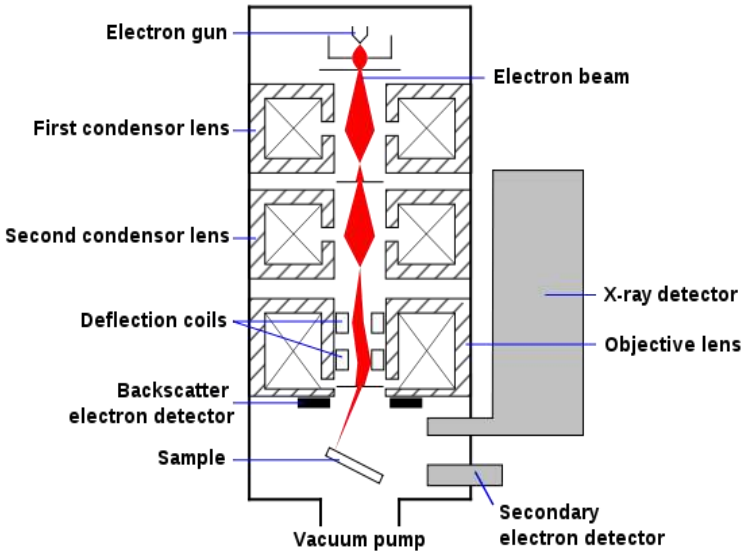

Figure 3.8: Schematic representation of SEM [143].

3.5.4 Transmission Electron Microscopy (TEM)

In this technique the accelerated beam of electrons (up to 1*Mev*) is projected on a ultrathin sample that interacts with the material during transmission. During this interaction of electron with material, a magnified image is obtained that focused on to a fluorescent screen. *TEM* are proficient

of imaging at considerably higher magnification than that of ordinary light microscopes, due to small de-Broglie wavelength, λ, of electron and is given as:

$$\lambda = \frac{h}{\sqrt{2mqv}}$$

Where m and q are mass and charge on electron, h is Plank's constant, and V is applied potential difference.

TEM are mostly used to extract information about nanostructure materials like: *(a)* morphology, in which particle size of nanostructure materials, shape of nanostructures/particles and their distribution in the sample can be determined. *(b)* crystallographic information, in which distribution of atoms in the sample and their degree of order and defects in areas of few nanometers can be determined, *(c)* compositional information, if *TEM* is equipped with this extra setup i.e. *EDX*, then; the composition of elements and compounds present in the sample with their relative weight ratio, can be obtained.

In this study, the *TEM* analysis was performed by *Philips EM-400*, using electron accelerating voltage of 60 kV. *Fig. 3.9* gives schematic diagram of *TEM*. During *TEM* measurements, the material were dispersed in ethanol and a small amount of solution were poured on a copper coated mesh called *TEM* grid. The image on fluorescent screen gives the morphology and the grain sizes are calculated from these images.

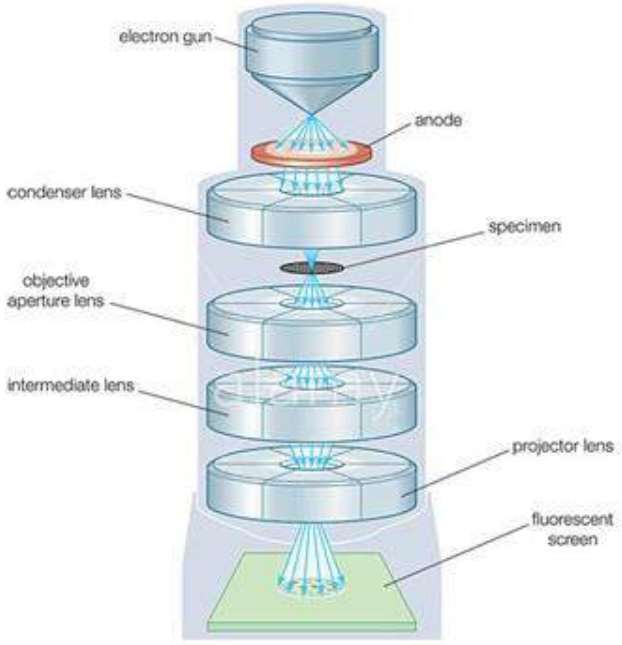

Figure 3.9: Schematic representation of TEM [144].

3.5.5 Vibrating Sample Magnetometer (VSM)

VSM works on the principle of Faraday's law, which state that, "the change in linking magnetic flux through a coil induces a voltage or an emf in a coil". The voltage induced in a coil with n number of turns and cross sectional area a is:

$$V = -na\frac{dB}{dt} \tag{3.10}$$

When the coil is placed in a uniform magnetic field B, then

$$B = \mu_o H \tag{3.11}$$

When a material having magnetization M is placed inside a coil then the magnetic field becomes,

$$B = \mu_o(H + M) \tag{3.12}$$

The resultant change in flux is $\Delta B = \mu_o M$ (3.13)

Combining Eqs. *(3.1) and (3.4)* gives

$$Vdt = -na\mu_o M \tag{3.14}$$

Equation 3.5 shows that, the output signal of coil directly depends on magnetization *M* and is free from the magnetic field *B*.

In *VSM*, the sample is attached to a vibrating rod subject to sinusoidal motion with a constant frequency, and an emf is induced in the pickup coils as shown in *Fig. 3.10***.** In this research work the magnetic properties were measured under an applied field of ± 2 *Tesla* using *VSM* (*Model BHV-50 of Riken Denshi Co. Ltd. Japan*). A vertical sample rod is connected with sample holder with transducer assembly positioned along the *z*-axis. The sample is exposed to a vibrational motion and coils pick up the signal, produced from the vibration of magnetic sample.

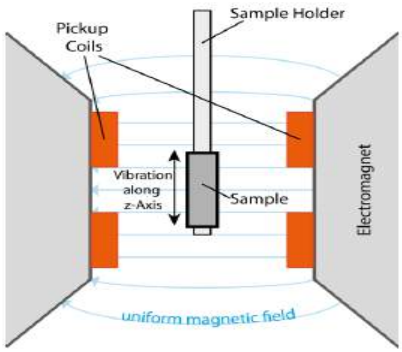

Figure 3.10 Schematic Diagram of VSM [145]

3.5.6 Electromagnetic Absorption Measurement

The *EM* absorption properties of nanocomposites have been measured by two ports Vector Network Analyzer (*VNA*) as shown in *Fig. 3.11*. In this setup, the antenna-1 transmits an input signal of certain frequency (2-10 *GHz*), which is passed through the material under investigation. Depending upon the dielectric and magnetic properties of material, some portion of wave is

transmitted through the material and received at antenaa-2, while remaining part is reflected back to antenna-1. The reflected portion of signal is again recollected at antanna-1.

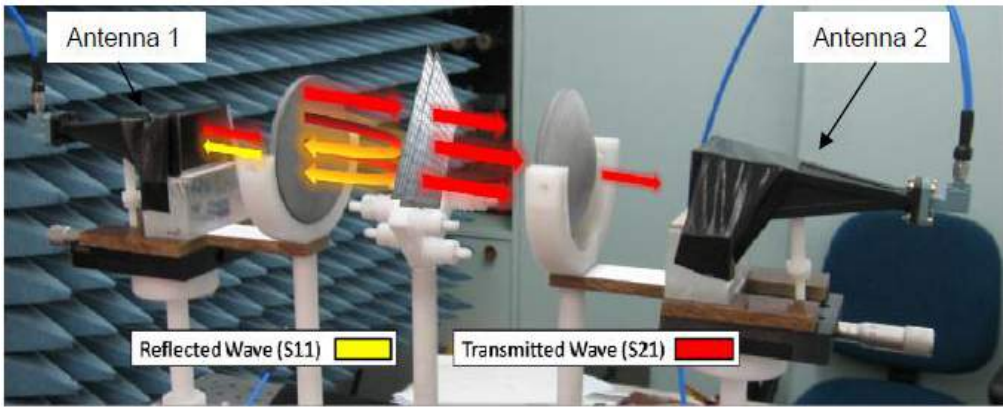

Figure 3.11: Free-space measurement setup operting at G Hz frequency range [147]

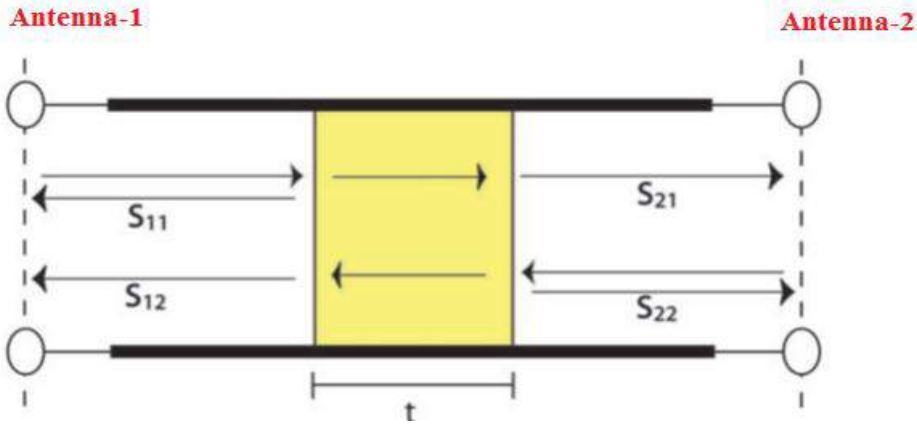

Figure 3.12: Plane representation of the S-parameters [148]

The *VNA* then sweeps in given frequency range and collect the reflected and transmitted signals simultaneously. This is completed in both directions, i.e. input signal from antenna-2 to antenna-1, thus four sets of data are produced. This can be mathematically symbolized by four complex scattering parameters: S_{11}, S_{21}, S_{22} and S_{12} respectively as shown in *Fig. 3.12*.

The reflected (P_R) and transmitted (P_T) powers linked with above *S* parameters are denoted as:

$$P_R = |S_{11}|^2 = |S_{22}|^2 \quad (3.19)$$

$$P_T = |S_{12}|^2 = |S_{21}|^2 \quad (3.20)$$

Thus, the absorbed power P_A can be calculated by taking the incident power P_I is 1 mW as:

$$P_A = 1 - P_R - P_T = 1 - |S_{11}|^2 = |S_{22}|^2 \quad (3.21)$$

When the wave is incident on the surface of sample and passes through it, these S-parameters can be suitably evaluated to obtain the overall shielding efficiency as:

$$SE_T = 10log\frac{P_I}{P_T} = SE_R + SE_A = 10log\frac{1}{|S_{21}|^2} \quad (3.22)$$

$$SE_R = 10log\frac{P_I}{P_I - P_R} = 10log\frac{1}{1-|S_{11}|^2} \quad (3.23)$$

$$SE_A = 10log\frac{P_I - P_R}{P_T} = 10log\frac{1-|S_{11}|^2}{|S_{21}|^2} \quad (3.24)$$

The complex permittivity and permeability of samples can be obtained by using an algorithm based Nicolson-Ross-Weir method [149] with the built-in software.

Concisely, given that $S_{12} = S_{21}$, the S-parameters can be articulated as a function of the reflection (Γ) and transmission (T) coefficients by [150],

$$S_{11} = R_1^2\left[\frac{\Gamma(1-T^2)}{(1-\Gamma^2T^2)}\right] \quad (3.25)$$

$$S_{22} = R_2^2\left[\frac{\Gamma(1-T^2)}{(1-\Gamma^2T^2)}\right] \quad (3.26)$$

$$S_{21} = R_1R_2\left[\frac{T(1-T^2)}{(1-\Gamma^2T^2)}\right] \quad (3.27)$$

Where R_1 and R_2 are coupled to the reference planes and their distance to the sample ends from each side of the antennas. Here Γ is represented by the complex propagation constant (γ) within the material, t is the thickness of the slab and μ is its complex magnetic permeability respectively [151].

$$T = e^{-\gamma t} \quad (3.28)$$

$$\Gamma = \frac{\left(\frac{\gamma_o}{\mu_o} - \frac{\gamma}{\mu}\right)}{\left(\frac{\gamma_o}{\mu_o} + \frac{\gamma}{\mu}\right)} \tag{3.29}$$

Where γ_o is the propagation constant in vacuum. Similarly, the complex propagation constant related to the complex permittivity ε and permeability μ of the sample is found by:

$$\gamma = j\sqrt{\mu_r}\varepsilon_r \frac{2\pi f}{c_o} \tag{3.30}$$

Hence, solving this complex matrix through the Nicolson-Ross-Weir algorithm enables the *VNA* to retrieve the four unknowns: ε', ε'', μ' and μ''.

Chapter No. 4

Structural, Morphological and Magnetic Study of MOs Nanostructures

4.1 Introduction

MOs nanostructures, display metallic, semiconductor and insulating behavior depending upon their electronic structures. *MOs* nanostructures standout among the most multipurpose groups of semiconductor nanostructures and are distinguished as one of the most familiar, versatile, and perhaps the plentiful classes of materials due to their broad structural and physicochemical characteristics. In recent years, the study of *MOs* nanostructures has become the hot topic of research for materials scientists and engineers.

Their distinctive and tunable properties with different weight percent loading of ferrites, graphene and polymers make them enable to be used in optical, optoelectronic and photochemical technology. The *MOs* and their nanocomposites are mostly used in fuel cells, battery electrode in supercapacitors, chemical sensors, *LASER*, waveguides, infrared (*IR*) absorbers, *MW* absorption, superconductor and magneto- resistance etc. Hence it is important to examine the structural and morphological study which depends strongly on the properties of synthesized nanocomposite for the required application.

The structural and morphological analysis of synthesized *MOs* nanostructures **(***ZnO, MgO, WO_3, SnO_2, and NiO*) were performed by *XRD, SEM* and *FTIR* techniques. Furthermore, the magnetic properties of *MOs* nanostructures also depend on morphology and particle dimension. The *MOs* nanostructures show ferromagnetic behavior at nanoscale due to oxygen vacancies and uncompensated spins at the surface. On the other hand, these *MOs* nanostructures show diamagnetic behavior in bulk form. Therefore, to analyze the magnetic response, the hysteresis loops of *MOs* nanostructures were obtained at room temperature.

4.2 Structural and Morphological Study

The crystal structure and purity of phases of prepared material were analyzed by the powder *XRD* technique. The *XRD* pattern of pristine $CuFe_2O_4$ and *MOs* (*ZnO, MgO,* WO_3, SnO_2, *and NiO*) nanostructures are shown in *Fig. 4.1* and *4.2* respectively.

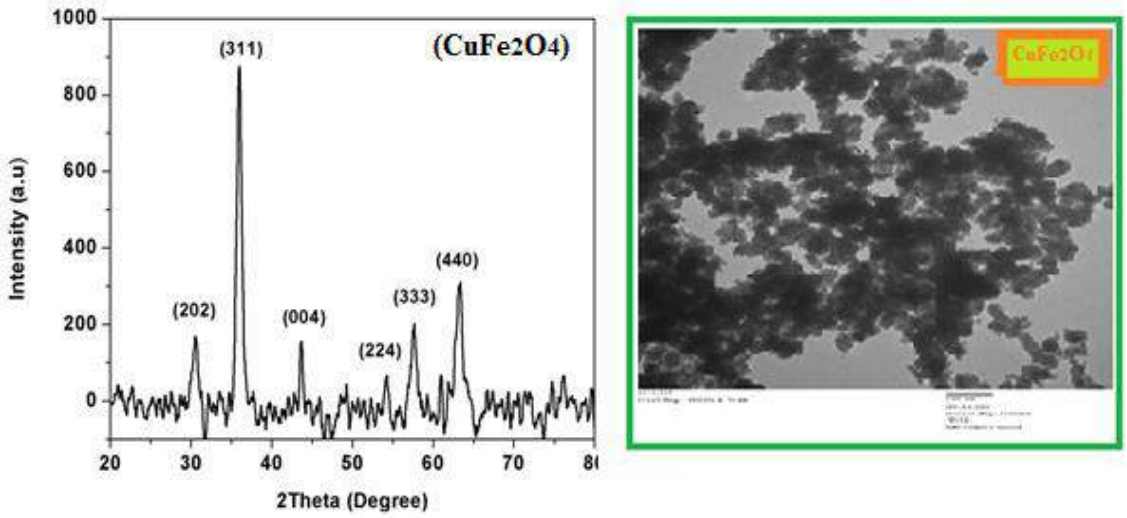

Figure 4.1: XRD pattern and TEM image of pristine $CuFe_2O_4$ MNPs.

The *XRD* pattern shown in *Fig. 4.1* demonstrate the formation of $CuFe_2O_4$ with tetragonal structures. The *TEM* image demonstrates the spherical morphology of *MNP* with size lying in the range of 25-30 nm. The *TEM* image also reveals that $CuFe_2O_4$ *MNPs* are agglomerated due to magnetic interaction. *Figure 4.2* demonstrate the *XRD* patterns of *MOs* nanostructures and the peaks position are well indexed to the characteristic wurtzite, cubic rock salt type, monoclinic, rutile type, tetragonal and face-centered cubic structure of *ZnO, MgO,* WO_3, SnO_2 *and NiO* respectively [152-156]. Moreover, the contraction in diffraction peaks in *Fig. 4.2* demonstrates the increase in grain size which was calculated using *Eq.4.1* and lies in the range of 30-80 nm.

$$D = \frac{K\lambda}{\beta_{hkl}\cos\theta} \tag{4.1}$$

Where λ is the wavelength of x-ray, β is full width at half maximum at diffracting angle θ.

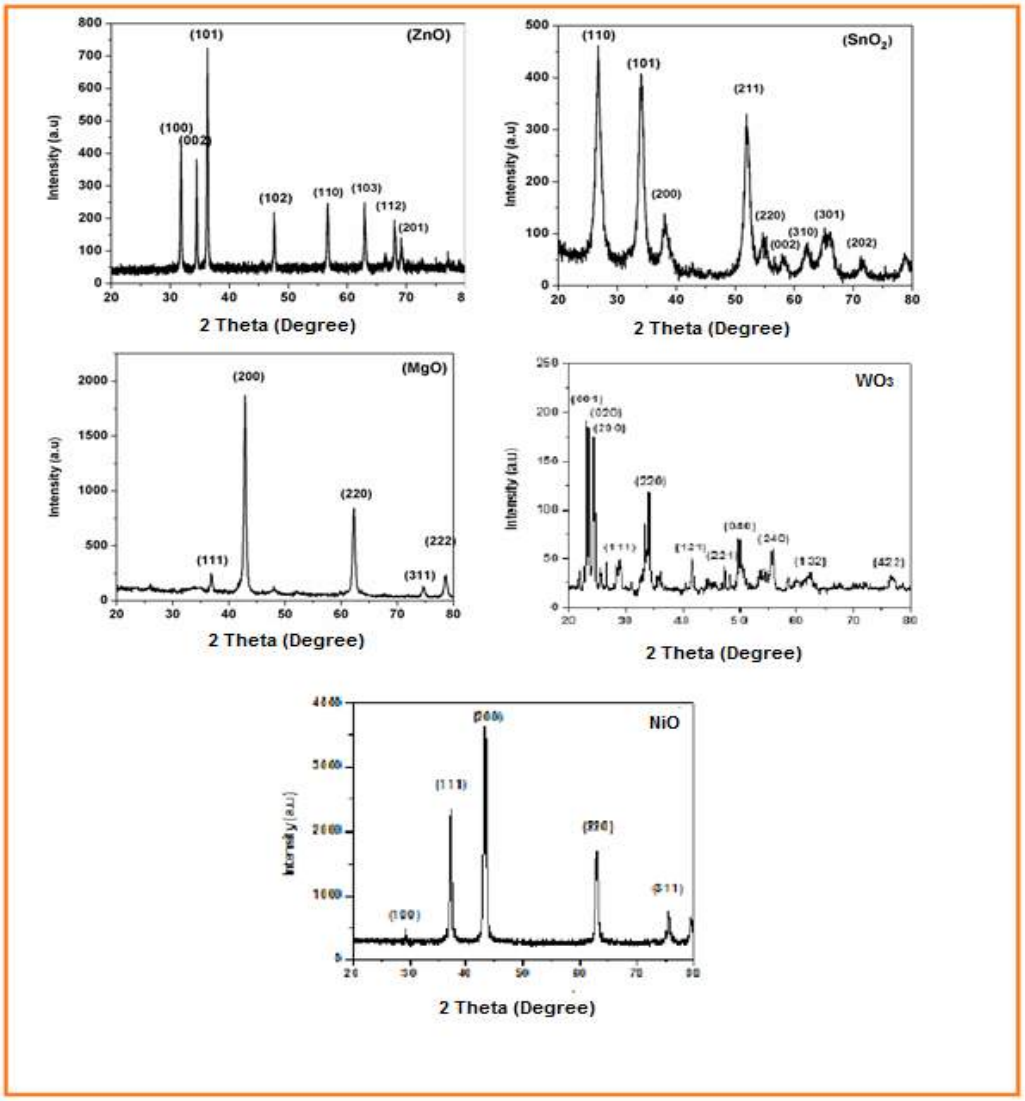

Figure 4.2: XRD patterns of MOs (M=Zn, Sn, W, Mg, and Ni) nanostructures.

The different morphology of nanomaterial shows distinct behavior which can be tailored for required application in different areas of engineering and medical. The morphology of the *MOs* nanostructures were investigated by *SEM* analysis. Figure 4.3 demonstrate the *SEM* images of selected *MOs* nanostructures.

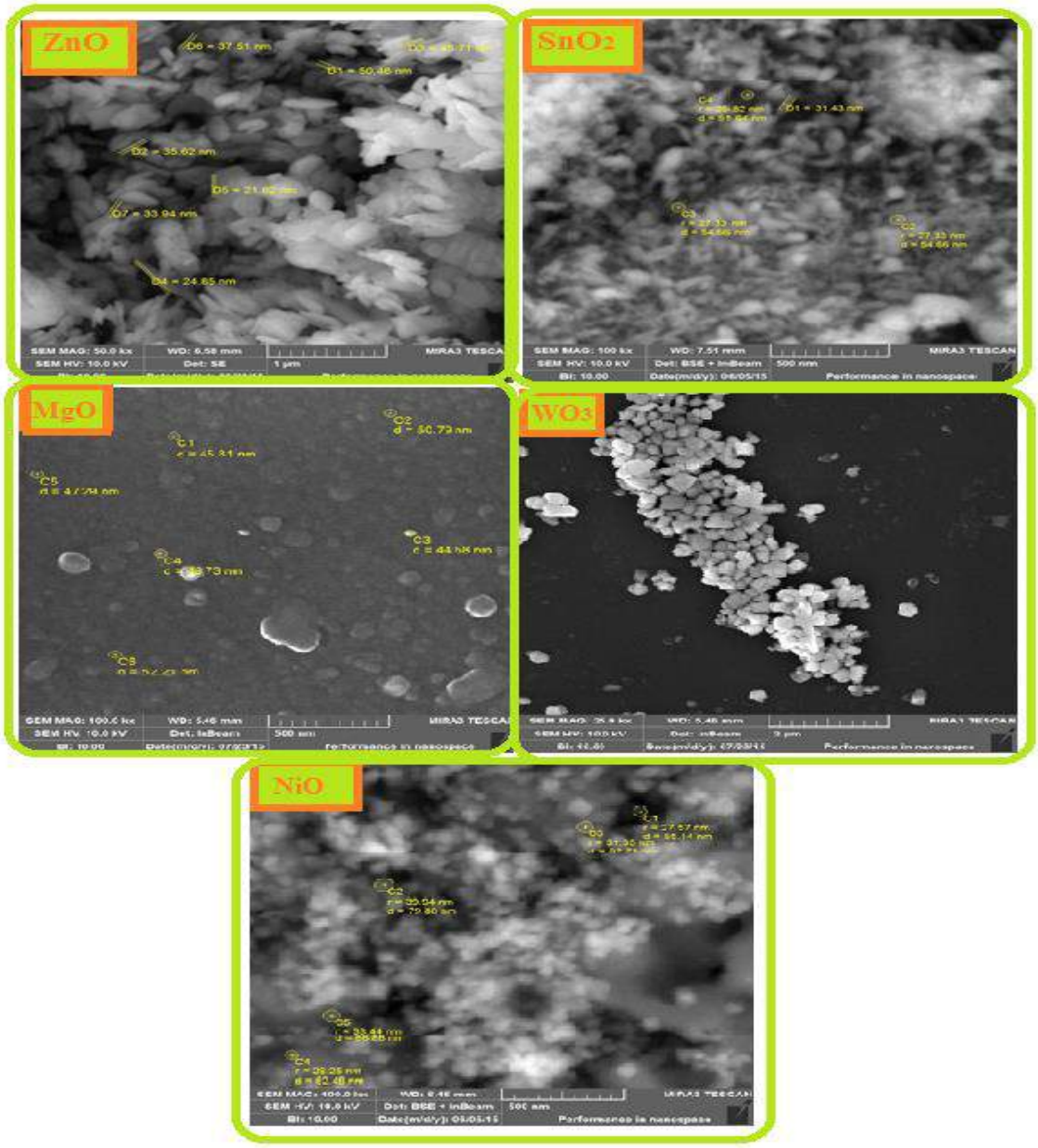

Figure 4.3: SEM images of MOs (M=Zn, Sn, W, Mg and Ni) nanostructures.

The *SEM* images show that the *MOs* nanostructures have different morphologies due to difference in oxygen vacancies during calcination process: *MgO* and *NiO* exhibit spherical morphology with uniform size distribution. Whereas *ZnO* shows nanodiscs like shape, SnO_2 has spindle like shape and WO_3 reveals nanoplatelets like nanostructures as shown in *Fig. 4.3*.

4.3 Vibrational Analysis of MOs Nanostructures

Nanostructures materials have a large percentage of atoms at the surface as compared to their bulk, this high surface area become more important at the nanoscale. This property makes nanostructures chemically more reactive. Therefore, the comprehensive analysis of the surface of *MOs* nanostructures is very crucial to extract the information of functional groups and vibration of different metal ions attached to the surface. Therefore, the presence of functional groups and different element was confirmed by *FTIR* analysis. *Figure 4.4* illustrate the *FTIR* spectra of *ZnO, SnO_2, MgO, WO_3,* and *NiO* nanostructures in the range of 400-1500 cm^{-1}.

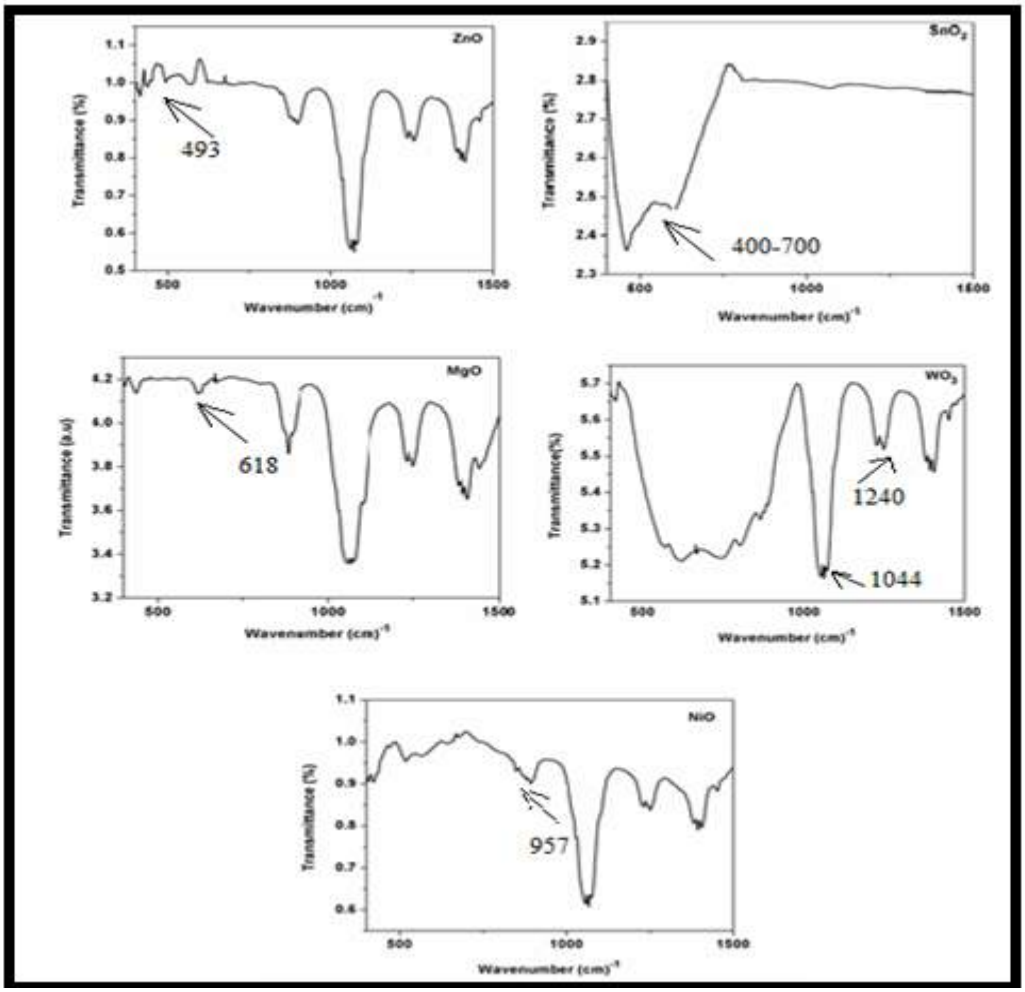

Figure 4.4: FTIR Spectra of MOs (M=Zn, Sn, W, Mg, and Ni) nanostructures.

The existence of different vibrational modes, in all samples, depicts the presence of *M-O* bonding (*M = Zn, Sn, W, Mg, and Ni*) [154-157]. Hence, the *FTIR* results also support the previous *XRD* patterns of *MOs* nanostructures.

4.4 Magnetic Study of MOs Nanostructures

Various attempts have been done to investigate the magnetic character in different semiconductor materials by adding *3d* transition metals [155]. The room temperature ferromagnetism (*RTFM*) in these semiconductor materials is due to the hybridization between the *3d* state of the magnetic ions and the *2p* state of oxygen ions [156]. But, the situation is quite changed by the manifestation of unpredicted ferromagnetic (*FM*) behavior in pure *MOs* nanostructures [156]. This type of magnetism has been characterized as d^0 ferromagnetism that originates from moments produced by vacancies and surface defects at nanoscale. [157]. However, many scientific work have been published on *RTFM* in *MOs* nanostructures, but, the ultimate evidence of this fact does not exist until now. The synchronization of experimental and theoretical research, demonstrate that surface effects and oxygen vacancies play an essential role in producing *RTFM* in these *MOs* nanostructures. These oxygen vacancies depend on the size and morphology of *MOs* nanostructures. Straumal and coworkers suggest that *FM* also originates due to crystal defects like grain boundaries in nano-granular *ZnO* and other *MOs* samples and the magnetic moments are situated at the vacancies exist at the grain boundaries [158]. *Figure 4.5* shows the *M-H* loops of *MOs* nanostructures, which show their ferromagnetic behavior at nanoscale. In this ***Fig.*** the diamagnetic behavior was observed in *ZnO* and SnO_2 nanostructures with size in the range of 22-50 nm already reported in previous work [159-60] The *MgO* nanoparticles show weak ferromagnetism at low field region and reveal diamagnetic behavior at higher field value. Nitesh Kumar et.al observes weak ferromagnetism in *MgO* nanoparticles with size 22 nm having M_s

0.00204 emu/g [161]. Up to our literature study, no magnetic study has been carried out on WO_3 nanoparticles but in this research, WO_3 nanoplatelets shows ferromagnetic behavior with *Ms* value of 0.2 emu/gm and weak ferromagnetic behavior is also observed in *NiO nanoparticles* due to uncompensated spins at the surface of *AFM* lattice [162]. Hence, the shape and size of a material performs a major role to modify the surface areas, that produce the magnetic character in nonmagnetic material.

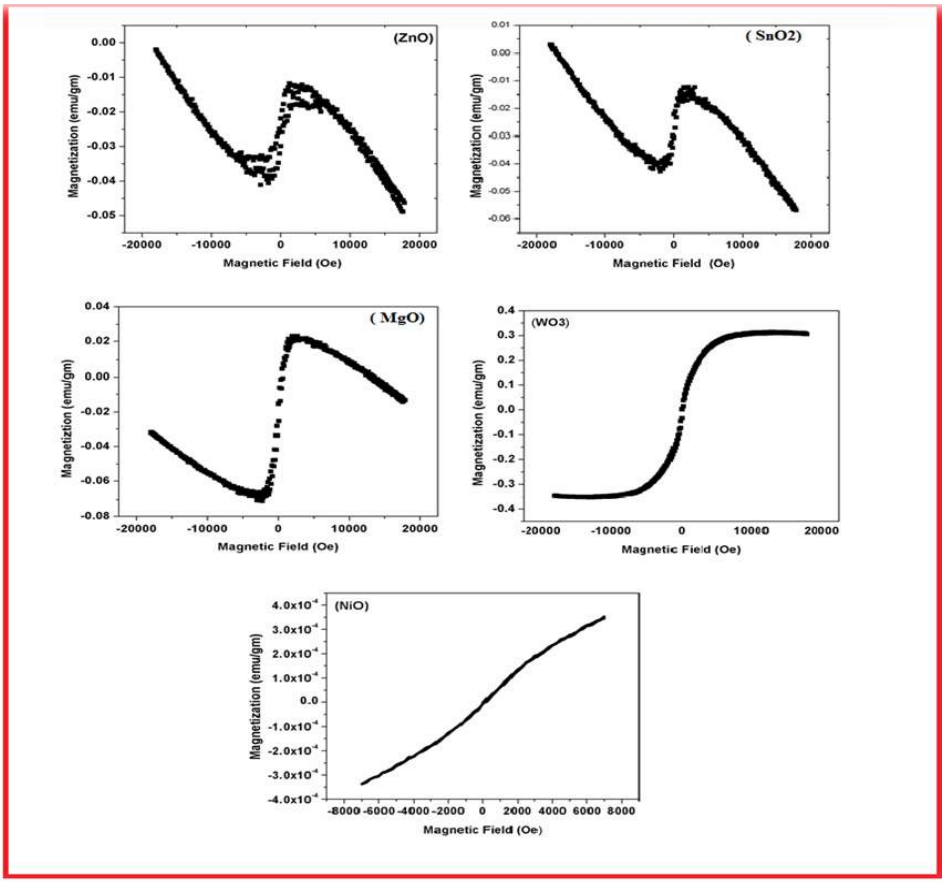

Figure 4.5: M-H loops of MOs (M=Zn, Sn, Mg, W and Ni) nanostructures

Chapter No. 5

Enhancement of Microwaves Absorption Properties of $CuFe_2O_4$ Magnetic Nanoparticles Embedded in ZnO Nanodiscs

5.1 Introduction

Among different materials, ferrites have attained much attention for *EM* shielding application [163]. But high density and low dielectric loss, restricts the application of ferrite in a *EM* absorbing coatings. Moreover, ferrites alone cannot encounter all the necessities such as strong absorption in wide band, thin coating thickness and effective absorption bandwidth [164]. Therefore, to overcome these problems, dielectric loss materials having low density, good thermal stability and low cost production are mixed with ferrite. The Dielectric loss fillers like *MOs* including *TiO_2, SnO_2, CeO_2 and Al_2O_3* have captured colossal care for their excellent *EM* absorption performance [165-174]. Therefore, to accomplish novel *MW* absorbing material, considerable attention has been devoted to magnetic-dielectric hybrid system to balance the *EM* parameters for getting anticipated results.

Among different types of *MOs*, *ZnO* nanostructures have focused the attention of scientists and engineers during last few decades due to their useful application in different sensors, *EM* absorption coatings and different acous-optical devices. [175-180].

In this study, the effect of *ZnO* contents in $CuFe_2O_4$ nanocomposites, stimulated the variations in surface morphology, grain size and physical characteristics. Tailoring physical characteristics of *$CuFe_2O_4$ MNP* via *ZnO* nanodiscs tune the ferromagnetic resonance, eddy current loss, multi-scattering mechanism due to defects and impedance matching. These unique properties make this beneficial for strong attenuation in required frequency band (*2-10 GHz*).

5.2 Results and Discussions

5.2.1 Structural Study

The structural properties and presence of crystalline phases were analyzed by *XRD* pattern. The *XRD* analysis was carried out with step size 0.2° (2 θ) and 2θ range of 20°-80° *Figure 5.1 (a and b)* demonstrate the *XRD* pattern of pristine $CuFe_2O_4$ and *ZnO* nanostructures respectively without any other impurity phases. The observed characteristic diffraction peaks marked well with *JCPDS card (22-1086)* and *(89-1012)* for inverse spinel $CuFe_2O_4$ and hexagonal *ZnO* nanoparticles respectively [181]. The *XRD* pattern of *ZnO*, matches the wurtzite hexagonal *ZnO* structure and diffraction peaks position matched with literature.

The average crystallite size of $CuFe_2O_4$ is 31 nm, while *ZnO* grain size varies from 30 to 81 nm in $ZnO/CuFe_2O_4$ nanocomposite. This increase in crystallite size is attributed to decrease in enthalpy of formation for sample with different contents of *ZnO*. Smaller heat will be liberated, enhancing the molecular concentration at the *ZnO* surface, and hence, improving the grain growth.

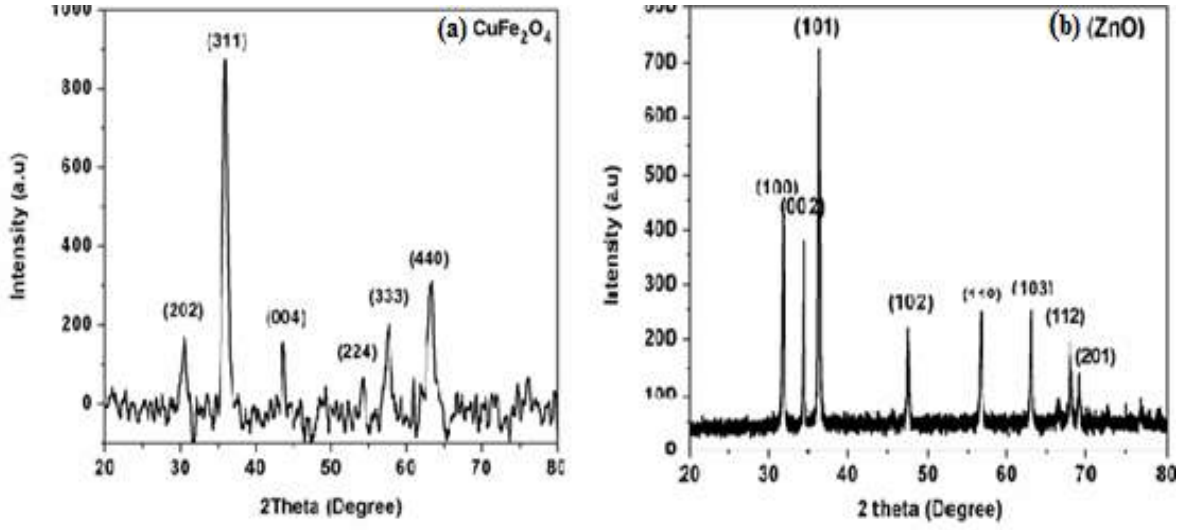

Figure 5.1: XRD pattern of (a) Pristine $CuFe_2O_4$ (b) Pristine ZnO

The *XRD* pattern of $(ZnO)_x/(CuFe_2O_4)_{(1-x)}$ nanocomposites is shown in *Fig. 5.2*, in which both the phases of constituents were observed. Moreover, there is, increase in peaks intensity of *ZnO* phases were also observed. This increase in peaks intensity is attributed to higher concentration of *ZnO*, which produces more crystallite planes for diffraction of x-ray. Thus, obtainability of huge number of diffracted planes strengthens the intensity of diffracted beam, and hence, improves the crystallinity of whole sample.

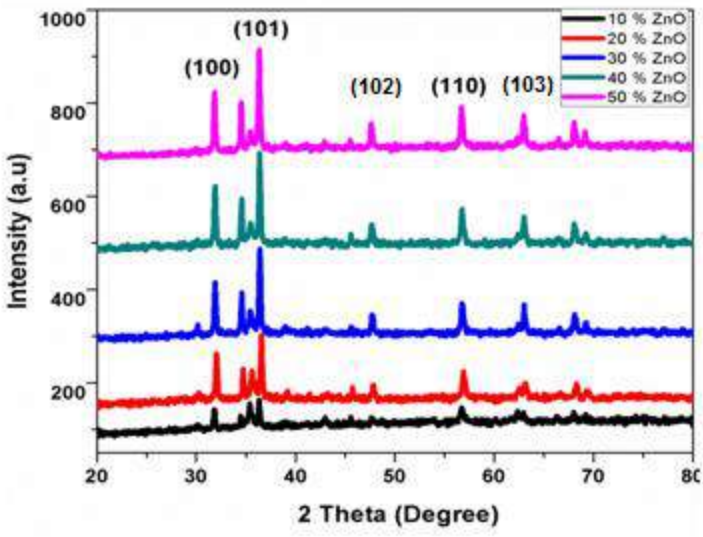

Figure 5.2: XRD pattern of $(ZnO)_x/CuFe_2O_4)_{(1-x)}$ (x=10 to 50 wt.%) nanocomposite.

The lattice parameters for ZnO hexagonal wurtzite structure (a=b, c > a) was calculated by using *Eq. 5.1* [182].

$$\frac{1}{d^2} = \frac{4}{3}\left[\frac{(h^2+hk+k^2)}{a^2}\right] + \frac{l^2}{c^2} \qquad (5.1)$$

Here **d** is the interplanar spacing in Å, and (a, b and c) are the lattice parameters. The values of lattice parameters show that a increase and **c** decreases (*a = 2.8601 Å, c= 5.2315 Å to a = 2.8701 Å, c = 5.2261 Å*) with increase in *ZnO* content (*x*) in the nanocomposite. The extended view of x-ray diffraction pattern of nanocomposites as shown in *Fig. 5.3* reveals shifting of diffraction

peaks with different weight fraction of *ZnO* in $CuFe_2O_4$ nanocomposites. The shifting of diffraction peaks towards lower angle is attributed to larger ionic size of Zn^{2+} as compared to Cu^{2+}.

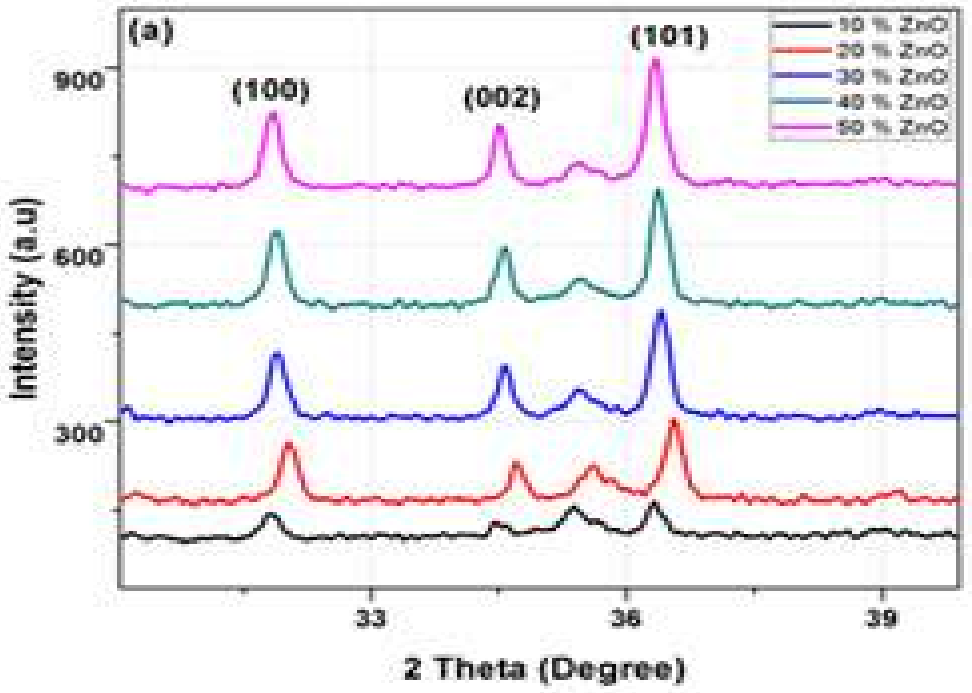

Figure 5.3: Extended view of diffraction pattern of $(ZnO)_x/CuFe_2O_4)_{(1-x)}$ (x=10 to 50 wt. %).

5.2.2 Morphological Study

The morphological study of pristine *ZnO* and its nanocomposites with $CuFe_2O_4$ were examined by *SEM* analysis. *Figure 5.4* demonstrates the *SEM* images that depicts the nanodiscs like morphology of composites with thickness *30 to 70* nm. Also, it is observed that, increase in *ZnO* contents in nanocomposite sample; reduces the agglomeration between the nanodiscs due to nonmagnetic nature of Zn^{2+} ion. However, the shape of nanodiscs were deteriorated in to irregular surface to reduce in surface energy as shown in *Fig.5.4* (e & f).

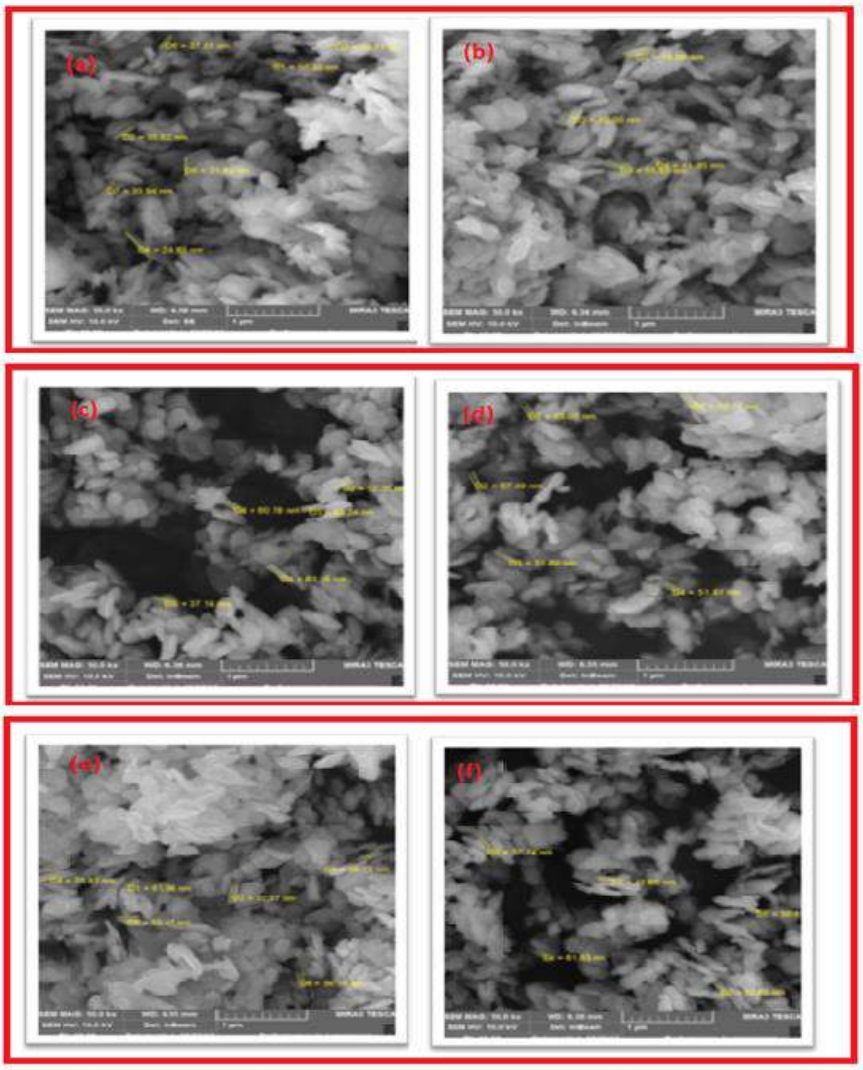

Figure 5.4: SEM images of (a) Pristine ZnO (b) 10% ZnO (c) 20% ZnO (d) 30% ZnO (e) 40% ZnO (f) 50% ZnO.

Moreover, to estimate the grain size of nanocomposites, *TEM* analysis was performed. The *TEM* images of $CuFe_2O_4$ show nearly spherical particles with grain size *30-35* nm, while *ZnO* has nanodiscs like shape with grain size 50 -70 nm. *TEM* images depict that increase in *ZnO* contents in nanocomposite sample, enhance the grain size and alter the morphology from uniform nanodiscs to irregular nanodiscs due to difference in oxygen vacancies and densities of particles that exert stress and strain at the interface.

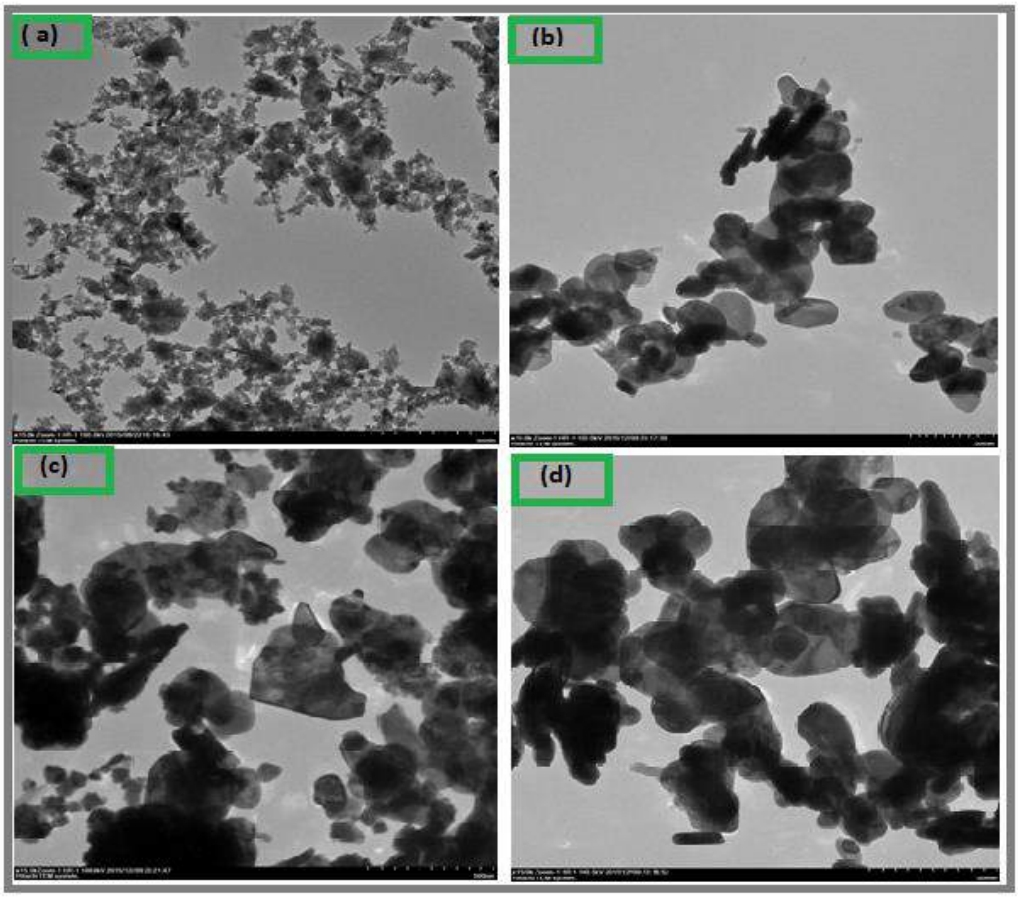

Figure 5.5: TEM images of (a) Pristine $CuFe_2O_4$ (b) Pristine ZnO (c) 20% ZnO and (d) 50% ZnO

5.2.3 Vibrational Analysis

FTIR analyses of prepared samples were measured in the range of 400 to 4500 cm^{-1} as shown in *Fig. 5.6 (a*). The transmittance spectra demonstrate the characteristics stretching vibration peaks (at 414 cm^{-1} and 589 cm^{-1}) of metal ions at octahedral and tetrahedral sites, which is ascribed to pristine $CuFe_2O_4$ [184,185].The distinctive peak of vibration of *Zn-O* was observed at about 493 cm^{-1} and 845 cm^{-1}, which is confirm the materialization of *ZnO* nanodiscs [186]. The absorption bands of O-H, C=O and C-C groups has also been observed at 1100 cm^{-1} and 1500–1600 cm^{-1}. Lastly, the all characteristics peaks of $CuFe_2O_4$ and *ZnO* were also seen in all the composition of $(ZnO)_x/(CuFe_2O_4)_{(1-x)}$ (x=10 to50 wt.%) nanocomposites as shown in *Fig. 5.6 (b).*

Hence FTIR transmittance analysis confirms the formation of nanocomposites and also support the previous *XRD* results.

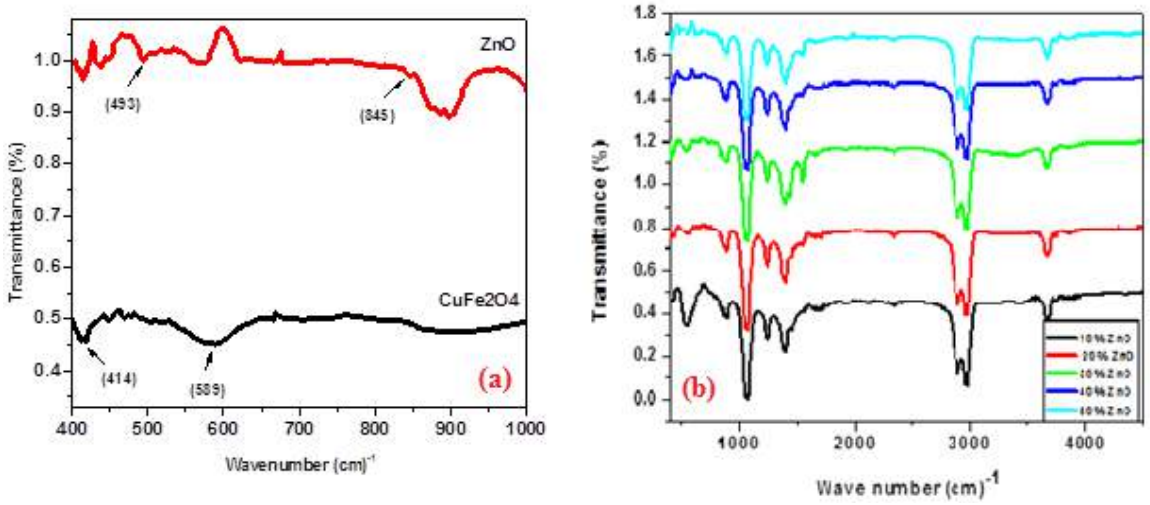

Figure 5.6: FTIR spectra of (a) $CuFe_2O_4$ and ZnO (b) $(ZnO)_x/(CuFe_2O_4)_{(1-x)}$ (x=10 to 50 wt.%).

5.2.4 Magnetic Properties

The *M-H* loop of pure $CuFe_2O_4$ shows, typical behavior of ferrimagnetic which is superparamagnetic in nature as shown in *Fig.5.7 (a)*, while the pristine *ZnO* shows weak ferromagnetic behavior. The magnetic behavior of nanocomposites samples remains same, but the M_s value decreases from 24.10 emu/gm to 13.71emu/gm with incremental increase in *ZnO* contents as calculated in *table-9.1*. This behavior can be elucidated by Sawatzky et. al model [187]. This model considered the interaction in the first neighborhood of Fe^{3+}/Cu^{2+} ions. The exchange integral $J_{1,}$ describe this interaction. According to this model, the hyperfine field at *B* site can be described as:

$$H_f(B) = 2J_1 n S_z(A_1) + 2J_2 (6-n) S_z(A_2) \quad (5.2)$$

Here the existence of two types of ions in the *A* site is considered and *B-B* interaction is ignored. In this system, 1 corresponds to Zn^{2+} ion and 2 correspond to Cu^{2+}/Fe^{3+} ions. The zinc ion (Zn^{2+}) possess zero μ_B, therefore the super exchange interaction [Zn^{2+}(A)-O-Fe^{3+}(B)] becomes zero.

Hence the first term in *Eq.5.5* vanish. On the *B* site, the value of field depends on (Zn^{2+}) ion at *A*-site and at higher contents of zinc oxide, the concentration of non-magnetic (Zn^{2+}) ion increases which replace the magnetic ion (Fe^{3+}/Cu^{2+}) from tetragonal structure and reduces the total magnetic moment of the material. Hence, it is determined that the *ZnO* contents reduce the hyperfine field as can be observed from *Fig. 5.7 (b).*

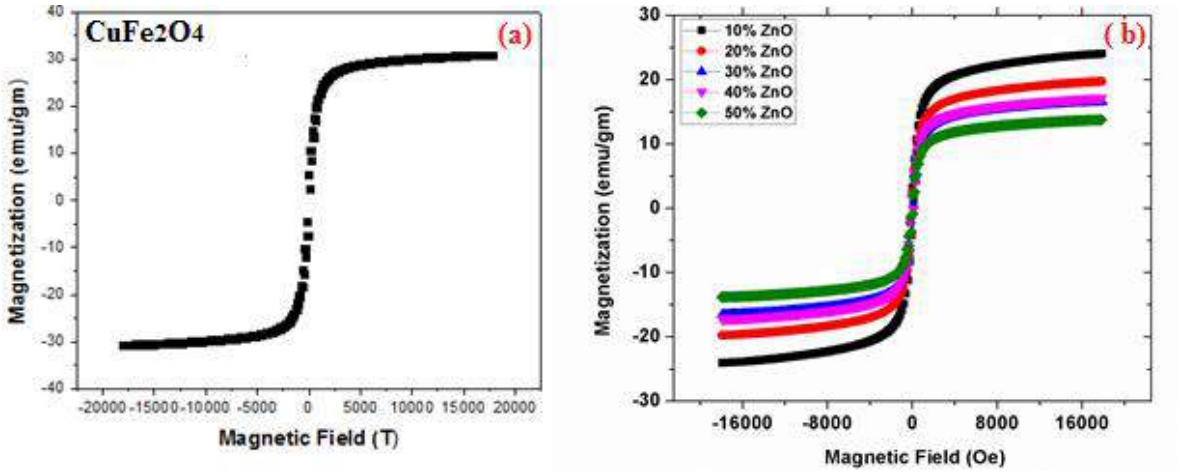

Figure 5.7: M-H loops of (a) Pristine $CuFe_2O_4$ and (b) $(ZnO)_x/(CuFe_2O_4)_{(1-x)}$ nanocomposite.

5.2.5 Microwave Absorption Properties

The Reflection Loss (*RL*) properties of $(ZnO)_x/(CuFe_2O_4)_{(1-x)}$ (x=10-50wt.%) nanocomposites were measured in the frequency range *2-10 GHz*. The *ZnO* possess high value of dielectric loss, while *$CuFe_2O_4$* contains both the dielectric and magnetic loss simultaneously. Therefore, their nanocomposites possess a synergistic behavior and demonstrate the maximum absorption in wide band below *-10 dB* as shown in *Fig. 5.8*. The *EM* wave absorption ability is often specified by *RL* of *EM* waves under normal incidence at the surface of material coated on a conducting surface and is given as [188].

$$RL = 20\, log_{10} \frac{Zin-1}{Zin+1} \quad unit: decibel\ (dB) \tag{5.4}$$

$$Z_{in} = [\ (\frac{\mu_r}{\varepsilon_r})^{\frac{1}{2}}\ tanh\ \{j\left(\frac{2f\pi d}{C}\right)\sqrt{\mu_r \varepsilon_r}\}] \quad (5.5)$$

Where Z_{in}, is impedance of the material, ε_r and μ_r corresponds to complex permittivity and permeability of studied samples respectively. While f is frequency of incident *EM* wave, c is the velocity of light and d is coating thickness of the absorber. According to *EM* absorption theory, high dielectric loss in materials occurs owing to electronic, interfacial polarization and relaxation behavior that results from the collective physical properties of *ZnO/$CuFe_2O_4$* nanocomposites. *Table-9.1*; gives maximum *RL* and frequency bandwidth values at coating thickness of 2 mm. The pristine *$CuFe_2O_4$* shows maximum RL -19.39 *dB*, while small change in *RL* values was observed with further increase in contents of *ZnO* up to 20%. The 30 wt. % *ZnO* contents give excellent *RL* - *42.35 dB* at *4.3 GHz* bandwidth. With further increase in *ZnO* contents $\geq$ 40 % gives the effective absorption (below -*10dB*) over required band width (*2-10 GHz*). This extraordinary *EM* absorption characteristic in these composite samples is attributed to several physical mechanisms involved to increase the dielectric loss in this nanocomposite sample. Firstly, at nanoscale the large number of dipoles are present on the material surface [189,190]. These dipoles produce polarization which contribute in the enrichment of dielectric loss in this composite sample and enhance the *EM* absorption capability. Secondly, the increase in *ZnO* contents in composite samples tune the ferromagnetic resonance frequency and also enhance the eddy current losses, which contribute in enhancement of *EM* absorption [191]. Thirdly, the space charge polarization produced at the interfaces of *$CuFe_2O_4$* and *ZnO*, produce the accumulation of charges with different permittivity zones areas and enhances the dielectric loss accordingly [192,193].

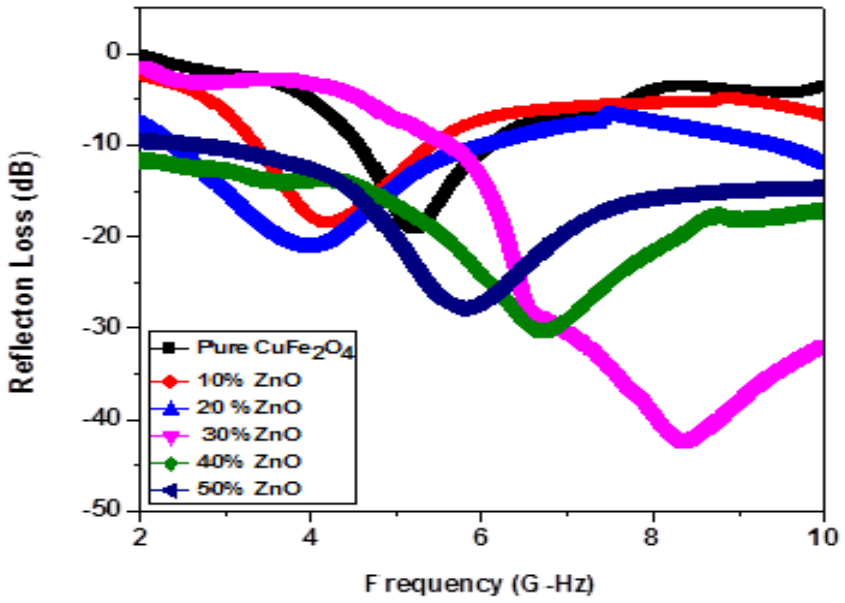

Figure 5.8: RL of $(ZnO)_x/(CuFe_2O_4)_{(1-x)}$ (x=10 to 50 wt.%) with coating thickness 2 mm.

Chapter No. 6

Synthesis and Microwaves Absorption Properties of $CuFe_2O_4$ /MgO Nanocomposites

6.1 Introduction

The *EM* absorption properties of materials depend upon the dielectric loss, magnetic loss, and impedance matching characteristic [194-197]. The ferrites powders are known to be ideal fillers to develop *EM* absorber materials at *MW* frequency because they contain both magnetic and dielectric loss properties simultaneously [198,199].

Since spinel and hexagonal ferrites alone cannot cover strong absorption in wide frequency band width. To overcome this problem, new composites materials like $ZnO/ZnAl_2O_4$, $SrFe_{12}O_{19}/ZnO$, $SrFe_{12}O_{19}/\alpha Fe_2O_3$, Fe_3O_4/ZnO, $ZnO/CoFe_2O_4$, Fe_3O_4/SnO_2 were prepared by different synthesis techniques [200-208].

Among different *MOs* ceramic nanostructures, *MgO* is a wide band gap insulating material with bandgap energy 5-6 eV. Different morphologies of *MgO* ceramic are extensively used for several purposes like antibacterial agent, high-T_c superconducting material and for suppression of electromagnetic Interference (*EMI*) [200,201]. In this chapter the effect of *MgO* contents on *MW* absorption properties of $CuFe_2O_4$ composites has been studied extensively. The *RL* properties shows increase in absorption of *MW* with *MgO* contents.

6.2 Results and Discussion

6.2.1 Structural Study

The structural investigation was carried out by *XRD* measurement, on all prepared samples. The characteristic peaks of *MgO* in composite samples were observed at: 37º (111), 42º (200), 62º (220), 74º (311) and 78º (222) [202].

The qualitative analysis shown in *Fig. 6.1* reveals that the intensities of diffraction peaks of $CuFe_2O_4$ (at 35.5440º) reduces, while the intensity of main peak of *MgO* (at 42º) increases with proliferation in weight fraction of *MgO*. This increase in intensity is attributed to the occurrence of large diffraction planes for *MgO*.

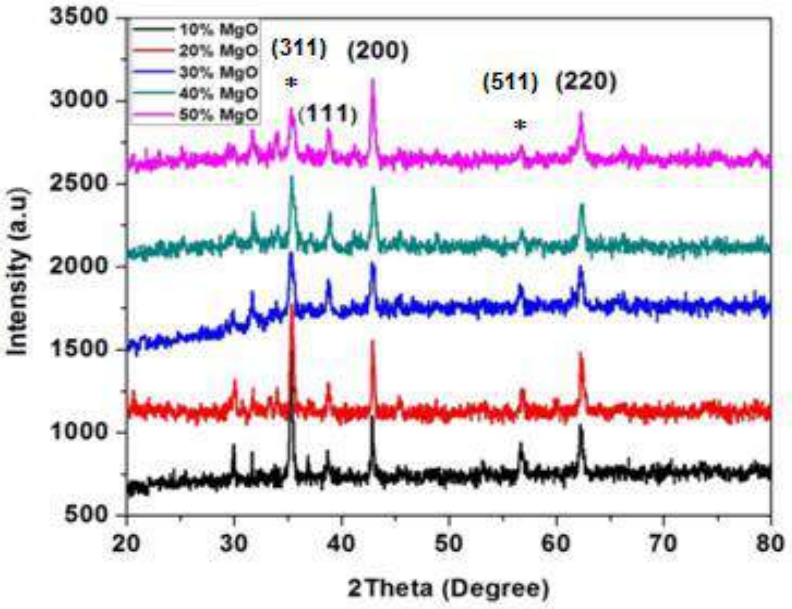

Figure 6.1: XRD pattern of $(MgO)_x/(CuFe_2O_4)_{(1-x)}$ (x= 10 to 50 wt. %) nanocomposite.

6.2.2 Morphological Study

The morphology of nanostructures has great influence on *RL* properties as well [203]. Therefore, to control the grain size and morphology of nanocomposites is great challenge for material scientists. In this study, the synthesis of nanocomposites with different weight fractions of *MgO* were prepared for excellent *EM* absorption properties. The *TEM* images shown in *Fig.6.2* (*a and b*) reveal the morphology of pristine $CuFe_2O_4$ and *MgO* respectively. The *TEM* micrographs depict that the grains are spherical in nature with average size 20-30 nm. *Fig.6.2* (c and d) demonstrate the morphology of composites with x = 20 and 50 wt. %. These micrographs demonstrate that increase in *MgO* content deteriorate the morphology from spherical to an irregular

shape due to increase in oxygen vacancies that enhance the diffusion rate of substituted ions from lattice site [209].

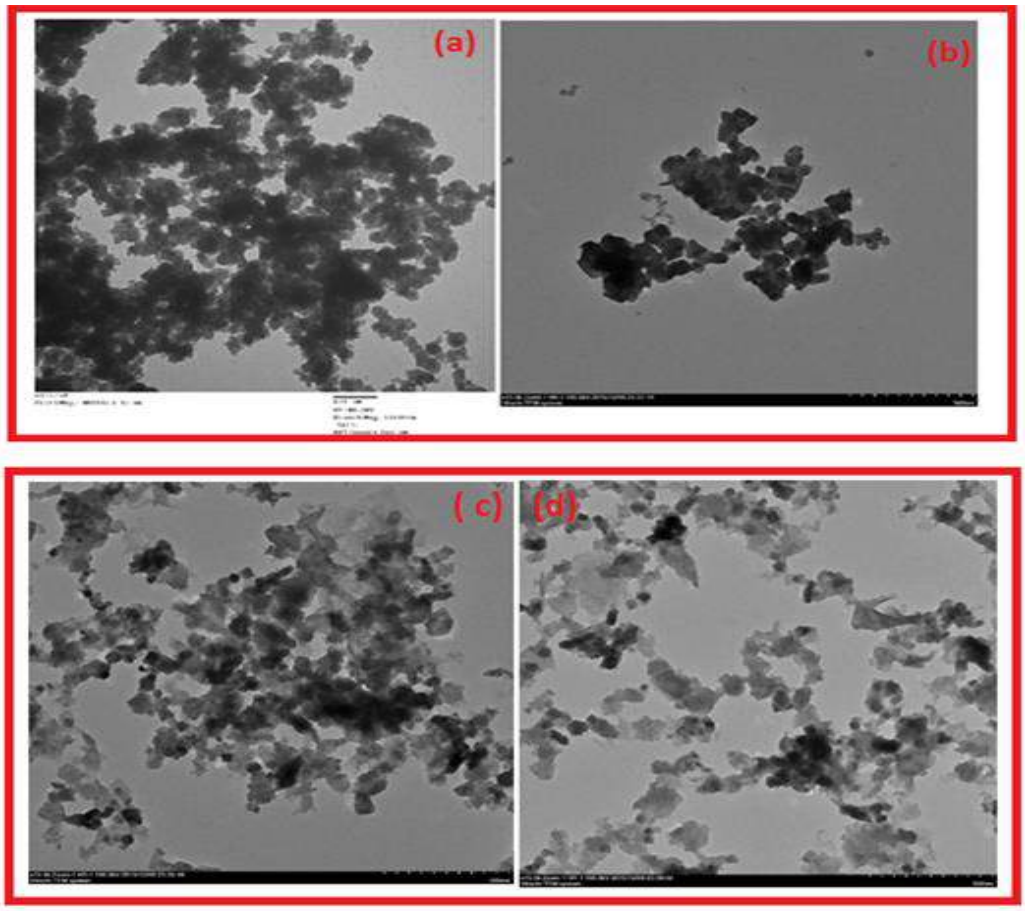

Figure 6.2: TEM images of (a) Pristine $CuFe_2O_4$ (b) Pristine MgO(c) 20% MgO and (d) 50% MgO.

6.2.3 Vibrational Analysis

Figure 6.3(a) shows the characteristics absorption modes of ferrites at 589 cm^{-1} and 404 cm^{-1}, and peaks at 883 cm^{-1} and 618 cm^{-1} in *MgO* spectra were also observed which is ascribed to different Mg-O vibration modes [204,205]. Also, the bending mode of absorption of water molecule at 1630-1640 cm^{-1} were also observed. The broad band between 3000-4000 cm^{-1} confirms the stretching mode of O-H group [204]. Hence, the *FTIR* study supports the formation of $(MgO)_x/(CuFe_2O_4)_{(1-x)}$ nanocomposite.

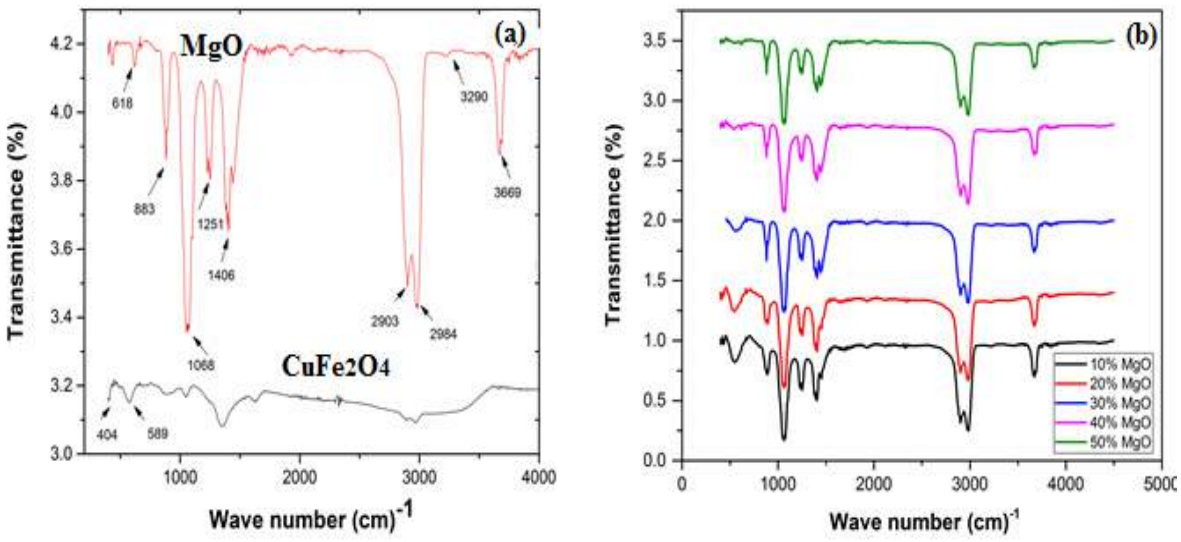

Figure 6.3: FTIR spectra of (a) $CuFe_2O_4$ and MgO (b) $(MgO)_x/(CuFe_2O_4)_{(1-x)}$ (x=10 -50 wt. %) nanocomposites.

6.2.4 Magnetic Properties

Figure 6.4 (a and b), shows the *MH* loops of pristine $CuFe_2O_4$ and composite samples with different weight fractions of *MgO* (x=10 to 50 wt.%) under applied field of $\pm$ 2*T*. All samples show the same superparamagnetic behavior with decrease in M_s value with the addition of nonmagnetic *MgO* contents as already reported in literature [206-208]. The inset in *Fig.6.4 (b)* shows *RTFM* behavior of pristine *MgO* at low field range $\pm$ 0.5T with M_S value of 0.02 emu/gm. This *RTFM* in *MgO* nanoparticles was mostly ascribed to the surface defects and oxygen vacancies induced at nanoscale [209-211].

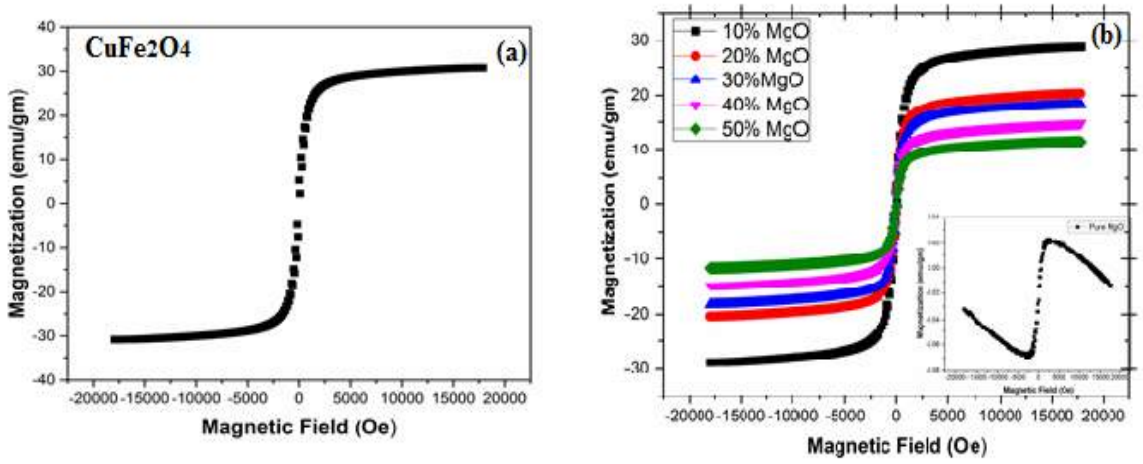

Figure 6.4: M-H loops of (a) Pristine $CuFe_2O_4$ (b) $(MgO)_x/(CuFe_2O_4)_{(1-x)}$ (x=10 to 50 wt.%) nanocomposite.

6.2.5 Microwave Absorption Properties

The *MW* absorption characteristics of material depend upon dielectric loss, magnetic loss, anisotropic energy and accumulation of dipoles in different grains [212-214]. Figure.6.5 shows the *RL* from 2-10 *GHz* and it is obviously observed that there is no broad peak below -10 *dB* up to 30 wt. % of *MgO* fractions in composite sample. However, further additions of *MgO* contents significantly enhance the *MW* absorbing abilities and widen the absorption band. The *MgO* $\geq$40 wt. % of contents in composite sample shift the absorption curve to higher frequency due to change in resonant frequency. This strong *MW* absorption is ascribed to several relaxation processes such as: dipolar reorientation processes, electronic and relaxation effects etc. [215].

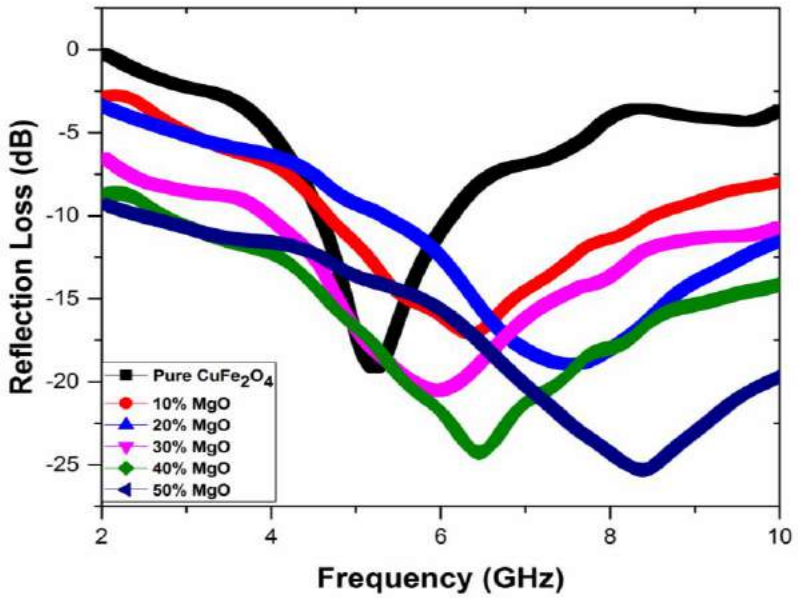

Figure 6.5: RL of $(MgO)_x/(CuFe_2O_4)_{(1-x)}$ (x=10 to 50 wt.%) with coating thickness of 2 mm.

The increase in absorption strength with change in *MgO* contents is attributed to increase in anisotropic energy. Figure 6.4 (b) shows that increase in *MgO* contents in composite samples decrease the M_s value. This decrease in M_s value enhance the anisotropic energy which is beneficial for absorption of *MW* in composite sample. Moreover, this composite sample contains large number of defects which behave as a scattering center for *MW* and after multiple internal scattering the wave is fully absorbed within material. Finally, in this composite materials the interfaces having different permittivity zones increases. To reduce the energy, the charges accumulate at these interface and produce space charge polarization [216]. This polarization increases the dielectric loss which leads to enhancement in *MW* absorption.

Chapter No.7

Synthesis and Microwave Absorption Properties of WO_3/$CuFe_2O_4$ Nanocomposites

7.1 Introduction

The absorption frequency of nanocomposite materials can be tuned by controlling the coating thickness, morphology, particle distribution in matrix and loading percentage of dielectric and magnetic loss materials [217]. Since *MOs* nanostructures demonstrated high dielectric loss, thermal stability, cost-effectiveness and high corrosion resistance. These engrossing properties made them promising for the development of high frequency absorbing coating [218].

WO_3 is an important transition *MO*, having direct band gap and *n*-type conductivity. WO_3 nanostructures have been widely studied for various scientific and industrial applications due to their tremendous physical and chemical characteristics [219]. In this chapter the tuning in absorption frequency can be achieved by increasing the weight fraction of WO_3 in composite sample of $CuFe_2O_4$. The elevation of WO_3 weight fractions in composite samples lead the *MW* absorption towards higher frequency. This tuning in absorption properties makes this material a potential candidate for *EMI* suppression at required frequency.

7.2 Results and Discussions

7.2.1 Structural Study

The structural analysis shows in *Fig. 7.1 (a)* depicts the inverse spinel tetragonal crystal structure of $CuFe_2O_4$ without any other impurity phase [220], whereas in *Fig. 7.2 (b)*, the characteristic peaks of monoclinic crystal structure of WO_3 were also observed [221].

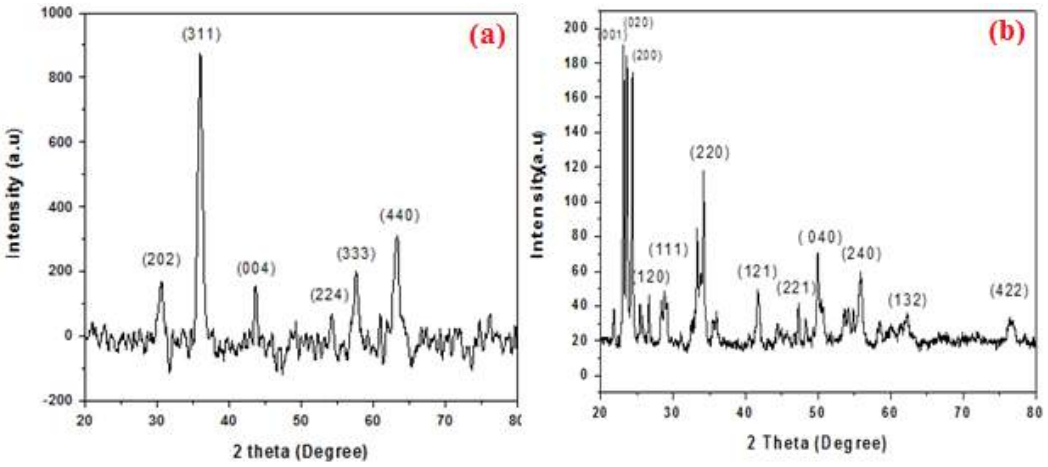

Figure 7.1: XRD patterns of (a) Pristine $CuFe_2O_4$ and (b) Pristine WO_3.

The *XRD* pattern shown in *Fig.7.1 (c)* confirms the formation of nanocomposites $(WO_3)_x/(CuFe_2O_4)_{(1-x)}$ (x=10 to 50 wt.%). The diffraction pattern of composite sample demonstrates that the peaks at 30º (202) and 35.54º (311) are characteristic peaks of $CuFe_2O_4$ and their intensities decrease with increase in weight fraction of WO_3. Whereas the intensities of diffraction peaks for WO_3 at 23.50º (020), 26.69º (120) and 28.68º (111) raise due to the presence of larger diffracting planes.

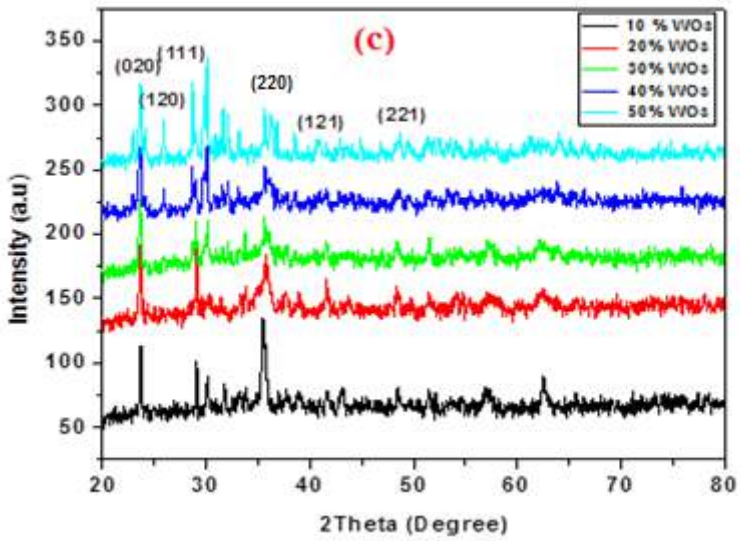

Figure 7.1: (c) XRD pattern of $(WO_3)_x$ /$(CuFe_2O_4)_{(1-x)}$ (x=10 to 50 wt. %).

7.2.2 Morphological Analysis

The morphology of nanostructures also influences the magnetic, dielectric and *EM* absorption characteristics of the materials [222]. Therefore, the morphology (shape and grain size) of prepared pristine samples and their nanocomposites were analyzed through *TEM*. The *TEM* images demonstrated that the morphology of WO_3 particles is nano-plate like with size ranges from 20 to 30 nm as presented in *Fig. 7.2 (b).* These micrographs also demonstrated that higher weight fractions of WO_3 enhance the oxygen vacancies and agglomerate the particles to reduce the surface energy as observed in *Fig. 7.2 (c and d).* Moreover, the addition of WO_3 weight fractions in composite also deteriorate the surface of WO_3 grains to an irregular structure.

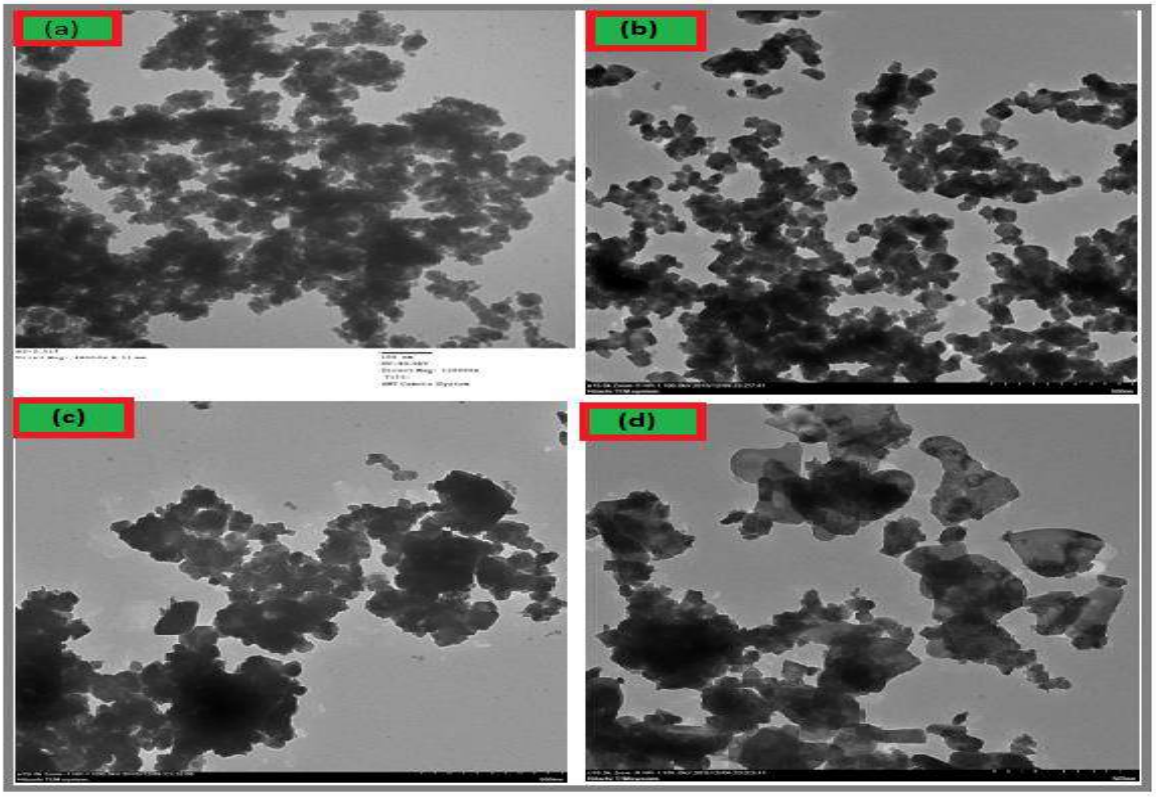

Figure 7.2: TEM images of (a) Pristine $CuFe_2O_4$, (b) Pristine WO_3, (c) 20 % and (d) 50 % WO_3.

7.2.3 Vibrational Analysis

FTIR transmission spectroscopy was performed to study the characteristic stretching vibration modes. The *FTIR* transmittance spectra of pristine nanostructures of $CuFe_2O_4$, WO_3 and their nanocomposites were measured in the range of 400 to 4000 cm^{-1}. In *Fig. 7.3 (a)* the stretching modes at 589 cm^{-1} and 404 cm^{-1} depict the cation vibrations at tetrahedral and octahedral sites of ferrite, whereas, the vibration modes at 1044 cm^{-1} and 1240 cm^{-1} may be due to stretching mode of W-O and O-W-O respectively. The band at 948 cm^{-1} may be due to W=O vibrations and the band at 647 cm^{-1} represents the W-O-W stretching mode [223-225]. Figure.*7.3 (b)* shows the transmittance spectra of composites samples in which the characteristics vibration modes of WO_3 and $CuFe_2O_4$ were observed without any other impurity phases. Hence, these *FTIR* results have also confirmed the formation of nanocomposites and corroborate well with XRD results.

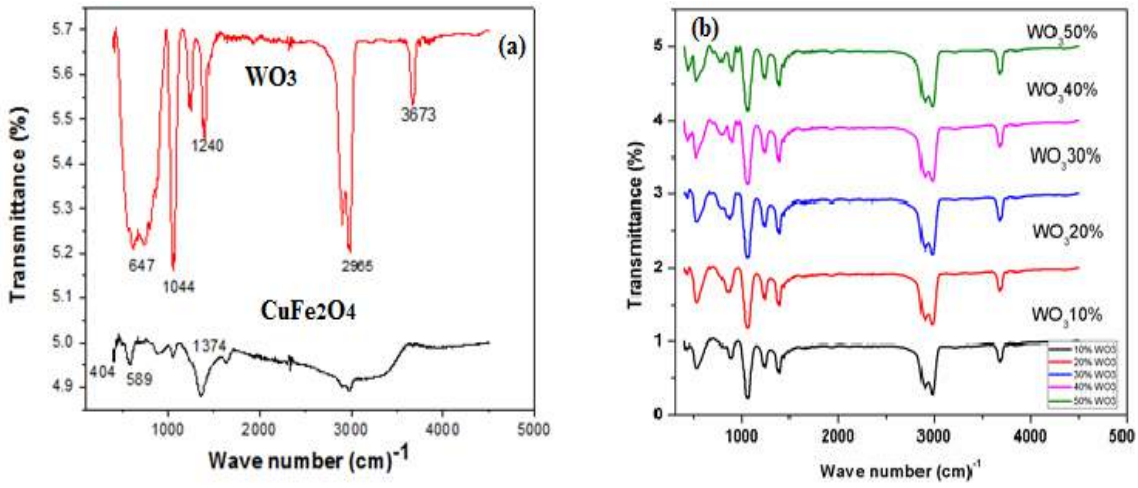

Figure-7.3: FTIR spectra of (a) pristine $CuFe_2O_4$ and WO_3 (b) $(WO_3)_x/(CuFe_2O_4)_{(1-x)}$ (x=10 to 50 wt. %) nanocomposites.

7.2.4 Magnetic Properties

The hysteresis loop of pristine $CuFe_2O_4$ shows a superparamagnetic behavior, while hysteresis loop of pristine WO_3 demonstrates weak ferromagnetic behavior at nanoscale as already shown in *Fig. 4.2.* This ferromagnetic behavior is ascribed to the existence of surface defects especially oxygen vacancies, as reported in different *MOs* nanostructures [226-231].

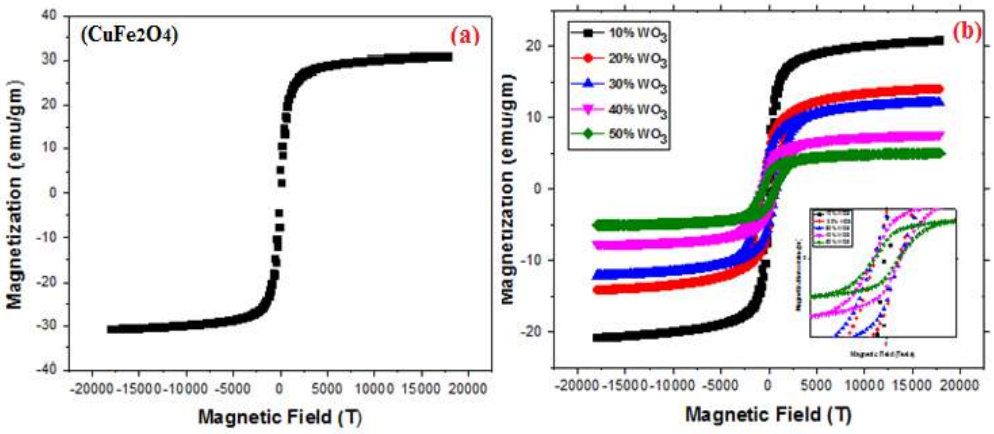

Figure-7.4**:** M-H loops of (a) Pristine $CuFe_2O_4$ and (b) $(WO_3)_x/(CuFe_2O_4)_{(1-x)}$ **(**x= 10-50 wt.%) nanocomposites.

Figure 7.4 (b), shows the *M-H* loops of nanocomposites with different weight fractions of WO_3. The M_s value of $(WO_3)_x/(CuFe_2O_4)_{(1-x)}$ (x=10 to 50%) nanocomposites decreases slowly while the H_c increases with incremental enhancement of nonmagnetic contents of WO_3. This decrease in M_s value can be understood by following relation.

$$M_S = \Phi m_s \qquad 7.1$$

Where Φ is weight fractions of magnetic constituents and m_s is the saturation magnetization of single magnetic particle. Moreover, the value of H_c of composite depends upon grain size, morphology and anisotropic energy. The increase in weight fractions of WO_3 in composite change the shape and particle size as revealed by *TEM* images. This change in morphology also enhance

the grain size in which particles having different orientation of grains agglomerated that leads to the high value of anisotropic energy and H_c as depicted in the inset of *Fig. 7.4 (b).*

7.2.5 Microwave Absorption Properties

The *MW* absorption properties of composite material depend upon the, permittivity and permeability, morphology and crystal structure, shape and domain size etc [232]. As $CuFe_2O_4$ is a magnetic loss material with a negligible value of dielectric loss and shows higher value of *RL* in GHz frequency. The absorbing performance of $CuFe_2O_4$ was enhanced by incorporation of WO_3 as a dielectric loss filler. The WO_3 in composite sample enhance the interfaces with different permittivity zone and also dissipate the energy by different polarization mechanisms and relaxation effects [233,234]. The *MW* absorption capability of a material originates from two main factors 1) impedance matching and 2) *EM* attenuation [235,236]. Firstly, at certain concentration of WO_3 the magnetic and dielectric loss may be higher which cause higher *EM* attenuation. As WO_3 nanostructures have higher dielectric loss as compared to $CuFe_2O_4$ nanoparticles the later have better magnetic loss properties. Therefore, at a specific weight percent of WO_3 and $CuFe_2O_4$ *MNPs* produce balanced dielectric and magnetic losses which lead to higher *EM* absorption [237-239]. *Figure-7.5* shows the *RL* of the WO_3-$CuFe_2O_4$ nanocomposites with varying WO_3 weight fractions measured in the frequency range of 2-10 *GHz.* The *RL* of $CuFe_2O_4$ reaches -19.39 *dB* at 5.21 *GHz* and the addition of WO_3 contents (30 wt.%) leads to the enhancement in *MW* absorption that corresponds to decrease in *RL* and reaches to -26.32 *dB* at frequency of 6.6 *GHz* for 30 wt. % of WO_3 as listed in *table 9.1.* Further increase in WO_3 content enhance the *RL* of composites and also produces a shift in absorption peaks towards higher frequencies. This tuning of absorption peaks toward higher frequency is attributed to change in ferromagnetic resonance frequency.

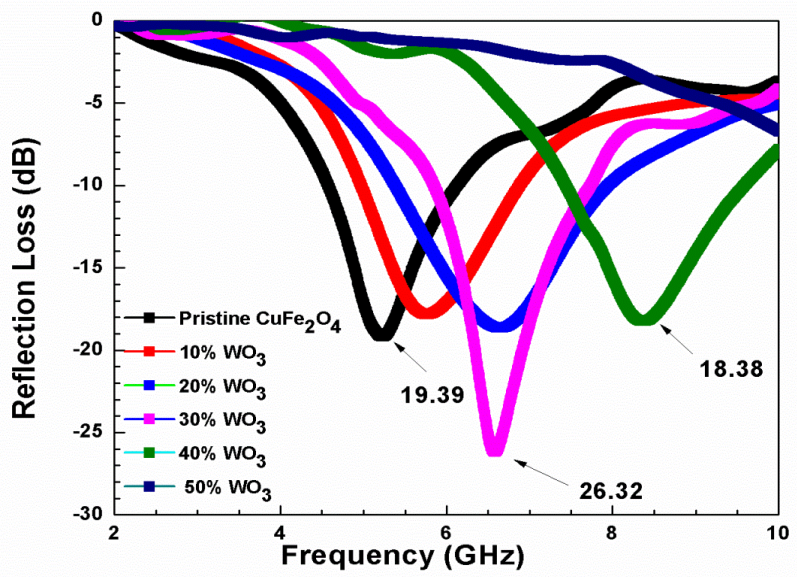

Figure 7.5: RL of $(WO_3)_x/(CuFe_2O_4)_{(1-x)}$ (x=10 to 50 wt.%) at thickness of 2 mm.

Moreover, the higher weight fractions of WO_3 (40 and 50 wt.%) reduces the absorption of *MW* due to change in the permittivity and permeability that disturb the impedance matching condition and hence enhance the reflection of waves from the surface of composite.

Chapter No. 8

Synthesis and Microwave Absorption Properties of SnO_2 -$CuFe_2O_4$ Nanocomposites

8.1 Introduction

Advance nanomaterials and their composites have gained enormous attention due to their unique physiochemical properties. Their nanosize effect and tailor made properties play a dynamic role for technological application. Among different types of composites, ferrites based *MOs* nanocomposites have attracted numerous considerations since last few decades [240-243]. Nanocomposites of $CuFe_2O_4$ with other *MOs* (*M= Ce, Si, and Ti*) have been prepared by different synthesis techniques to obtain the desired characteristics for required application [244,245]. SnO_2 is an n-type semiconductor (3.8 eV) with rutile tetragonal structure and its nanocomposites with $CuFe_2O_4$ reveal interesting physiochemical characteristics and making it potential candidate for numerous technological applications [246,247].

In this chapter the effect of SnO_2 wt. fractions in composite samples of $CuFe_2O_4$ has been studied in detail. The *MW* absorption properties show decrease in *RL* from -19.39 to -28.37 at 20 wt.% of SnO_2. This increase in strength of absorption is attributed to different types of polarizations, which are produced in composites sample. The dipolar and electronic polarization play a dominant role in this composition and enhance the absorption capability. Further increase in SnO_2 contents deteriorate the impedance matching conditions and hence reduce the absorption in effective frequency bandwidth.

8.2 Results and Discussions

8.2.1 Structural study

The structural analysis of pristine $CuFe_2O_4$ and SnO_2 has been studied through powder x-ray diffraction (*XRD*) technique. *Figure.8.1 (a and b)* shows the XRD patterns of $CuFe_2O_4$ and SnO_2 having simple tetragonal and rutile type tetragonal structures respectively [248,249]. The broadening in diffraction peaks reveals the nanocrystalline nature of prepared samples and average grain size lies in the range of 17- 31 nm.

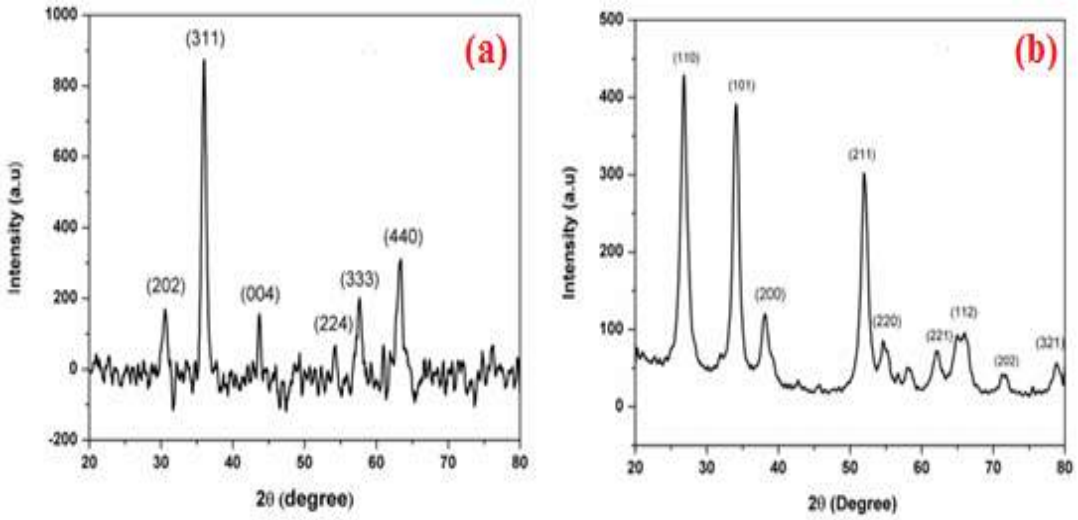

Figure 8.1: XRD patterns of (a) Pristine $CuFe_2O_4$ and (b) Pristine SnO_2.

Figure 8.1 (c) demonstrates the *XRD* pattern of $(SnO_2)_x/(CuFe_2O_4)_{(1-x)}$ (x=10 to 50 wt.%) composite. The composites (x=10 to 30 wt.%) reveal single phase of tetragonal structure of $CuFe_2O_4$ due to thermodynamic solubility of SnO_2 in the complex structure (inverse spinel) of $CuFe_2O_4$. The further addition in weight fractions of $SnO_2 \geq 40\%$ in composite, a secondary phase of SnO_2 was observed which revealed that SnO_2 is not fully dissolved in $CuFe_2O_4$ lattice. A slight variation in lattice parameters were also observed due to difference in ionic radii of Cu^{2+} and Sn^{4+} that produce stress and strains at the interface of both phases and hence distort the crystal lattice.

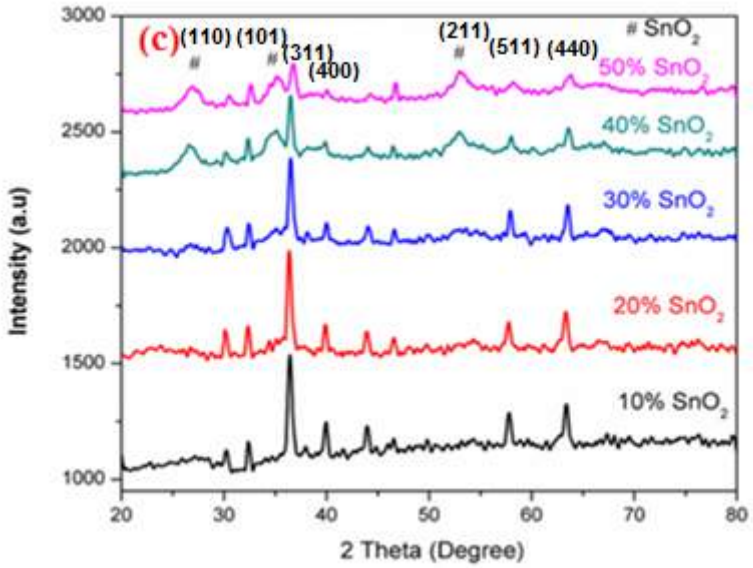

Figure 8.1 (c) XRD patterns of $(SnO_2)_x/(CuFe_2O_4)_{(1-x)}$ (x=10 to 50 wt.%) nanocomposite.

8.2.2 Morphological Study

The *TEM* analysis was performed to observe the grain size and morphology of the composite. The *TEM* images in *Fig. 8.2* demonstrate the nano-scaled of grain size with spherical morphology. The SnO_2 sample reveals spherical morphology having average grain size in the range of 30 nm. The SnO_2 contents in composite has influenced both the grain size and morphology. The morphology of composite samples is slowly transformed into flatter plate like particles and increase in grain growth is also observed which is ascribed to increase in oxygen vacancies as shown in *Fig. 8.2 (b and c).*

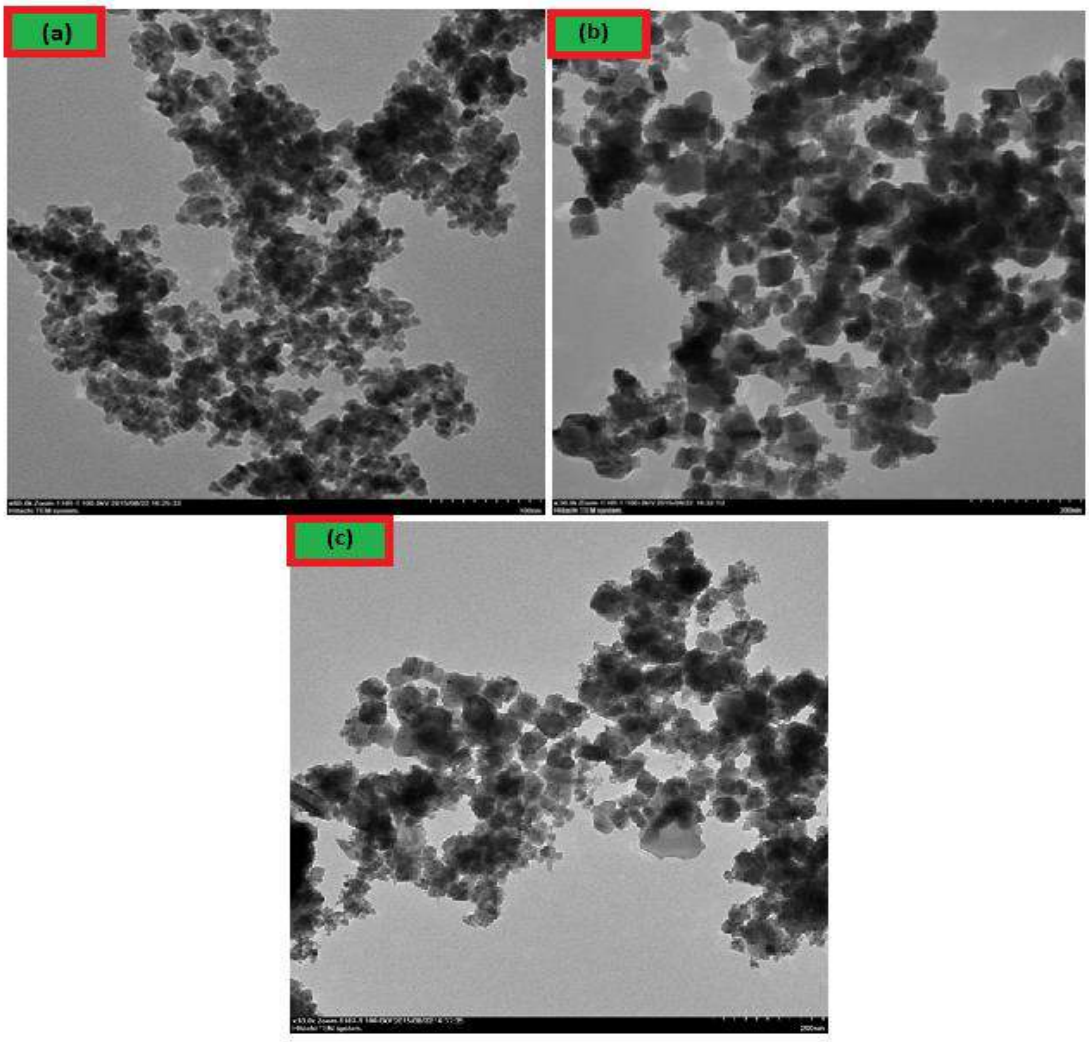

Figure 8.2: TEM micrographs of (a) Pristine SnO_2, (b) 20% SnO_2, and (c) 50% SnO_2 loaded $CuFe_2O_4$ nanocomposites.

8.2.3 Vibrational Analysis

The *FTIR* spectroscopy was carried out to further validate these results and to study the vibrational properties of synthesized samples. *Figure 8.3* shows the *FTIR* transmittance spectra of $(SnO_2)_x/(CuFe_2O_4)_{(1-x)}$ composites. In *FTIR* spectra, the characteristics vibration modes of metal ions at octahedral (band at 410 cm^{-1}) and tetrahedral sites (band at 586 cm^{-1}) were observed. The bands at octahedral and tetrahedral show different intensities which is attributed to difference in bond lengths of Fe-O at lattice sites [250]. At lower concentration of SnO_2, there is slight shift

towards lower wave number is observed which is attributed to migration of Fe^{3+} ions from lattice sites. Moreover, the vibration modes of SnO_2 (Sn-O and Sn-O-Sn) were also observed at higher concentration of SnO_2 in composite which validate previous *XRD* results [251]. The absorption peak at 1061 cm^{-1} may be associated to the Sn-Cu band vibration [252]. Thus the *FTIR* study clearly shows the formation of desired $(SnO_2)_x/(CuFe_2O_4)_{(1-x)}$ nanocomposites.

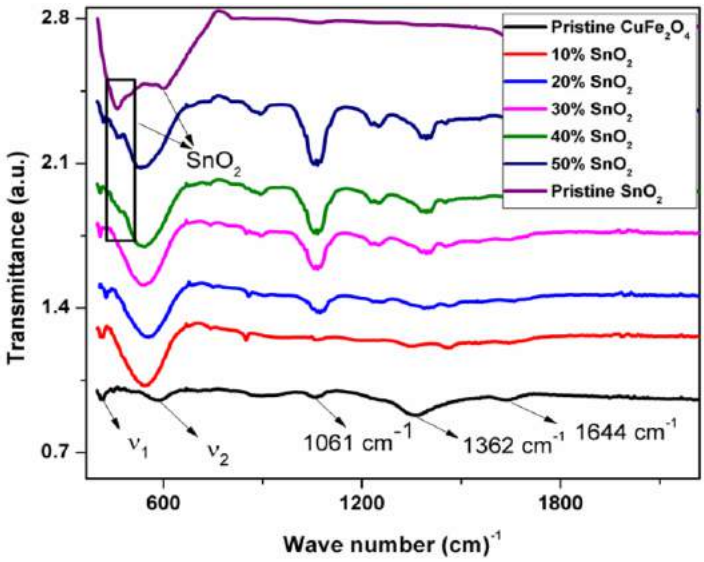

Figure 8.3: FTIR Spectra of the prepared $(SnO_2)_x/(CuFe_2O_4)_{(1-x)}$ nanocomposites.

8.2.4 Magnetic Properties

The magnetic properties in *Fig. 8.4 (a and b)* demonstrates the superparamagnetic behavior of $CuFe_2O_4$ having M_s =30.78 emu/gm and zero value of coercivity. The SnO_2 is diamagnetic in bulk form, but shows a weak ferromagnetic behavior at nanoscale originated due to oxygen vacancies and surface defects already discussed in chapter 4.

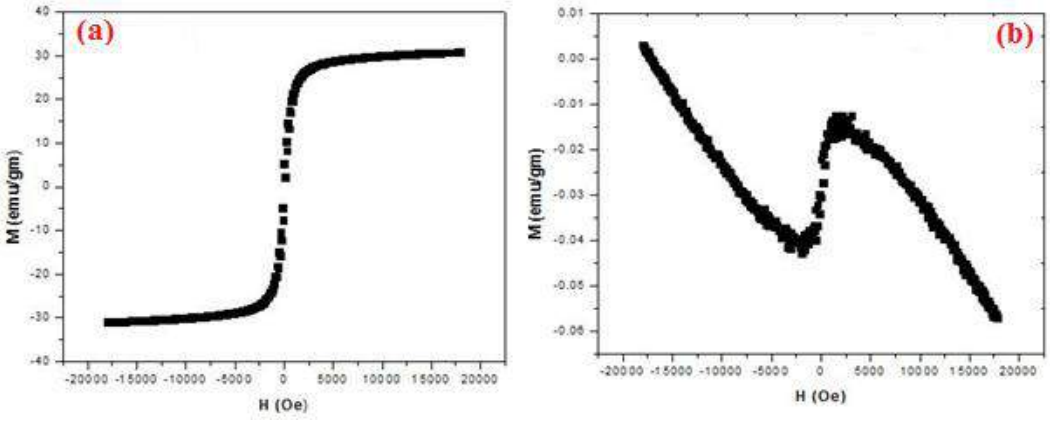

Figure 8.4: M-H loops of (a) Pristine $CuFe_2O_4$ and (b) Pristine SnO_2

Figure 8.4 (c) shows that the magnetic properties of the composites changed significantly with the increase in SnO_2 weight fractions. All the sample show same ferromagnetic behavior but M_s values decreases systematically with SnO_2 contents. As $CuFe_2O_4$, has inverse spinel structure in which $8Cu^{2+}$ ions reside in octahedral sites (*B*) while $16Fe^{3+}$ ions reside in both octahedral (*B*) and tetrahedral sites (*A*) [253]. When non-magnetic Sn^{4+} ions with zero magnetic moment are incorporated in composites, it reduces the overall moment of composites and hence decrease the *Ms* values.

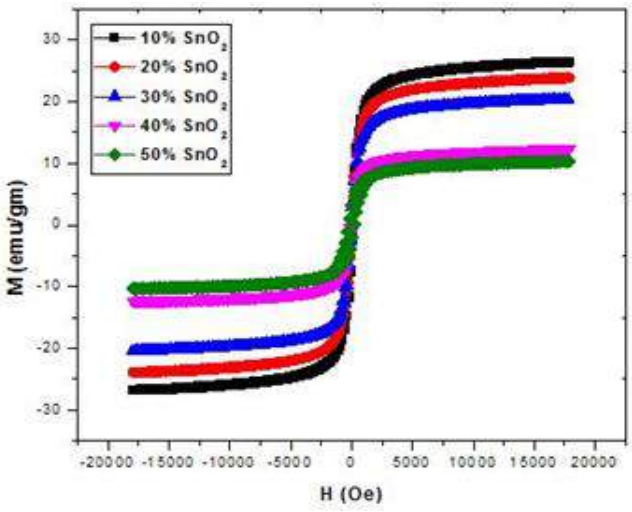

Figure 8.4 (c) M-H loops of $(SnO_2)_x/(CuFe_2O_4)_{(1-x)}$ (x=10 to 50 wt.%) nanocomposite.

8.2.5 Microwave Absorption Properties

The high frequency *MW* absorption properties of $(SnO_2)_x/(CuFe_2O_4)_{(1-x)}$ *(x=10 to 50 wt. %)* nanocomposites has also measured in the frequency range *2-10 GHz*. The addition of SnO_2 weight fractions in composite samples shift the absorption peaks towards higher frequency. *Figure 8.5* shows that, in pristine $CuFe_2O_4$, the maximum *RL* is only -19.39 *dB* and the effective bandwidth is only 1.23 *GHz*. The effective absorption bandwidth with minimum *RL* (-22.37 *dB* to -28.37 *dB*) was observed with 10 and 20 wt. % loading of SnO_2 respectively in composite sample. As reported in literature, the excellent *MW* absorption characteristics of materials mainly depend on the proper matching condition of dielectric loss and magnetic loss [235,236]. The SnO_2 is an important dielectric material in which dipolar polarization is dominated and the associated relaxation phenomena in an alternating field constitute the loss mechanisms [189]. The addition of SnO_2 loadings (*10 to 20 wt. %*) in $CuFe_2O_4$ *MNPS* generate a balanced matching condition and consequently enhance the *MW* absorption ability.

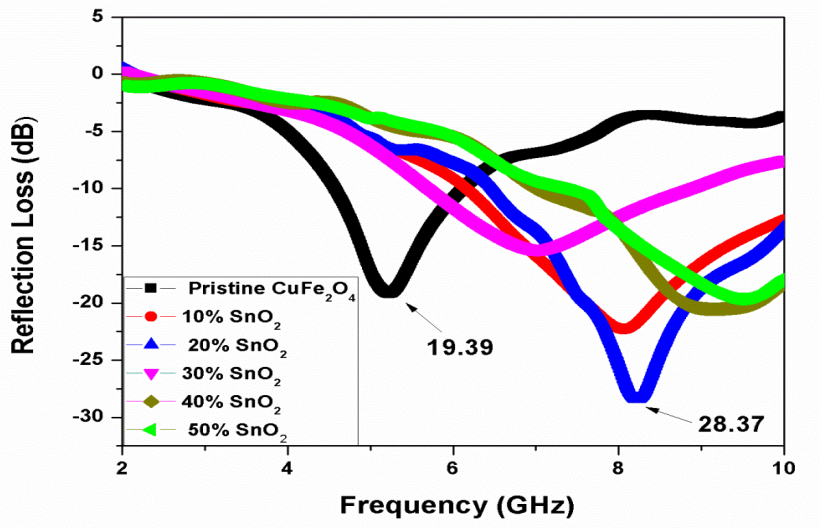

Figure 8.5: RL of $(SnO_2)_x/(CuFe_2O_4)_{(1-x)}$ *(x=10 to 50 wt.%)* nanocomposites at thickness of 2mm.

The higher loading fractions of SnO_2 (*30-50 wt. %*) in composite sample enhance the dielectric loss, but reduce the magnetic losses produced by eddy current effect, natural resonance and exchange resonance phenomena [212]. Therefore, this higher concentration of SnO_2 (*30-50 wt. %*) disturbed the synergistic effect of dielectric and magnetic losses in composite sample and deteriorate the impedance matching condition.

Chapter No. 9

Structural, Magnetic and Microwave Absorption Properties of $CuFe_2O_4$/NiO Nanocomposites

9.1 Introduction

The *EM* characteristics of nanocomposites abruptly differ from those of their single crystalline, polycrystalline and bulk counterparts. The large surface area, higher contribution from the interfacial region, the probability of high defect density and tailoring in band structure influence the properties of these fascinating materials. Being an important member of transition *MOs* family, *NiO* contains several applications in different sensors, fuel cell electrodes and dielectric loss fillers in polymer matrix [254-261]. In this chapter the magnetic and *MW* absorption properties of prepared nanocomposites $(NiO)_x/(CuFe_2O_4)_{(1-x)}$ (x=10 to 50 wt.%) have been investigated in detail.

9.2 Results and Discussion

9.2.1 Structural Study

Figure 9.1 (a and b) shows the *XRD* pattern of pristine $CuFe_2O_4$ and *NiO*, which revealed the tetragonal and face centered (*FCC*) cubic crystal structures of $CuFe_2O_4$ and *NiO* respectively. The *XRD* pattern of the $CuFe_2O_4$ composite samples with different weight fractions of *NiO* is shown in *Fig. 9.1(c).* The increase in weight fractions of *NiO* in composite sample enhance the intensity of diffraction peaks assigned *to NiO* phase. In *Fig. 9.1 (c),* the diffraction peaks related to $CuFe_2O_4$ phase are marked with an asterisk while the *NiO* peaks are marked with arrow head.

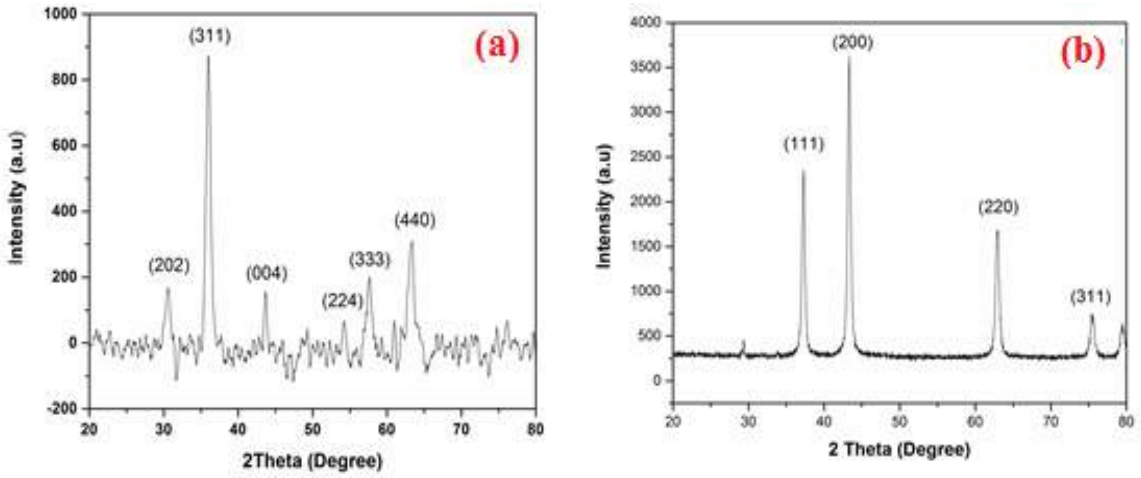

Figure 9.1: XRD patterns of (a) Pristine $CuFe_2O_4$ and (b) Pristine NiO

The *Fig.9.1* (c) revealed that, the intensity of the diffraction peaks of *NiO* increases with a surge in *NiO* weight fractions. Moreover, the broadening in diffraction peaks validates the nanometer dimensions of crystallites with size in the range of 22-36 nm for all compositions.

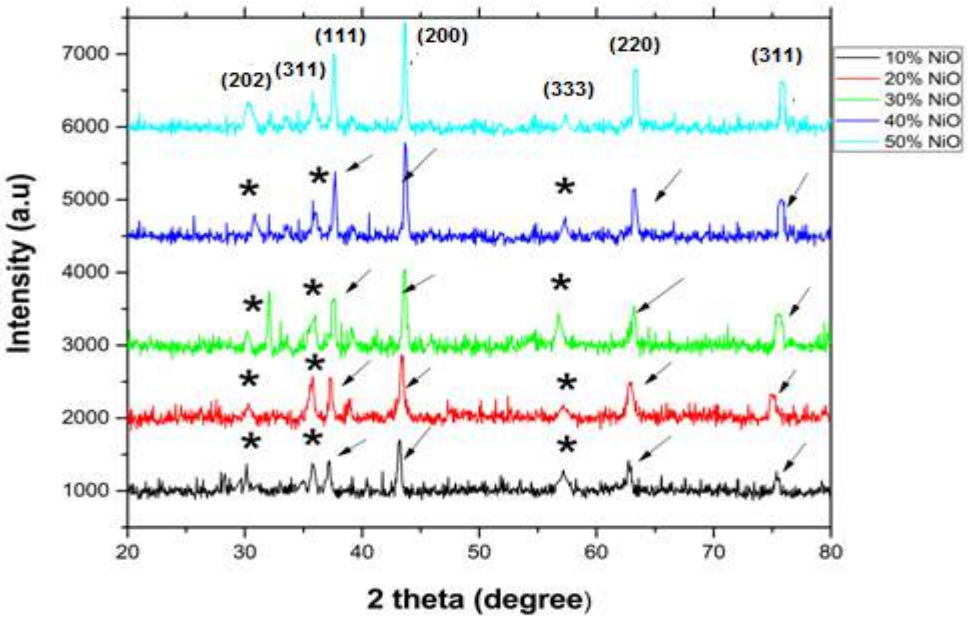

Figure 9.1(c): XRD patterns of $(NiO)_x/(CuFe_2O_4)_{(1-x)}$ (x=10 to 50 wt. %) nanocomposites.

Figure 9.2 demonstrates the extended view of diffraction pattern of the composite of $CuFe_2O_4$ having a different weight fraction of *NiO*. The addition of *NiO* produces a slight shift in diffraction

peaks towards higher *2θ*. This shifting is attributed to the substitution of Cu^{2+} (87 pm) ions by Ni^{2+} (83 pm) ions. The smaller ionic radii of Ni^{2+} ions as compared to Cu^{2+} ions decrease the lattice constant of cubic structure. As a result of which the spacing between lattices planes decreases, that produces a shifting of peaks towards higher *2θ* as shown in *Fig. 9.2*.

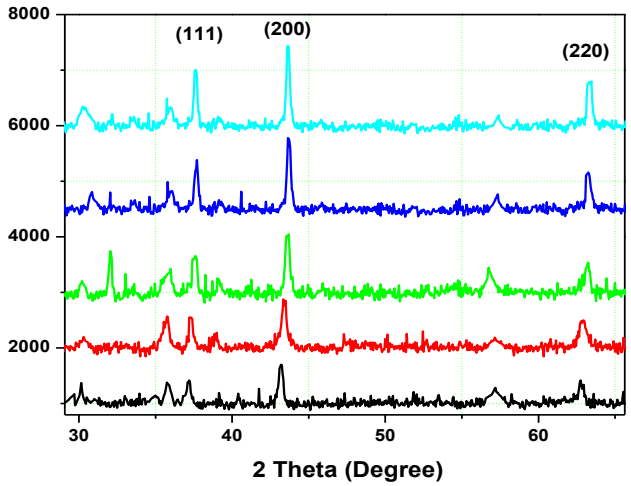

Figure 9.2: Extended view of XRD patterns of $(NiO)_x/(CuFe_2O_4)_{(1-x)}$.

9.2.2 Morphological Study

To investigate the morphology and grain size of composite samples, *TEM* analysis was performed. The *TEM* images reveal the spherical morphology of $CuFe_2O_4$ and *NiO* nanoparticles. The *TEM* images of composites sample as shown in *Fig. 9.3 (a-e)* also demonstrate the spherical morphology, which preserved with incorporation of *NiO* contents and behaves like a core-shell structure. The average particle size increases from 20-35 nm with surge in *NiO* contents in $(NiO)_x/(CuFe_2O_4)_{(1-x)}$ (x=10 to 50 wt.%) composites as estimated by *TEM* micrographs.

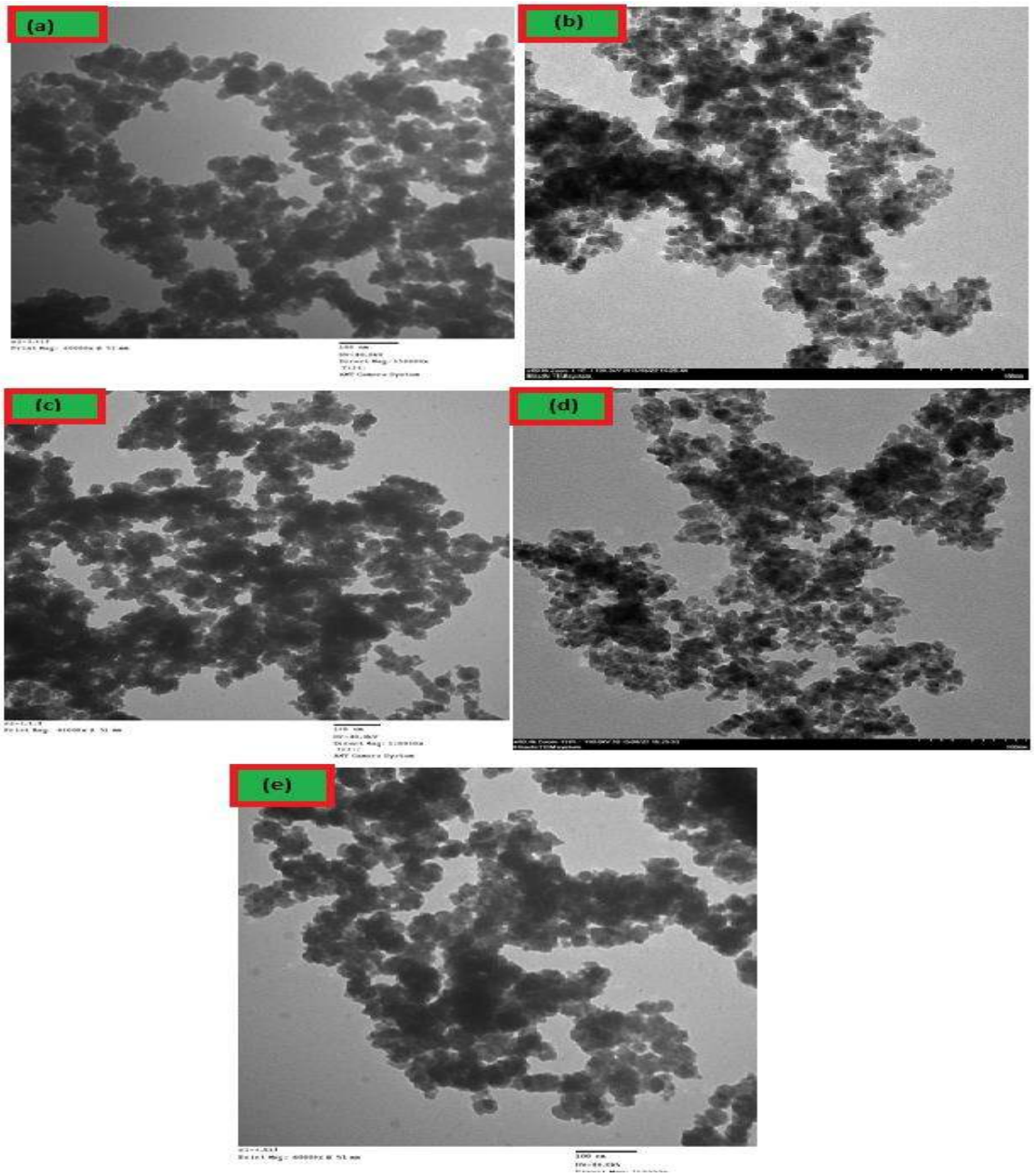

Figure 9.3: (a to e) TEM images of $(NiO)_x/ (CuFe_2O_4)/_{(1-x)}$ (x=10 to 50 wt. %)

9.2.3 Vibrational Analysis

Fig. 9.4 (a & b) shows the absorption spectra of prepared samples. In *Fig. 9.4 (a)* the characteristics absorption bands (at 433 cm^{-1} and 540 cm^{-1}) attributed to vibration of metal ions

at octahedral and tetrahedral sites of $CuFe_2O_4$ respectively [262]. Moreover, the stretching vibration mode of (*Ni-O*) has also been observed at absorption band near 628- 957 cm^{-1}.

The bands related to stretching and bending vibration modes of hydroxyl groups (O-H) and water molecules (H-O-H) may also been observed at 3430 cm^{-1} and 1606 cm^{-1} respectively [263,264].

Figure 9.4 (b) demonstrates the absorbance spectra of composite samples $(NiO)_x/(CuFe_2O_4)_{(1-x)}$ *(x=10 to 50 wt. %),* in which the absorption bands of both phases are present. Hence, the *FTIR* absorption spectra confirm the presence of both phases ($CuFe_2O_4$ and *NiO*) in composite samples.

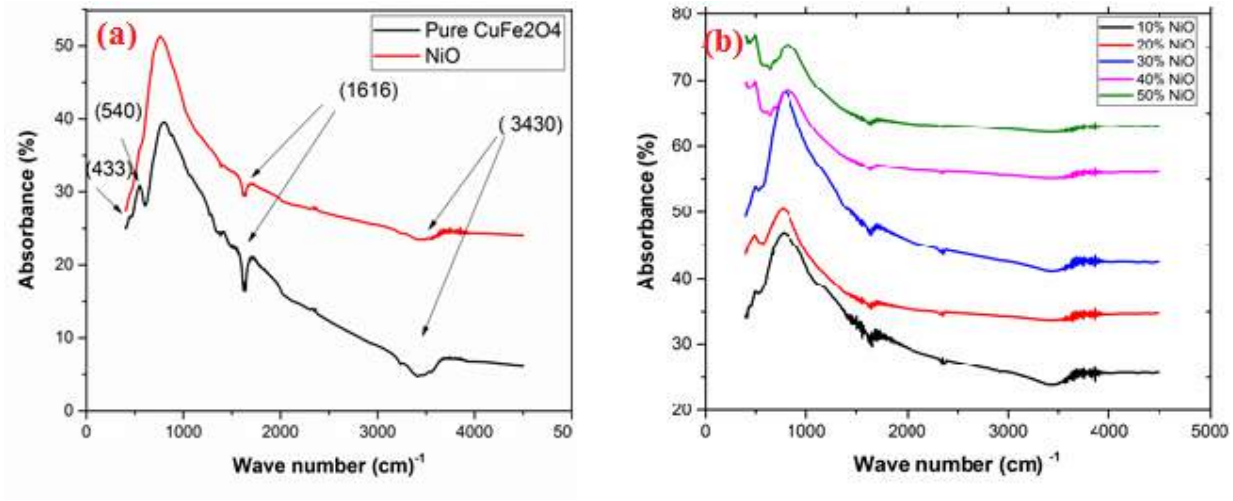

Figure 9.4: FTIR Spectra of (a) Pristine $CuFe_2O_4$ and NiO (b) $(NiO)_x/(CuFe_2O_4)_{(1-x)}$ (x=10 to 50 wt. %) nanocomposites.

9.2.4 Magnetic Properties

Figure 9.5 depicts the hysteresis loops of $(NiO)_x/(CuFe_2O_4)_{(1-x)}$ nanocomposites at room temperature under applied field of $\pm$ 7 k Oe. These *M-H* loops reveal that all the samples have the same ferromagnetic behavior of normal ferrite. However, the incorporation of *NiO* contents in the composite sample of $CuFe_2O_4$ drastically affects the magnetic properties. The decrease in M_S value of composite sample is observed which is attributed to antiferromagnetic (*AFM*) nature of *NiO* at room temperature (*M-H* loop shown in *Fig.4.4*). The increase in weight fractions of *NiO*

(nonmagnetic) contents, in a composite sample of $CuFe_2O_4$ reduces the mass fractions contributing the magnetic orders under an applied field. As a result, one would expect, the overall magnetic property, to decrease, as observed and separately shown in *Fig.9.6 (a).*

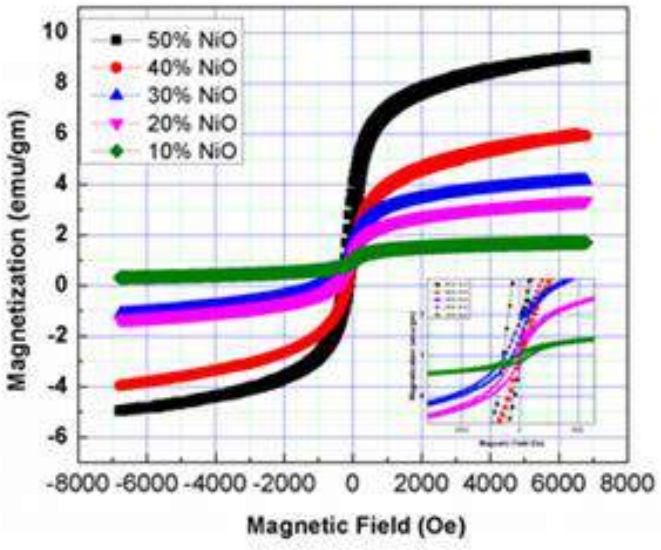

Figure 9.5: M-H loops of $(NiO)_x/(CuFe_2O_4)_{(1-x)}$ (x=10 to 50 wt. %) nanocomposites.

Moreover, *Fig.9* shows that H_c of the composite of $CuFe_2O_4$ decreases with the addition of *NiO* weight fractions and this decreasing trend shown in *Fig.9.6 (b).* The addition of *NiO* concentration, enhance the grain size of composite samples which is attributed to increase in oxygen vacancies as shown in *TEM* images (*Fig.9.3*). The coercivity (H_c) of nanoparticles strongly depend on grain size, with increase in grain size the value of H_c decreases [265]. Therefore, the increase in weight fractions of *NiO* in composite samples shows a decreasing trend in H_c as can be observed in Fig. 9.6 (b).

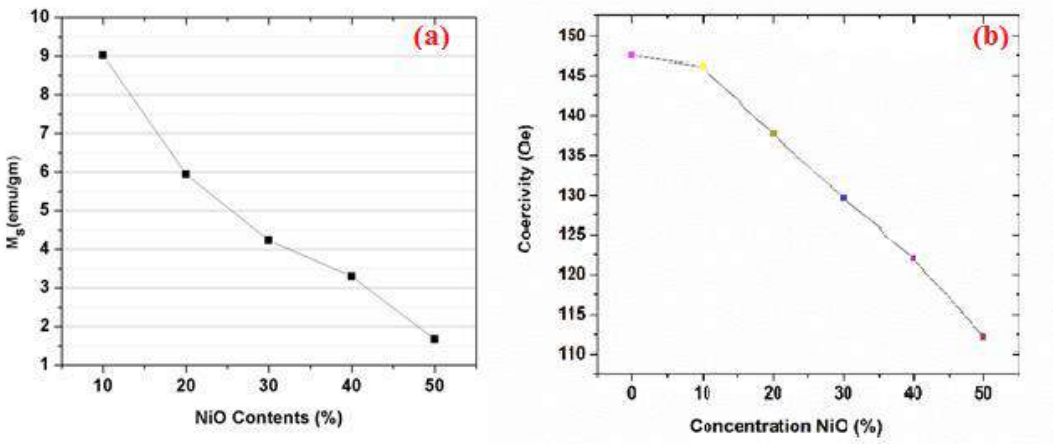

Figure 9.6: Effect of NiO concentrations on (a) M_s and (b) H_c of nanocomposite.

9.2.5 Microwave Absorption Properties

The consequence of *NiO* contents on the *MW* absorption properties of composite samples has also been studied comprehensively in the frequency range 2-10 *G Hz* at room temperature. *Fig. 9.7* shows a shift in absorption peaks towards higher frequency with *NiO* contents (10- 50 wt. %) in composite samples. The strength of absorption peak increases from 19.39 *dB* to 47.26 *dB* (30 wt. % *NiO*) and then decreases to 19.36 *dB* (50 wt. % *NiO*). In *Fig. 9.7*, there is slight change in bandwidth below -10 dB (90% absorption) was also observed with addition of *NiO* contents. The manifestation of this strong *MW* absorption as shown in *Fig. 9.7* in composites samples (10 to 40 wt. %) may be attributed to the increase in the dielectric loss value. Commonly, in the composites system, the dipole polarization plays a dominant role at a higher frequency [266]. Therefore, increased in the strength of absorption peaks in the frequency range 7-8 G Hz with incremental change in *NiO* contents is due to the growth of dipole polarization. *Chen et.al* reported that an enormous contents of crystalline and disorder interface in composite samples produce the combined movement of interfacial dipoles which is called the collective movement of interfacial dipole (CMID) mechanism [266]. As $(NiO)_x/(CuFe_2O_4)_{(1-x)}$ (x=10 to 50 wt. %) nanocomposites contain a large number of crystalline and disorder interface, which can behave as polarization

center to produce more polarization relaxation than that of pristine $CuFe_2O_4$ and consequently enhance the absorption strength of *EM* waves.

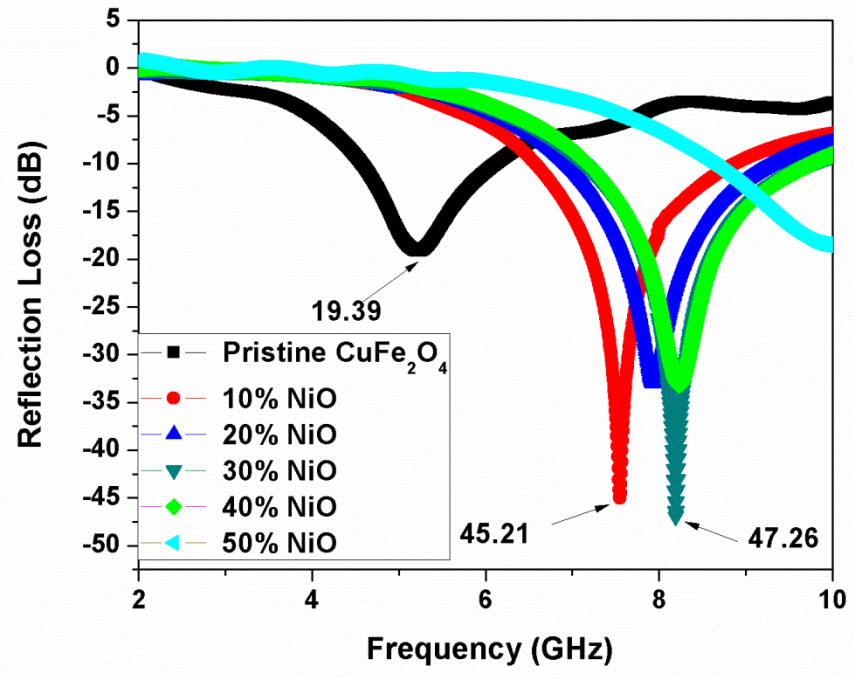

Figure 9.7: RL of $(NiO)_x/(CuFe_2O_4)_{(1-x)}$ (x=10 to 50 wt.%) nanocomposites at thickness of 2mm

Table – 9.1: Magnetic and MW absorption Parameters for $(MOs)_x/(CuFe_2O_4)_{(1-x)}$ (M=Zn, Mg, W, Sn and Ni) Nanocomposites.

Sample Composition	Maximum (RL)	Effective Band Width (G Hz)	Particle Size (nm)	M_s (emu/gm)	H_c (Oe)
Pristine $CuFe_2O_4$	-19.39	1.23	31	30.78	0
$(ZnO)_{0.10}/(CuFe_2O_4)_{0.90}$	-18.40	1.87	55	24.10	0
$(ZnO)_{0.20}/(CuFe_2O_4)_{0.80}$	-20.91	2.94	61	19.77	0
$(ZnO)_{0.30}/(CuFe_2O_4)_{0.70}$	-42.35	4.33	67	17.02	0
$(ZnO)_{0.40}/(CuFe_2O_4)_{0.60}$	-30.17	10	79	16.45	0
$(ZnO)_{0.50}/(CuFe_2O_4)_{0.50}$	-27.99	9.9	81	13.71	0
$(MgO)_{0.10}/(CuFe_2O_4)_{0.90}$	-17.15	2.02	32	28.62	0
$(MgO)_{0.20}/(CuFe_2O_4)_{0.80}$	-18.96	3.58	29	20.20	0
$(MgO)_{0.30}/(CuFe_2O_4)_{0.70}$	-20.46	4.08	30	18.52	0
$(MgO)_{0.40}/(CuFe_2O_4)_{0.60}$	-24.34	10	26	14.47	0
$(MgO)_{0.50}/(CuFe_2O_4)_{0.50}$	-25.35	10	20	11.78	0
$(WO_3)_{0.10}/(CuFe_2O_4)_{0.90}$	-19.39	2.2	20	20.68	0
$(WO_3)_{0.20}/(CuFe_2O_4)_{0.80}$	-18.02	2.7	27	13.95	0
$(WO_3)_{0.30}/(CuFe_2O_4)_{0.70}$	-18.74	2.6	25	12.15	0
$(WO_3)_{0.40}/(CuFe_2O_4)_{0.60}$	-26.32	1.8	30	7.69	0
$(WO_3)_{0.50}/(CuFe_2O_4)_{0.50}$	-18.38	2.3	22	5.16	0
$(SnO_2)_{0.10}/(CuFe_2O_4)_{0.90}$	-22.22	3.86	20	24.03	26.44
$(SnO_2)_{0.20}/(CuFe_2O_4)_{0.80}$	-28.37	3.57	25	20.10	24.12
$(SnO_2)_{0.30}/(CuFe_2O_4)_{0.70}$	-15.37	3.17	27	15.97	20.77
$(SnO_2)_{0.40}/(CuFe_2O_4)_{0.60}$	-19.69	3.07	28	8.77	12.28
$(SnO_2)_{0.50}/(CuFe_2O_4)_{0.50}$	-20.58	2.69	30	6.98	10.47
$(NiO)_{0.10}/(CuFe_2O_4)_{0.90}$	-45.21	2.33	22	9.00	146.20
$(NiO)_{0.20}/(CuFe_2O_4)_{0.80}$	-33.08	2.45	25	5.99	137.68
$(NiO)_{0.30}/(CuFe_2O_4)_{0.70}$	-47.26	2.2	31	4.23	129.76
$(NiO)_{0.40}/(CuFe_2O_4)_{0.60}$	-33.32	2.52	32	3.44	122.07
$(NiO)_{0.50}/(CuFe_2O_4)_{0.50}$	-18.66	1.42	36	1.63	112.02

Chapter No. 10

Conclusions and Future Perspectives

10.1 Conclusions

In this research study the $(MOs)_x/(CuFe_2O_4)_{1-x}$ nanocomposites with different weight fractions of *MOs* nanostructures were synthesized by *ex-situ* method. Their structural, morphological, magnetic and *MW* absorbing properties were also studied extensively. The *XRD* pattern and vibrational analysis confirm the formation of nanocomposites without any impurity phase. The *SEM* analysis demonstrates the different morphologies for *MOs* nanostructures attributed to the difference in electronegativity and oxygen vacancies. The *TEM* micrographs of composite samples show that the particles are in nanoscale and behave like core/shell structures in which *MNPs* of $CuFe_2O_4$ embedded in *MOs* matrix. The *VSM* study elucidates the superparamagnetic behavior of pristine $CuFe_2O_4$ *MNPS* and manifestation *of RTFM* behavior is also observed in *MOs* nanostructures. The impregnation of nonmagnetic contents of *MOs (M=Zn Mg and Sn)* nanostructures in composite samples show the same superparamagnetic behavior with decrease in M_s values from 30.78 emu/gm to 5.16 emu/gm. However, *M-H* loops of WO_3 and *NiO* composite samples demonstrate the same decrease in M_s value with systematic change in coercivity. The increase in coercivity from (600 to 718 Oe) in WO_3 samples is attributed to the shape anisotropy that originates with changing the shape of particles from spherical to nanoplatelets. The *NiO* composite samples show decrease in coercivity from 146.20 to 112.02 Oe) due to the growth in particle size that results in decrease the anisotropic energy. This decrease in H_c values make this composite materials $(NiO)_x/(CuFe_2O_4)_{1-x}$ a potential candidate for transformer core where low eddy current losses are required at higher frequency.

The *MW* absorption measurement, which is the main objective of this research have been performed in the frequency range 2-10 *GHz* and also studied in detail. The pristine $CuFe_2O_4$ *MNPs* having large value of anisotropy energy and small value of dielectric loss shows a maximum *RL* -19.39 *dB* at 5.21 *GHz*. The selected *MOs* nanostructures with different morphologies behave as a dielectric loss filler in the magnetic nanocomposite and tune the *MW* absorption properties. The *MW* absorption properties of material depend upon the interfacial polarization, dipolar polarization and the impedance matching condition. In $(ZnO)/(CuFe_2O_4)$ nanocomposites, the 30 wt.% of *ZnO* contents gives maximum *RL* -42.35 *dB* (99.999 %) at 8.35 *G Hz.* The further increase in *ZnO* contents up to 50 wt. % enhance the effective absorption (90 %) in the whole frequency band 2-10 *G Hz* due to increase in the interfacial polarization.

In $MgO/CuFe_2O_4$ nanocomposites, there is no absorption band (below -10*dB)* up to 30 wt.% of *MgO* was observed but 40 wt.% of *MgO* contents shift the absorption curve to higher frequency, enhance the strength of absorption abilities and widen the effective absorption band (2-10 *GHz*). The 50 wt. % of *MgO* contents in composite sample reduces the effective absorption bandwidth to 8 *GHz* due to mismatch of dielectric and magnetic loss. The $WO_3/CuFe_2O_4$ nanocomposites demonstrate the slight variation in absorption peaks towards higher frequency with increase in WO_3 weight fractions up to 20 wt. %. The 30 wt. % additions of WO_3 contents in composite sample produce an enhancement in *RL* to -26.32 *dB* at 6.6 *GHz*. The further addition of WO_3 weight fraction lower the *RL* and shift the absorption peak towards higher frequency attributed to tailor in the resonant frequency. The *chapter* eight also demonstrates the high frequency *MW* absorption properties of $(SnO_2)_x/(CuFe_2O_4)_{(1-x)}$ (x=10 to 50 wt. %) nanocomposites from 2-10 *G Hz*. The 10 to 20 wt. % loading of SnO_2 enhance the strength of *RL* from -22.37 *dB* to -28.37 *dB* respectively. The higher loading fraction (30-50 wt.%) reduce the strength of *MW* absorption due to the

decrease in the synergistic effect in the dielectric and magnetic properties in the composite samples. This reduction in synergistic effect disturbs the impedance of material and lowers the absorption of *MW* in required frequency. Finally, the effect of *NiO* weight fractions on *MW* absorption characteristics of composite samples has also been analyzed in chapter nine. There is increase in *RL* from -19.39 *dB* to -47.26 *dB* (30 wt. % *NiO*) towards higher frequency was observed. This increase in strength of *MW* absorption properties is attributing to the increase in dipolar polarization as compared to interfacial or space charge. Therefore, increased in the strength of absorption peaks in the frequency range 7-8 *G Hz* with incremental change in *NiO* contents is attributed to the enhancement of dipole polarization.

Hence the loading of *MOs* nanostructures with different morphologies lead the composite sample towards higher dielectric loss and also tunes the resonant frequency. The impregnation of dielectric fillers in *MNPs* produces large number of grain boundaries and interfaces. The growth of charges at the grain boundaries produces the polarization and hence this mechanism contributes to enhance the strength of *MW* absorption in wide band. The strength of *MW* absorption of nanocomposites material also demands a matching of dielectric loss and magnetic loss. Therefore, the choice of dielectric filler and optimal size and shape of particles also play an important role to enhance the strength of *MW* absorption. Hence, depending upon the dielectric filler properties and as well as filler loadings, one can tune absorption properties of nanocomposites in required frequency band width.

Hence in this study it is concluded that a judicious choice of *MOs* nanostructures with appropriate weight fractions can give a combination of dielectric and magnetic properties suited for various applications.

10.2 Future Perspectives

In future research, we would like to conduct a comprehensive *MW* study, to investigate the probable mechanism involved for *MW* absorption properties of $(MOs)_x/(CuFe_2O_4)_{(1-x)}$ *(M=Zn, Mg, W, Sn and Ni)* nanocomposites. The response of complex permittivity and permeability with frequency may provide the exact mechanism involved for the dissipation of energy responsible for *MW* absorption. Unfortunately this technique is not available to us and we may search new collaboration in order to fulfill this requirement.

Further work can also be carried out with different ferrites and metal oxides nanostructures having light weight, which enhance the strength of absorption in wide band.

References

[1] A. K. Rafaqat, S. Mizukami, A. M. Khan, B. Ismail, A. R. Khan, T. Miyazaki, *J. Alloy.Compd.* 637 (2015) 202.

[2] Q. H. Liu, Q. Cao, X. B. Zhao, H. Bi, C. Wang, D. S. Wu, R. C. Che, *ACS Appl. Mater. Inter.* 7 (2015) 4240.

[3] X. G. Huang, Y. Y. Chen, J. H. Yu, J, Zhang, T. Y. Sang, G. X. Tao, H. L. Zhu. *J. Mater. Sci. Mater. Electron*. 26 (2015) 3478.

[4] E. F. Knott, J. F. Shaeffer and M. T. Tuley, Radar Cross Section (SciTech Publishing,1993).

[5] D. D. L. Chung. Electromagnetic interference shielding effectiveness of carbon materials. *Carbon*, 39 (2) (2001), 285.

[6] W.Zhu, L.Wang, R Zhao, J.Ren, G.Lu and Y. Wang, *Nanoscale*, 3 (2011), 2864.

[7] Y.B. Feng, T. Qiu, C.Y. Shen, , *J.Magn. Magn. Mater*. 318 (2007) 13.

[8] Y.B. Feng, T. Qiu, C.Y. Shen, , *J.Magn. Magn. Mater*. 318 (2007) 13.

[9] C.L. Yuan, Y.S. Tuo, *J.Magn. Magn. Mater*. 342 (2013) 53.

[10] H.B. Yang, T. Ye, Y. Lin, M. Liu, *Appl. Surf. Sci.* 357 (2015) 1293.

[11] H.B. Yang, M. Liu, Y. Lin, Y.Y. Yang, *J. Alloys Compd*. 631 (2015)339.

[12] Y.J. Chen, F. Zhang, G.g.Zhao, X.y.Fang, H.B. Jin, P. Gao, C.L. Zhu ,,M.S. Cao and G. Xiao, *J.Phys.Chem.C*, 114 (2010) 9244.

[13] Goldman, A. *Modern Ferrite Technology*; Van Nostrand Reinhold: New York, (1990).

[14] Rastogi, A. C.Dhara, S. Das, B. K. *J. Electrochem. Soc. 142* (1995)3148.

[15] Liu, T. Y. Hu, S. H.Liu, K. H. Liu, D. M. Chen, S. Y. *J. Magn.Magn. Mater. 310* (2007) 2850.

[16] Chung, K. W.Kim, K. B. Han, S. H. Lee, H. *Electrochem. Solid State Lett.* A, *8* (2005) 259.

[17] Kuo, S. L.Wu, N. L. *Electrochem. Solid State Lett. A* 8 (2005) 495.

[18] M.S. Tomar, S.P. Singh, O. Perales-Perez, R.P. Guzman, E. Calderon, C. Rinaldi-Ramos, *Microelectr. Jour.*36, (2005) 479.

[19] U. Lüders, A. Barthélémy, M. Bibe, K.Bouzehouane, S. Fusil, E.Jacquet, J.P. Contour, J.-F. Bobo, J. Fontcuberta, A. Fer ,. *Ad*V. *Mater. 13* (2006) 1733.

[20] Yang, G. Q. Han, B. Sun, Z. T. Yan, L. M. Wang, X. Y. *Dyes Pigm.* 9 (2002)*55*.

[21] A.Kalendova, D.Vesely, J. Brodinova, *Anti-Corros. Methods Mater. 51* (2004)17.

[22] Proodelalova, J. Rittich, B. Petrova, K. Benes, M.J. *J. Chromotagr*.43 (2004)*1056*.

[23] G.F. Goya, H.R. Rechenberg, *J. Appl. Phys.* 84 (1998) 1101.

[24] J. Janicki, J. Pietrzak, A. Porebska, and J. Suwalski, *Phys. Status Solidi.A.* 72, (1982) 95.

[25] O. Muller and R. Roy, *Crystal Chemistry of Non-Metallic Materials*, (Springer-Verlag, Berlin, 1974).

[26] R. Valenzuela, Ed. B. Dunn, J. W. Goodby, A. R. *Magnetic Ceramics, Chem. of Sol. State Mater.*, Series West, (Cambridge Univ. Press, Cambridge1994).

[27] H.H. Kung, Transition Metal Oxides: *Surface Chemistry and Catalysis;* Elsevier: Amsterdam,(1989).

[28] M.L. Trudeau, J.Y. Ying, *Nanostructured Mater*.7, (1996) 245.

[29] R.E. Presley, C.L. Munsee, C.-H. Park, D. Hong, J.F. Wager, D.A. Keszler, J. *Phys. D.* 37, (2004) 2810.

[30] X.Wang, J.Song, Z.L. Wang. *Mater. Chem.* 17 (2007) 720.

[31] Z.L.Wang, J.H.Song *Science,* 312 (2006) 246.

[32] R. F. Zhuo, H. T. Feng, J. T. Chen, D. Yan, J. J. Feng, H. J. Li, B. S. Geng, S. Cheng, X. Y. Xu, and P. X. Yan, *J. Phys. Chem.C.*, 112 (2008) 11767.

[33] R. F. Zhuo, L. Qiao, H. T. Feng, J. T. Chen, D. Yan, Z. G. Wu, *and* P. X. Yan, *J. Appl. Phys.*, 104 (2008), 094101.

[34] Q. Zhang, P. J. McGinn, *J. Americ. Ceram*.89 (12) (2006) 3823.

[35] J.Z Ou, S. Balendhran, M. R. Field, D. G. McCulloch, A. S. Zoolfakar, R. A.Rani, S. Zhuiykov, A. P. O.Mullane and K. Kalantar-zadeh.*Nanoscale*. 19 (2012) 5988

[36] S.K.Deb. *Solar Energy Mater. and Solar Cells*. 92 (2008) 258.

[37] J.M.Berak, M.J Sienko, *Solid State Chem*. 2 (1970) 133.

[38] D. J. Ham,A. Phuruangrat ,S. Thongtem, J. S. Lee, *J.Chem Eng.* 165 (2010) 369.

[39] G. Gu ,B. Zheng, W. Q. Han,S. Roth and J. Liu, *Nano Letters*, 8 (2002) 851.

[40] S.H. Lee, R. Deshpande. A. Parilla,K. M. Jones,B. To,A. H. Mahan,A. C. Dillon**.** *Adv Mater*.18 (2006) 766.

[41] B.G. Lewis, D.C. Paine, *Mater. Res. Soc. Bull*. 25 (2000) 23.

[42] A. Maddalena, R.D. Maschio, S. Dire, A. Raccanelli, *J. Non-Cryst. Solids121* (1990) 365.

[43] S.S. Kim, S.Y. Choi, C.G. Park, H.W. Jin, *Thin Solid Films* 347 (1999)155.

[44] C. Kilic and A. Zunger, *Phys. Rev. Lett.* 88 (2002) 095501.

[45] S.Zhuiykov, Properties and Applications 484. Cambridge, UK: Woodhead Publishing; (2014).

[46] S.Balendhran, J. Deng , J.Z.Ou , S.Walia , J.Scott , J.Tang , K.L.Wang,M.R. Field, S.Russo S.Zhuiykov, M.S.Strano, N.Medheka, S.Sriram, M. Bhaskaran, K. Kalantar-zadeh K. *Adv Mater*. 25 (2013)109-114.

[47] T.P. Hulser, H. Wiggers, F.E. Kruis, A. Lorke, *Sens. Actuators B* 109 (2005) 118.

[48] K. Kamalpreet, A. Mahajan, R.K. Bedi, J. *Appl. Surf. Sci*. 257 (2011) 2934.

[49] O. Bidault, M. Maglione, M. Actis, M. Kchikech, *Phys. Rev. B* 52 (1995) 4191–4197.

[50] L. Chen, L. Li, G. Li, J. *Solid State Chem.* 181 (2008) 2073–2077.

[51] T.P. Hulser, H. Wiggers, F.E. Kruis, A. Lorke, *Sens. Actuators B* 109 (2005) 118.

[52] K. Kamalpreet, A. Mahajan, R.K. Bedi, *J. Appl. Surf. Sci.* 257 (2011) 2934.

[53] M.L. Cukrov, T. Tsuzuki, P.G. Mc Cormick, *Script. Mater*. 44 (2000) 1790.

[54] S. Gautam,A. Thakur,A.Vij,J. Suk, Ik-Jae Lee, *Thin Solid Films* 546 (2013)254.

[55] P.Poizot, S.Laruelle, S.Grugeon , L.Dupont , J.M.Tarascon, *Nature* 407 (2000) 499.

[56] H.L. Tasi, J. L. Schindler, C. R. Kannewurf and M. G. Kanatzidis, *Chem.Mater.* 9 (1997) 878.

[57] P.M. Ajayan, L.S. Schadler and P.V.Braun, *Nano compo. Sci. and Tech.*, (2003).

[58] A. C. Razzitte, W. G. Fano and S. E. Jacobo, *Physica B* 354 (2004)231.

[59] Y. Shen, Z.Yue, M. Li and C.W. Nan, *Adv. Funct. Mater.* 15 (2005) 1100.

[60] P. V. Kamat, *J. Phys. Chem. B* 106 (2002)7244.

[61] P. Penwisa, M. Rathanawan, and C. J. Sadhan, *J.Nano. Mater.* (2012).

[62] D.X.Yan, H.Pang, L.Xu,Y.Bao, P.G.Ren, J.Lei, and Z.M.Li , J. of Nanotech., 25 (2014),145705.

[63] G. A. Gelves, M. H. Al-Saleh, and U. Sundararaj, *J. Mater. Chem.* 21(2011),829.

[64] M. H. Al-Saleh and U. Sundararaj. *Carbon*, 47(2009), 1738.

[65] B. E. Keiser "Principles of electromagnetic compatibility" Artech House Microwave

Library,(1979).

[66] F. Qin and C. Brosseau. *J. Appl. Phys.*111 (6), 061301,

[67] V. G. Harris, A. Geiler,Y. Chen,S. D.Yoon,M. Wu,A. Yang,Z. Chen,P. He, P.V. Parimi,X. Zuo,C. E. Patton, M. Abe,O. Acher, and C. Vittoria, *J. Magn. Magn.Mater.* 321 (2009) 2035.

[68] W. Liu, W. Zhong, H. Y. Jiang, N. J. Tang, X. L. Wu, and W. Y. Du. *Eur. Phys.*46 (2005), 471.

[69] X. F. Zhang, P. F. Guan, and X. L. Dong. *Appl. Phys. Lett.*97 (2010), 033107.

[70] R.Dosoudil, M.Usakova, J. Franek, J. Slama, A. Gruskova, J. Slama, and A. Gruskov *Polym. Compos. Magn*. 46 (2010) 436.

[71] A.H. Habib, S.Xu, E.Walker,M. Ondeck,R. Swaminathan, and M. E.McHenry. *J. Appl. Phys*.(7) (2012) 111.

[72] X. F. Zhang, X. L. Dong, H. Huang, Y. Y. Liu, W. N. Wang, X. G. Zhu, B. Lv,J. P. Lei, and C. G. Lee. *Appl. Phys. Lett*. 89 (2006).

[73] X. G. Liu, B. Li, D. Y. Geng, W. B. Cui, F. Yang, Z. G. Xie, D. J. Kang, and Z. D. Zhang, *Carbon*,47 (2009) 474,.

[74] D. Hasegawa, H. Yang, T. Ogawa, and M. Takahashi. *J. Magn.Magn.Mater*.321 (2009) 749.

[75] R. Lv, F. Kang, J. Gu, X. Gui, J. Wei, K. Wang, and D. Wu .*Appl. Phys. Lett*.93(2008).

[76] R. K. Srivastava, T. N. Narayanan, A. P. Reena Mary, M. R. Anantharaman,A. Srivastava, R.Vajtai, and P. M. Ajayan. *Appl.Phys. Lett.* 99 (2011).

[77] X. Gui, W. Ye, J. Wei, K. Wang, R. Lv, H. Zhu, F. Kang, J. Gu, and D. Wu.*J. Phys. D: Appl. Phys*.42 (2009) 75002.

[78] M. Crespo,N. M_endez,M. Gonz_alez,J. Baselga, and J. Pozuelo. *Carbon*, 74 (2014) 72.

[79] A.P.Singh, P.Garg, F.Alam, K.Singh, R.Mathur, R.Tandon, A.Chandra, and S. Dhawan. *Carbon*, 50 (2012) 3875.

[80] T. Wang, Z. Liu, M. Lu, B. Wen, Q. Ouyang, Y. Chen, C. Zhu, P. Gao, C. Li,M. Cao, and L. Qi.J. *Appl. Phys.*113 (2013) 024314.

[81] K.Y.Park, J.H. Han, S..B. Lee, J.B. Kim, J.W. Yi, and S.K. Lee. *Compos. Sci. Technol.* 69 (2009)1278.

[82] R.C.Che, C.Y. Zhi,C.Y. Liang, and X. G. Zhou. *Appl. Phys. Lett.* 88 (2006) 033105.

[83] F. Wen, F. Zhang, and Z. Liu *J. Phys. Chem. C,* 115 (2011)14030.

[84] R.C.Che, L. M. Peng, X. F. Duan, Q. Chen, and X. L. Liang. *Adv. Mater*.16 (2004) 401.

[85] F. Qin and C. Brosseau. *J. Appl. Phys.*111 (2012) 061301.

[86] Z.H. Peng, J.C. Peng, Y.F. Peng, Y.Y. Ou, Y.T. Ning, *Phys. Lett. A* 372 (2008) 3714.

[87] Y.B. Li, R. Yi, A. Yan, L.W. Deng, K.C. Zhou, X.H. Liu, *Solid State Sci.* 11 (2009)1319.

[88] R. Moucka, M. Mravcakova, J. Vilcakova, M. Omastova, P. Saha, *Mater. Des.* 32 (2011) 2006.

[89] K.Y.Chen,L.C. Li, G.X. Tong, R. Qiao, B. Hao, X.X. Liang, *Synth. Met.* 161 (2011) 2192.

[90]Ying Lin,Xiao Liu,Ting Ye,Haibo Yang,Fen Wang,Chun Liu**,** *Jour. of Mater. Sci. Mater. in electron.*, 27(2016) 4838.

[91] M. Faisal, S. Khasim, *Jour. of Mater Sci: Mater in Electron.*, 24 (2013) 2210.

[92] G.Wang, X. Peng, L. Yu,G. Wan,S. Lin and Y. Qin, *J. Mater. Chem.A*,3(2015) 2740.

[93] W. Widanarto, F.M. Rahayu, S.K. Ghoshal, M. Effendi,W.T. Cahyanto, *Resul. in Phy.* 5 (2015) 256.

[94] C.D.Pina,E. Falletta, A. M. Ferretti, A. Ponti, G. G. Gentili, V. Verri, and R. Nesti, *J.of Appl.Phys.*116 (2014) 154306.

[95] A. Poorbafrani, P.Kameli, H. Salamati, *J. of Mater. Sci.*,48 (2013) 191.

[96] K.C.Tripathi, S.M.Abbas, P.S.Alegaonkar, R.B. Sharma, *Int. Jour. of Adv. Resea*. in Science, Engineering and Technology 2 (2015) 463.

[97] H.Yang**,** T. Ye and Y. Lin **,***RSC Adv.5* (2015)103493.

[98] B.Li, X.Weng, G.Wu, Y. Zhang, X.Lv , G. Gu Jour. of Saudi Chem. Soci.,21 (2016) 472.

[99] J.Guo,Y.Dan,L.Liu, L. Chen, S. Liu, *Jour. of Electrom. Anal and Appli*, 3 (2011)146.

[100] X.Qin,Y. Cheng, K. Zhou, S. Huang, X. Hui, *Jour. of Mater. Sci. and Chem. Eng.* 5 (2013)13.

[101] Y.Ding,Q.Liao, S. Liu,H.Guo, Y.Sun, G.Zhang and Y.Zhang, *Sci Rep*.6 (2016) 32381.

[102] Y.Chen , Z.Lei, H.Wu, C.Zhu, P.Gao, Q.Ouyang, L.H.Qi, W.Qin, *Mater Rese.Bull.*,9 (2013)3366.

[103] M.Verma, A.P.Singh, P.Sambyal, B.P.Singh, S.K.Dhawanand, V.Choudhary, *Phys. Chem. Chem. Phys.*17,(2015)1618.

[104] L.Kong, X.Yin, Y.Zhang, X.Yuan, Q.Li, F.Ye, L.Cheng, and L. Zhang ,*J. Phys. Chem. C,* 38 (2013)19711.

[105] Y.Yin, M.Zeng, J.Liu, W.Tang, H.Dong, R.Xia and R.Yu. *Sci. Rep*. 6 (2016) 25075.

[106] F.Wu, Y.Xia, Y. Wang and M. Wang , *J. Mater. Chem.* A, (2)201420315.

[107] S.A. Rakha, A. A. Khurram, N.Ali, A. Munir, A.Iqbal, T. Subhani, I. H. Gul, *J. of adv. in polym. Tech*., 34 (2015).

[108] Y.Arooj,Y. Zhao, X. Han,T. Bao, Y.Wang, *J. of poly. for adv. Tech.* 26 (2015) 625.

[109] Ruey-Bin Yang,Wen-Shyong Kuo,Heng-Chih Lai, *J. of appl. poly. Sci.* 131(2014) 21 .

[110] T. Wang, Z. Liu,M. Lu, B. Wen, Q. Ouyang, Y. Chen,C.Zhu, P. Gao, C. Li, M. Cao, and L. Qi, *J. of appl. Phy*. 113 (2013) 024314.

[111] S. Bindra, N. Pubby, S.K. Chawla, P. Kaur. *J.Ferroelectric*, 505 (2016) 73.

[112] L. Zhu, X. Zeng, X. Li, B. Yang, R. Yu. *J. Magn.Magn.Mater* .426 (2016)120.

[113] W.C.Li,J. Lv, X. Zhoua, J. Zhenga, Y. Yinga, L. Qiaoa, J. Yua,S. Chea, *J.Ferroelectric*, 203 (2016).

[114] J.Luo, P.Shen,W.Yao, C. Jiang and J. Xu. *Nanosc. Resea. Lett.* (2016) 11:141.

[115] H. Xu, S.Bie, Y.Xu, W.Yuan, Q. Chen, J. Jiang. *Appl.Sci. and Manuf.*, 80, (2016)117.

[116] X. Huang, J. Zhang, Z. Liu, T. Sang, B. Song, Hongli Zhu,C Wong, *J.*of *Alloys and Comp.*, 648, (2015) 1075.

[117] K. R.Obulesu, T.S. Rao, K.C. J. Raju., *J. of Alloys and Comp.* 695, (2017), 3035.

[118] D. K. Kalluri,**"**Principles of electromagnetic waves and materials" (2013).

[119] X. Zhao,L. Wang,X. Xu,Xi. Lei,S. Xu, and F.Zhang, *Mater., Inter, and Electrochemical Pheno.* (2011) 12597.

[120] A. Sundaresan, R. Bhargavi, N. Rangarajan, U.R. Siddesh, C.N.R. Rao, *Phys. Rev. B* 74 (2006) 161306.

[121] D. Pozar, *Microwave Engineering*, (2004).

[122] E. F. Knott, J. F. Shaeffer and M. T. Tuley, *Radar Cross Section* (1993).

[123] M.Hill, TheMicrowave Palaeointensity Technique and its Application to Lava, PhD. Thesis, University of Liverpool, (2000).

[124] A.J. Moulson and J. M. Herbert, *Electrocer: Mater*, Prope, Applications, 2nd.ed. (2003).

[125] C. Kittel, *Physical Review*, 73,2 (1948).

[126] J. Huo, L. Wang and H. Yu, *J. of Mater. Sci.* 44 (2009) 3917.

[127] J.L. Snoek, Physica, 14 (1948) 207.

[128] L. Landau and E.Lifshitz, *Phys. Z. Soviet Union*, 8 (1935) 153.

[129] P. Ravikumar, B. Kisan, and A. Perumal, "*AIP ADV."* 5(2015), 087116.

[130] R. F. Zhuo, H. T. Feng, J. T. Chen, D. Yan, J. J. Feng, H. J. Li, B. S. Geng, S. Cheng, X. Y. Xu, and P. X. Yan, Phys. *Chem.C.* 112 (2008)11767.

[131] Y.K.Mishra, S.Kaps, A.Schuchardt,I.Paulowicz, X.Jin, D.Gedamu, S.Freitag, M.Claus, S.Wille, A.Kovalev, S.N.Gorb, R.Adelung, *Part.Syst.Charact*.30 (2013)783.

[132] X.D.Wang, J.H. Song, Z.L. Wang, *J. Mater. Chem.*17 (2007) 720.

[133] R. F. Zhuo, H. T. Feng, J. T. Chen, D. Yan, J. J. Feng, H. J. Li, B. S. Geng, S. Cheng, X. Y. Xu, and P. X. Yan, *Phys. Chem.C.* 112 (2008)11767.

[134] K. J. Klabunde Nanoscale Mater in Chem., Ed. (2001).

[135] H. Gleiter, *Adv. Mater.* 4, (1992) 474.

[136] G. A. Ozin, *Adv. Mater.* 4, (1992) 612.

[137] D. Wang and H. Mohwald, *J. Mater. Chem.* 14 (2004) 459.

[138] X.J. Zhang, G.S. Wang ,W.Q. Cao,Y.Z. Wei, J.F. Liang, L. Guo, M.S. Cao, *ACS, Appl. Mater. Interfaces* 6 (2014) 7478.

[139] Y.H. Huang, X. Chen, Z.M. Wang, C.S. Liao, C.H. Yan, H.W. Zhao, and B.G. Shen, *J. Appl. Phys*.9 (2002) 7733.

[140] B.D. Cullity, Elements of x-ray Diffraction , Addison Wesley publishing Company Inc.

[141] Fundamentals of Fourier Transform Infrared Spectroscopy by Brian C.Smith, by Taylor and Francis Group, *LLC.* (2011).

[142] Introduction to Fourier Transform Infrared Spectroscopy by Thermo Nicolet Corporation E-MAIL: nicinfo@thermonicolet.com & www.thermonicolet.com.

[143] J. Goldstein, D. Newbury, D. Joy, C. Lyman, P. Echlin, E. Lifshin, L. Sawyer and J. Michael, Scanning Electron Microscopy and X-ray Microanalysis, (2003).

[144] D.B.Carter, C.B. Wa, Transmission Electron Microscopy. 2 ed. 2009, New York: Springer.

[145] S. Foner, Rev. Sci. Inst. 30 (1959) 548.

[146] D. C. Sinclair and A. R. West, J. Appl. Phys. 66 (1989) 3850.

[147] L.F.Chen,C. K. Ong, C. P. Neo, V. V. Varadan and V. K. Varadan, Microwave Electronics Measurement and Characterization (2004).

[148] D. Pozar, Microwave Engineering (2004).

[149]J.Baker-Jarvis,E.J.Vanzura,and W.A.Kissick,Trans.Microw. Theory Techn.38(1990),1096-1103

[150] J. Baker-Jarvis. Transmission/reflection and short-circuit line permittivity measurements.

Theory Tech.(1990).

[151] J.M. Thomassin,C.Jerome,T. Pardoen, C. Bailly, C. Je, I. Huynen, and *C. Mater. Sci. Eng*., R, 74 (2013) 232.

[152] A. Azam, A.S. Ahmed, M. Oves, M.S. Khan, S.S. Habib, A. Memic, *Int. J. Nanomed*.7

(2012),6003.

[153] X. Zhao,L. Wang,X. Xu,Xi. Lei,S. Xu, and F.Zhang, *Mater.s Interf. and Electrochemical Phenomena* (2011) 12597.

[154] Y. J. Xing, Z. H. Xi, X. D. Zhang, J. H. Song, R. M. Wang, J. Xu, Z. Q. Xue, and D. P. Yu, *Appl. Phys.A* 80 (2005) 1527.

[155] J. Alaria,H. Bieber,S. Colis,G. Schmerber,A. Dinia, *Appl. Phys. Lett*. 88 (2006) 112503.

[156] A. Sundaresan, R. Bhargavi, N. Rangarajan, U.R. Siddesh, C.N.R. Rao, *Phys. Rev. B* 74 (2006) 161306.

[157] A. Sundaresan, C.N.R. Rao, *Nano Today* 4 (2009) 96.

[158] B.B.Straumal, F.F. Mazilkin, S.G. Protasova, A.A. Myatiev, P.B. Straumal,G. Schütz,P.A. Van Aken, E. Goering, B. Baretzky, *Phys. Rev. B* 79 (2009) 205206.

[159] M.I. Bashir, K, Ali, Sarfraz A. K,I. M. Mirza, "*J.of Alloy and Comp.* 684 (2016) 161.

[160] P. Chetri, B. Choudhury and A. Choudhury" *J. of Mater. Chem. C*: 43 (2014).

[161] N. Kumar, D. Sanyal , A. Sundaresan , *Chemi. Phys. Lett.*, 477 (2009),364.

[162] P. Ravikumar, B. Kisan, and A. Perumal, "*AIP ADVAN*." 5 (2015), 087116.

[163] S.L. Zhang, Q.Z. Jiao, Y. Zhao, H.S. Lia, Q. Wu, *J. Mater. Chem.* A 2 (2014) 18033–18039.

[164] C . Dong, X. Wang, P. Zhou, T. Liu, J. Xie, and L Deng. *J .Magn. Magn. Mater.* (2014) 354-340

[165] J.W.Liu, J.J.Xu, R.C.Che, H.J.Chen, M.M.Liu, Z.W.Liu, *J. Eur.Chem.* 19(2013) 6746–6752.

[166] S.W.Phang, M.Tadokoro, J.Watanabeb, N.Kuramoto, *Polym.Adv.Technol*. 20 (2009) 550–557.

[167] M.R. Dadfar, S.A.S.Ebrahimi, M.Dadfar, *J.Magn.Magn.Mater*.324 (2012) 4204–4208.

[168] L. Kong, X.W.Yin, L.T.Zhang, L.F.Cheng, *J.Am.Ceram.Soc*. 95 (2012) 3158–3165.

[169] R.F.Zhuo, L.Qiao, H.T.Feng, J.T.Chen, D.Yan, Z.G.Wu, P.X.Yan,*J .Appl.Phys.* 104 (2008) 094101.

[170] H.F.Li, Y.H.Huang, G.B.Sun, X.Q.Yan, Y.Yang, J.Wang, Y.Zhang, *J.Phys.Chem. C* 114(2010)10088–10091.

[171] X.B. Wu, H.L.Luo, Y.Z.Wan, *Mater.Lett.*92 (2013)139–142.

[172] B. Zhao, G. Shao, B.B.Fan, C.Y.Wang, Y.J.Xie, R.Zhang, *Powder Technol.*270 (2015) 2026.

[173] X.G. Liu, D.Y. Geng, H. Meng, W.B.Cui, F.Yang, D.J.Kang, Z.D.Zhang, *Solid State Commun*. 149 (2009) 64–67.

[174] Z.D. Zhang, Z.C.Shi, R.H.Fan, M.Gao, J.Y.Guo, X.G.Qi, K.N.Sun, *Mater.Chem. Phys*.130 (2011)615–618.

[175] A.Tsukazaki, A.Ohtomo, T.Onuma, M.Ohtani, T.Makino, M.Sumiya, K.Ohtani, S.F.Chichibu, S.Fuke and Y.Segawa, *Nat.Mater*.4(2004)46.

[176] S.Jebril, H.Kuhlmann, S.Muller, C.Ronning, L.Kienle,V.Duppel, K.Mishra and R.eduling , *Cryst.Growth.* (2010), 2846.

[177] Y.K.Mishra, S.Kaps, A.Schuchardt, I.Paulowicz, X.Jin, D.Gedamu, S.Freitag, M.Claus, S.Wille, A.Kovalev, S.N.Gorb, R.Adelung, *Part. Syst.Charact.* 30 (2013)783.

[178] X.D.Wang, J.H. Song, Z.L. Wang, *J. Mater. Chem*. 17(2007) 720.

[179] R. F. Zhuo, H. T. Feng, J. T. Chen, D. Yan, J. J. Feng, H. J. Li, B. S. Geng, S. Cheng, X. Y. Xu, and P. X. Yan, *Phys. Chem.C.* 112 (2008)11767.

[180] Y. Zou, L. Jiang, S. Wen, W. Shu, Y. Qing, Z. Tang, H. Luo, *and* D. Fan, *Appl. Phys. Lett.*, 93, (2008), 261115.

[181] K.Verma, A. Kumar and D. Varshney, *Curr. appl. phy.* 13 (2013) 473.

[182] N. Rezlescu, C. Pasnicu and M.L. Craus , *J. Phys. Cond. Matter* 6 (1994)5707.

[183] S.R. Ovshinsky, M.A. Fetcenko and J. Ross, *Science* 260 (1993)181.

[184] S.Berchmans,H. Gomathi and G. Prabhakara Rao, *J. Electroanal. Chem.* 394, (1995) 270.

[185] M.Yoshio,Y. Todorov,K.Yamato, H. Noguchi, J.I. Itoh, M. Okada and T. Mouri, *J.of Power Sources* (1998)53.

[186] A. James, Dirksen, K. Duval and T.A. Ring, *Actu.B. Chem.* 80 (2001)115.

[187] E.L. Miller and R.E. Rocheleau, *J. Electrochem. Soc.*144 (1997) 3077.

[188] R.C. Makkus, K. Hemmes and J.H.W.D. Wir, *J. Electro Chem. Soc*. 141 (1994) 3429. [189] G. Boschloo and A. Hagfeldt, *J. Phys. Chem.* B 105 (105) (2001) 3039–3044.

[190] G. Cao, Nanostructures & Nanomaterials: second ed. World Scientific Publishing Company, ISBN: 4324557 (2011), 978–981.

[191] K. Ali, A.K. Sarfraz, A. Ali, A. Mumtaz and S.K. Hasanain, *J.Magn.Magn.Mater.*, (2014), 369-385.

[192] R.K.Selvan, V.Krishnan, C.O.Augustin, H.Bertagnolli, C.S.Kim and Gedanken, *J. Chem. Mater.* 20 (2008) 439.

[193] H. Qiao, Z. Wei, H. Yang, L. Zhu and X. Yan, J. Nanomater. (2009).

[194] P.Xu, X.J.Han, C. Wang, D.H. Zhou, Z.S.Lv, A.H. Wen, X.H. Wang, B.J. Zhang, *Phys. Chem. B* 112 (2008)10449.

[195] L.G.Yan, J.B.Wang, X.H. Han, Y.Ren, Q.F.Liu, F.S.Li, *Nanotechn.* 21(2010) 095708.

[196] W.Zhu, L.Wang, R.Zhao, J.Ren, G. Lu and Y. Wang, J.*nanocrystals Nanoscale* 3 (2011) 2864.

[197] C. Wang, X. Han, X.Zhang, S.Hu, T. Zhang, J. Wang, Y.Du, X. Wang and P.Xu, *Phys. Chem. C*, 114 (2010)14830.

[198] Y.B. Feng, T. Qiu, C.Y. Shen, *J. Magn. Magn.Mater*.318 (2007)13.

[199] C.L.Yuan,Y.S. Tuo, *J.Magn. Magn. Mater*. 342 (2013) 53.

[200] X. Gerbaux, A. Hadni, M. Tazawa, and J. C. Villegier, *J. C. Appl. Opt.* 33 (1994) 59.

[201] T. J. Edwards, D. Walsh, M. B. Spurr, C. F. Rae, M. H. Dunn, and P. G. Browne, *Opt. Express* 14 (2006) 1589.

[202] S. Makhluf, R. Dror, Y. Nitzan,Y. Abramovich, R. Jelinek, and A. Gedanken, *Adv. Funct. Mater*.15 (2005), 1715.

[203] H. Yu, T. Wang, B .Wen, M. Lu, Z.Xu, C. Zhu, Y. Chen, X. Xue, C.Sun and M. Cao, *J. Mater. Chem*, 22 (2012) 21685.

[204] K. Kaviyarasu and P. A. Devarajan, *Advan. in Appl. Sci. Reseer.*,6 (2011)138.

[205] R. Wahab, S.G. Ansari, M.A. Dar,Y.S. Kim and H.S. Shin, *Mater. Sci. Forum* 986 (2007) 559.

[206] A. N. Andriotis, R. M. Sheetz, and M. Menon, *J. Phys. Condens. Matte.r* 22, (2010) 334210.

[207] G. Z. Xing,Y. H. Lu,Y. F. Tian, J. B. Yi, C. C. Lim, Y. F. Li, G. P. Li, D. D. Wang, B. Yao, J. Ding, Y. P. Feng, and T. Wu, *AIP Adv*. 1 (2011) 022152.

[208] B. M. Maoz, E. Tirosh, and M. B. Sadan, *Phys. Rev. B* 83 (2011)161201.

[209] T. L. K. Brinkman, K. Nishida, T. Katoda, and H. Funakubo, *Ferroelectrics*, 35 (2007) 357-361.

[210] N. Kumar, D. Sanyal, and A. Sundaresan, *Chem. Phys. Lett*. 477 (2009) 364.

[211] F. Gao,J. Hu, C. Yang, Y. Zhang, H. Qin, Li. Sun, X. Kong, and M. Jiang, *J. of Solid State Communic.* 149 (2009) 858.

[212] M.Z. Wu, Y.D. Zhang, S. Hui, T.D. Xiao, S.H. Ge, W.A. Hines, J.I. Budnick, G.W. Taylor,*Appl. Phys. Lett.* 80 (2002) 4406.

[213] Z. Ma, J.B. Wang, Q.F. Liu, J. Yuan. *J.Surf. Sci.* 255 (2009)6633.

[214] I.Huynen, N.Quiévy, C.Bailly, P.Bollen, C. Detrembleur,S.Eggermont, I. Molenberg, J.M. Thomassin,L. Urbanczy and T. Pardoen, *Acta. Mater.* 59 (2011) 3266.

[215] R. F. Zhuo, H. T. Feng, J. T. Chen, D. Yan, J. J. Feng, H. J. Li, B. S. Geng, S. Cheng, X. Y. Xu and P. X. Yan *J. Phys. Chem. C*, 122 (2008) 11775.

[216] K.Lakshmi,K. Honey,T. John, M. R. Joseph K.E. George, *Acta Mater*.57 (2009) 375.

[217] K.Verma, A. Kumar, D. Varshney, *Curr. Appl. Phy.* 473 (2013).

[218] J.Cao, W. Fu, H. Yang, Q. Yu, Y. Zhang, S. Liu, P. Sun, X. Zhou, Y. Leng, S.Wang, B. Liu, and G. Zou, *The J. of Phy. Chem. B*, 113 (2009) 4647.

[219] J. Yin, H. Cao, J. Zhang, M. Qu, and Z. Zhou, *Cryst. Growth , 13* (2013) 769.

[220] M.G-Fabra, P. Dunne, D.Grant, P. Gooden, E. Lester, *J. Chem. Engine.* 226 (2013) 29.

[221] S. Salmaoui, F. Sediri, N. Gharbi, *J. of Polyhedron*, 29 (2010) 1777.

[222] P. Saini,V. Choudhary, B.P. Singh, R.B. Mathur, S.K. Dhawan,. *Mater.Chem. Phys*. 113 (2009) 119.

[223] H.S.Mansur, C. M. Sadahira, A. N. Souza, and A. A. P. Mansur, *J.Mater. Sci.and Engi*. C, 28 (2008) 548.

[224] H. S. Mansur, R. L. Orefice, and A. A. P. Mansur, *J. of Polymer*, 45 (2004)7202.

[225] O.Yayapao, T.Thongtem, A.Phuruangrat and S.Thongtem, *J. of Alloys and comp.*509 (2011) 2299.

[226] N. H. Hong, J. Sakai, N. Poirot, and V. Brize, *Phys. Rev. B* 73 (2006) 132404.

[227] A. Sundaresan,R. Bhargavi,N. Rangarajan,U. Siddesh, and C. N. R. Rao, *Phys. Rev. B* 77 (2008),201306

[228] I. Shalish, H. Temkin, and V. Narayanamurti, *Phys. Rev. B 69* (2004), 245401.

[229] L.Zhang,L.Yin, C. Wang, X.N. Lun, Y. Qi, and D. Xiang, *J. Phys. Chem. C* ,114 (2010) 9658.

[230] I. S. Elfimov, S. Yunoki, and G. A. Sawatzky, *Phys. Rev. Lett.* 89 (2002) 216403.

[231] J. A. Chan, S. Lany, and A. Zunger, *Phys. Rev. Lett.* 103 (2009), 016404.

[232] W. Zhu, L. Wang, R. Zhao, J. Ren, G. Lua, Y. Wang,*Nanoscale* 3, 2862 (2011).

[233] Z. Ma, J.B. Wang, Q.F. Liu and J. Yuan, *J.Surf. Sci*. 255 (2009) 6633.

[234] I. Huynen, N. Quiévy, C. Bailly, P. Bollen, C. Detrembleur, S. Eggermont, I. Molenberg, J.M. Thomassin,L. Urbanczy and T. Pardoen, *J.Acta. Mater.* 59 (2011),3266.

[235] P.Bollen, N.Quiévy, I. Huynen, C. Bailly,C. Detrembleur, J.M. Thomassin and T. Pardoen, *Scripta Materialia*,68 (2013) 54.

[236] W. Zhu, L. Wang, R. Zhao, J. Ren, G. Lua, Y. Wang, *Nanoscale* 3, (2011)2862.

[237] X. Sun, J. He, G. Li, J. Tang, T.Wang, Y. Guo and H. Xue, *J. Mater. Chem.C*,1(2013)777.

[238] X.G.Liu, D.Y.Geng. H.Meng, P.J.Shang and Z.D, *Appl.Phy.lett.* 92 (2008)173117.

[239] L.J. Rong, Itoh, M.Terada, Masao, Horikawa, T. Machida and Kenichi, *Appl.Phys.*91 (2007), 093101.

[240] R.Kalai, Selvan, C.O.Augustin, V.Sepelak, L.John Berchmans, C. Sanjeeviraja, A. Gedanken, *Materials Chemistry and Physics* 112 (2008)380.

[241] M.M. Rashad, D.A. Rayan, A.A. Ramadan, *J Mater Sci: Mater. Electron.* 24 (2013) 2749.

[242]M. Rahim Uddin, M.R. Khan, M.W.Rahman, A. Yousuf and C. K. Cheng, Reac. *Kinet. Mech. Cat.* 116 (2015) 604.

[243] Raul Valenzuela, Volume 2012, Article ID 591839, 9 pages, Phy. Research Internat. doi:10.1155/2012/591839

[244] R.K.Selvan,V. Krishnan,C.O.Augustin, H. Bertagnolli, C.S. Kim, A. Gedanken, *Chemical Material* 20 (2008) 439.

[245] O. Stefanescu, G. Vlase, M. Barbu, P. Barvinschi, M. Stefanescu, J. Therm Anal. Calorim. 113 (2013) 1253.

[246] C. Karunakaran, S. SakthiRaadha, P. Gomathisankar and P. Vinayagamoorthy, *RSC Adv***.** 3 (2013)16738.

[247] V. Krishnan, R.K. Selvan, C.O. Augustin, A. Gedanken and H. Bertagnolli, *J. Phys.Chem. C*. 111 (2007) 16733.

[248] M.Ashter, A.Munir, M.Anis and A.Maqsood .*Mater. Resear. Bull.* 79 (2016) 14-21.

[249] T. Jan, J. Iqbal, M. Ismail, N. Badshah, Q. Mansoor, A. Arshad and Q. Ahkam, *Mater Sci. in Semicond. Process.* 21 (2014)160.

[250] J. Iqbal, M. Rajpoot.T. Jan and I. Ahmad, *J. of Supercond. and Novel Magn.* 27 (2014)1749.

[251] P. Raju, S. R. Murthy, *Adv. Mat. Lett.* 4 (2013)105.

[252] K. M. Batoo, M. S. Ansari, *Nanoscale Resea Lett.* 7 (2012)125.

[253] V. Krishnan, R.K. Selvan, C.O. Augustin, A. Gedanken, H. Bertagnolli, , *J. Phys. Chem. C* 111 (2007) 16724-16733.

[254] S.R. Ovshinsky, M.A. Fetcenko and J. Ross, *Sci.* 260 (1993)181.

[255] S.Berchmans,H. Gomathi and G. Prabhakara Rao, J. Electroanal. *Chem.* 394, (1995)270.

[256] M.Yoshio, Y. Todorov, K.Yamato, H. Noguchi, J.I. Itoh, M. Okada and T. Mouri, *J. Power Sources* (1998)53.

[257] A. James, Dirksen, K. Duval and T.A. Ring, *Actu. B. Chem.* 80 (2001)115.

[258] E.L. Miller and R.E. Rocheleau, *J. Electrochem. Soc.*144 (1997) 3077.

[259] R.C. Makkus, K. Hemmes and J.H.W.D. Wir, J. *Electro Chem. Soc.* 141 (1994) 3429.

[260] G. Boschloo and A. Hagfeldt, A. *J. Phys. Chem. B* 105 (2001), 3039-3044.

[261] G. Cao, Nanostruc. and Nanomater: second ed., (2011), World Scientific Publishing Company, ISBN: 978–9814324557.

[262] R.K.Selvan, V.Krishnan, C.O.Augustin, H.Bertagnolli, C.S.Kim and Gedanken, *J.Chem.Mater.* 20 (2008) 439.

[263] H. Qiao, Z. Wei, H. Yang, L. Zhu and X. Yan, *J. Nanomater.* (2009).

[264] E. Pervaiz and I.H. Gul, Int. J. Curr. Eng. Technol. 2 (4), (2012) 387.

[265] Georgia.C. and Papaefthymiou, "*Nanoparticle Magnetism*",Nanotoday,4 (2009) 447.

[266] T. Liu, Y. Pang , X. Xie , W. Qi , Y. Wu , S. Kobayashi , J. Zheng and X. Li, "*J. Alloy. Compd."* 667 (2016) 296.

References